Photoelectrochemical Performance of Catalyst Systems Based on Pd deposited TiO_2 and Ag incorporated $BiFeO_3$

Pelin Yilmaz

Submitted in partial fulfilment of the

requirements of the Degree of

Doctor of Philosophy

School of Engineering and Materials Science,

Queen Mary University of London

London, United Kingdom

Declaration

I, Pelin Yilmaz, confirm that the research included within this thesis is my own work or that where it has been carried out in the collaboration with, or supported by others, that this is duly acknowledged below and my contribution indicated. Previously published material is also acknowledged below.

I attest that I have exercised reasonable care to ensure that the work is original, and does not to the best of my knowledge break any UK law, infringe any third party's copyright or other Intellectual Property Right, or contain any confidential material.

I accept that the College has the right to use plagiarism detection software to check the electronic version of the thesis.

I confirm that this thesis has not been previously submitted for the award of a degree by this or any other university.

The copyright of this thesis rests with the author and no quotation from it or information derived from it may be published without the prior written consent of the author.

Pelin Yilmaz

March 8th, 2016

Acknowledgements

I would like to thank my supervisor Prof. Dr. Steve Dunn for his endless support and guidance throughout my PhD. I felt very lucky and honoured to be a part of his group as I really admired his work and science ethics. He was always there to give ideas and always was very encouraging when I struggled with my PhD. I would also like to express my appreciation to Dr. Joe Briscoe for his brilliant recommendations in the lab and his caring support. I also want to express my gratitude to Dr Armando Lacerda as he helped me so much with Pd synthesis, TEM imaging and gas chromatography. My special thanks go to my science sister Ann Louise Anderson for her constant support through our PhD journeys together and her kindness to do the proof reading of my thesis.

I am grateful to my amazing colleagues and friends Dr. Yongfei Cui, Dr Nimra Jalali, Shuqun Chen, Dr. Luz Romero, Xuan Li, Yaqiong Wang, Ying Tu and all other residents of Office 3.72. They have been a huge part of my studies and it was a pleasure to work with them in the lab and in the office. I also want to thank Mr Darwin Yeo from Nanyang Polytechnic in Singapore for our collaboration which I really enjoyed. I further would like to thank Dr. Krystelle Mafina, Dr. Zofia Luklinska, Dr. Nadezda Tarakina Dr. Rory Wilson and Mr. John Booth, who helped me with materials characterisation equipment and the potentiostat.

My final and greatest thanks are for my family, my sister Selin in particular, my close friends and my two cats who always kept me motivated and cheered me up during this journey.

Dedication

This thesis submitted on March 8th International Working Women's Day (2016) is dedicated to the brilliant women in science who have struggled but never gave up. Their passion and determination has been inspiring and encouraging for me as a scientist and will always be appreciated.

Abstract

Since the discovery of titanium dioxide's (TiO_2) capability for water-splitting and photocatalytic degradation of organic compounds, semiconductor photocatalysis has received great attention and promises an environmentally clean and sustainable solution by solar hydrogen production and waste water treatment.[1,2] In this thesis, the photocatalytic performance of two different photocatalyst systems based on Pd nanoparticle decorated n-type TiO_2 nanorods and Ag incorporated p-type $BiFeO_3$ thin films were investigated for solar hydrogen and oxygen production and photodecolourisation of a common textile dye, Rhodamine B.

High surface area TiO_2 nanorods were grown on glass fibre substrates by a hydrothermal method to produce a mechanically robust photocatalytic filter. Metallic Pd nanoparticles were deposited onto TiO_2 nanorods via a photochemical method. It was found that the hybrid Pd/TiO_2 catalyst system showed higher photoactivity with a doubled kinetic rate for the photodecolourisation of RhB. Full decolourisation has been achieved in 180 minutes with as-grown TiO_2 nanorods whereas this time was reduced to only 90 minutes for the Pd/TiO_2 hybrid catalyst. This enhancement was associated with the localised surface plasmon resonance (LSPR) effect due to the interaction of Pd with visible light and the electron scavenging role of Pd for efficient charge separation.

The same hybrid Pd/TiO_2 photocatalyst system was then developed on FTO coated glass substrates so that the photoelectrochemical experiments can be carried out using a potentiostat. Mott-Schottky curves demonstrated a positive

shift in flat band potential and an increased charge carrier density after Pd deposition. The facilitated charge transfer at the interface of Pd and TiO_2 was shown by EIS data with a smaller arc size for Pd/TiO_2 in Nyquist plots. The photoelectrochemical performance of the bare TiO_2 and hybrid Pd/TiO_2 samples were compared through the photoelectrocatalysis of Rhodamine B (RhB) and solar hydrogen production in different electrolyte solutions at various applied voltage values. A higher amount of hydrogen by Pd/TiO_2 was photogenerated in methanol solution whereas bare TiO_2 produced a higher amount of hydrogen in 0.01M Na_2SO_4 and pure deionised water under the same conditions. The results were discussed by proposing possible reaction mechanisms with an emphasis on the charge trapping role of Pd nanoparticles.

P-type $BiFeO_3$ (BFO) thin films were deposited on large scale FTO coated glass substrates by a sol-gel method. A photocurrent density of -0.004mA/cm^2 was achieved at 0V vs NHE under AM1.5 G illumination and 1.2μmol of O_2 was produced in 2h at an external bias of -0.5V vs Ag/AgCl. These values were significantly increased upon the incorporation of Ag into the BFO matrix. Ag was incorporated into the $BiFeO_3$ matrix at different concentrations as metallic Ag structures and Ag nanowires. The enhancement by Ag modification was attributed to enhanced light absorption due to light scattering effect and efficient charge separation by Ag as they act as electron sinks. These explanations were supported by shifts in flat band and onset potentials after Ag modification in detailed measurements of Mott-Schottky plots and j-v curves.

Table of Contents

List of Figures

List of Tables

CHAPTER 1: INTRODUCTION

Energy harvesting from sunlight offers a clean and sustainable solution to the global energy crisis due to the inevitable development of civilisation and depletion of natural resources such as oil and coal.[3] Solar energy is a free endless natural source with minimum environmental effect. Research into solar energy utilisation relies on efficient solar light conversion to various types of more useful energy, such as chemical or electrical energy, as well as effective energy storage and distribution.[4]

One of the most exciting technologies in this field is heterogeneous photocatalysis.[5] This process consists of a semiconductor catalyst, a solution and light irradiation. The semiconductor photocatalyst generates an electron and hole pair when it absorbs a photon of light. These photoexcited charge carriers separately undergo redox reactions with the adsorbed molecules at the semiconductor/liquid interface.[6] Redox reactions for water splitting involve the oxidation of water to evolve O_2 gas and H^+ ions with subsequent reduction of these H^+ ions to produce H_2 gas. It is the formation of hydroxyl ions by redox reactions that can then chemically attack organic compounds for other photocatalytic processes such as dye decolourisation. It was the work of Fujishima and Honda in 1972 on TiO_2 photoanodes for solar-driven water-splitting and degradation of stearic acid that pioneered the research in this field.[2] Heteregeneous photocatalysis now has a great potential for solar hydrogen production and waste water treatment.[1]

The phenomenon is more complicated than it sounds. A successful photocatalytic process requires a suitable band gap within the semiconductor, with a suitably positioned conduction band and valence band with the corresponding thermodynamic and kinetic energy to overcome the overpotentials to do the redox chemistry.[7] There

has been extensive research on almost every available semiconductor material over the years to satisfy these requirements.[8] Semiconductors with various band gap energies and band levels have also been modified by introducing new energy levels by doping, metal deposition or coupling by another semiconductor.[9]

Photoelectrochemistry examines each of these mechanism steps through the fundamentals of physics, chemistry, optics and electronics.[10] It analyses the semiconductor photocatalyst system with a variety of photoelectrochemical characterisation tests to come up with a deeper understanding for the mechanism so that necessary modifications can be performed to maximise the solar light conversion efficiency. The modifications of photocatalysts focus on improvements to enhance wavelength range response, to efficiently separate charge carriers and to enhance redox reactions by an efficient charge transfer between the photocatalyst and the adsorbed molecules.[11]

Since Fujishima and Honda's work, the most heavily investigated is still TiO_2 due to its chemical stability, low cost and good photocatalytic efficiency.[12] The two main drawbacks of TiO_2 as a photocatalyst is the lack of visible light harvesting associated with its large band gap energy (~3.2eV) and the short lifetime of its photoexcited charge carriers.[13] The investigations with TiO_2 therefore mainly concentrate on the modifications to enhance its optical response to visible light and induce an efficient charge separation to surpass the recombination of electrons and holes.[14]

There is also a growing interest in ferroelectric materials in photocatalytic and photovoltaic applications due to their materials properties associated with carrier separation and chemical stability under illumination in aqueous environments.[15,16] Among ferroelectric photocatalysts, $BiFeO_3$ stands out as a visible light driven

photoactive material due to its narrow band gap (2.0-2.2eV).[17] $BiFeO_3$ is an interesting material with its varying band positions, indirect/direct band gap characteristics and p and n type conductivity. Its structural, optical and electrical properties have been also studied extensively to understand its complex structure.[18]

This thesis reports an investigation into the photocatalytic performance of two different photocatalyst systems based on Pd nanoparticle deposited n-type TiO_2 nanorods and Ag incorporated p-type $BiFeO_3$ thin films.

The main objectives of this project were:

- To synthesise n-type TiO_2 nanorods and p-type $BiFeO_3$ thin films on glass fibre and FTO coated glass substrates and separately investigate their potential use for photodecolourisation of a common textile dye Rhodamine B or photogeneration of hydrogen and oxygen under simulated solar light.
- To investigate the influence of metal loading (Pd and Ag) on photocatalysts in terms of photoactivity, flat band potential and charge transfer kinetics at the metal/semiconductor interface by a variety of photoelectrochemical tests.
- To develop an understanding of charge transfer and redox reaction mechanisms occurring at photoelectrocatalysis of dye and water in different solutions under various values of voltages externally applied.

The thesis consists of 7 chapters and the corresponding summaries of each chapter are:

Chapter 1 gives brief background information on the solar energy conversion and semiconductor photoelectrochemistry followed by the aims and objectives of the project.

Chapter 2 summarises the literature review starting with the fundamentals of photoelectrochemistry with a brief background on semiconductor physics followed by mechanisms of dye degradation and water splitting. The chapter then introduces two photocatalysts that were studied in this project, TiO_2 and $BiFeO_3$, with their structural, electrical and optical properties. Modification techniques for the enhancement of photocatalytic activity are listed discussing the mechanism behind each technique with example studies on TiO_2 and $BiFeO_3$ in literature.

Chapter 3 presents the details of synthesis of the materials and methods to carry out the photoelectrochemical tests. The characterisation methods are also described.

Chapter 4 focuses on the development of a robust photocatalytic filter which is composed of TiO_2 nanorods supported on glass fibres substrates. The photocatalytic performance of the catalyst system is tested through photodecolourisation of RhB. The effect of annealing and Pd nanoparticle loading onto TiO_2 is also investigated with recyclability tests of the system.

Chapter 5 focuses on the photoelectrochemical performance of the Pd/TiO_2 system grown on FTO coated glass. The conductive substrate enables the discussion of photoelectrochemical characterisation of the system providing a deeper understanding of the mechanism with j-v curves, Mott Schottky plot and electrochemical impedance spectroscopy. The performance of the Pd/TiO_2 catalyst system compared to bare TiO_2 system is investigated through photoelectrocatalysis of Rhodamine B and solar hydrogen production in different solutions at a variety of externally applied voltages.

Chapter 6 investigates the potential use of p-type BiFeO3 thin films on large area FTO coated glass for photo-oxidation of water. The effect of Ag modification in

photocurrent and the amount of photogenerated oxygen amount is investigated by various photoelectrochemical tests.

Chapter 7 summarises the conclusions of all chapters and suggests future work and research on the project

CHAPTER 2: LITERATURE REVIEW

2.1. Photoelectrochemistry of Semiconductors

2.1.1. Overview and History

Photoelectrochemistry is a field that blends fundamentals of optics, physics, electronics and chemistry. It is a complex scientific area that compromises electrochemical systems involving semiconductor materials exposed to light. The photons absorbed by the semiconductor create excited electron and hole pairs which separately interact with redox reactions at the semiconductor/electrolyte interface.[7]

The earliest photoelectrochemical study was by Becquerel in 1839, whereby he placed a silver chloride electrode in an acidic solution which was connected to platinum electrodes, which enabled the demonstration of the photovoltaic effect when the system was illuminated.[19] This photovoltaic effect was termed as the Becquerel effect. In 1954, Brattain and Garrett worked on both n and p type germanium electrodes in different electrolyte solutions and demonstrated the effect of light intensity on anodic and cathodic reactions.[20] But it was the work of Fujishima and Honda's (1972) on TiO_2 photoanodes for solar-driven water-splitting that pioneered the research on photoelectrochemistry.[2] Aside from the most popular TiO_2, almost every suitable semiconductor has been analysed for solar hydrogen production and photocatalytic treatment of water and organic compounds.

The fundamental steps can be summarised as follows (Figure 2.1):

1. **Charge generation by photon absorption:** A photon of light is absorbed by the semiconductor on the condition that the photon has higher energy than the semiconductor band gap. The absorbed photon excites the charge carriers. With

sufficient energy, electrons are excited to the Conduction Band (CB) of the semiconductor which leaves holes in the Valence Band (VB).

2. **Charge separation and transfer:** The electron and hole pairs should be separated to different surfaces of the semiconductor for redox reactions to occur. This must be done within the charge carrier lifetime which is signified as the time before they recombine.
3. **Redox chemistry at the interface:** The electrons and holes separately undergo redox reactions at the semiconductor/liquid interfaces. For water splitting, water is oxidised by holes to give O_2 gas and H^+ ions with subsequent reduction of these H^+ ions to produce H_2 gas. For other photocatalytic processes such as waste water treatment or dye decolourisation, it is the formation of hydroxyl ions by redox reactions to chemically attack the organic compounds resulting in degradation.

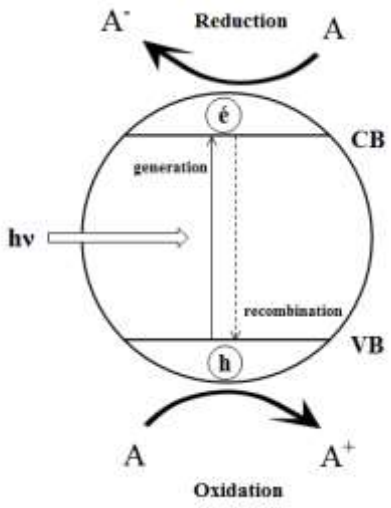

Figure 2.1 Schematic representation of the photoelectrochemistry of semiconductors: charge generation, charge separation and redox chemistry at the surface. (A: adsorbed molecules)

Photoelectrochemistry studies each of these fundamental process steps. The light harvesting efficiency, characteristics of the semiconductor and electrolyte interface, the kinetics and thermodynamics of charge separation and charge transfer together with redox chemistry all influence the resulting photoelectrochemical properties and performance.

2.1.2. Electronic Band Structure of Semiconductors

In solid-state physics, the electrical conductivity is discussed in terms of energy band structures. Instead of forming discrete energy states, molecular orbitals occupied by electrons are condensed at given energy levels.[21] These continuum energy levels form energy bands. The highest occupied energy band is termed the valence band (VB) and the lowest occupied energy band is called the conduction band (CB). The band gap (E_g) can then be defined as the energy difference between the bottom of CB and the top of VB (Figure 2.2).[22]

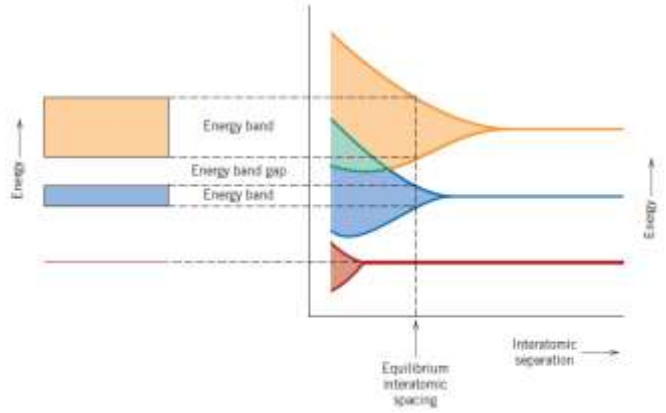

Figure 2.2 Schematic representation of the electronic band structure of materials[24]

It is the band gap energy that determines the electrical characteristics of the materials. Conductivity of a solid is determined by the occupancy of conduction band. This occurs by the promotion of an electron from the valence band to the conduction band which leaves positively charged holes in the valence band.[23] If the band gap is so

large that electrons cannot reach the CB, then the material is considered an insulator. If the band gap is small (2<Eg<4 eV), the materials is termed as semiconductor whereby the electrons need sufficient heat or photon induced energy to be excited into the CB.[24] In conductive materials, conduction band and valence bands already overlap as shown in Figure 2.3:

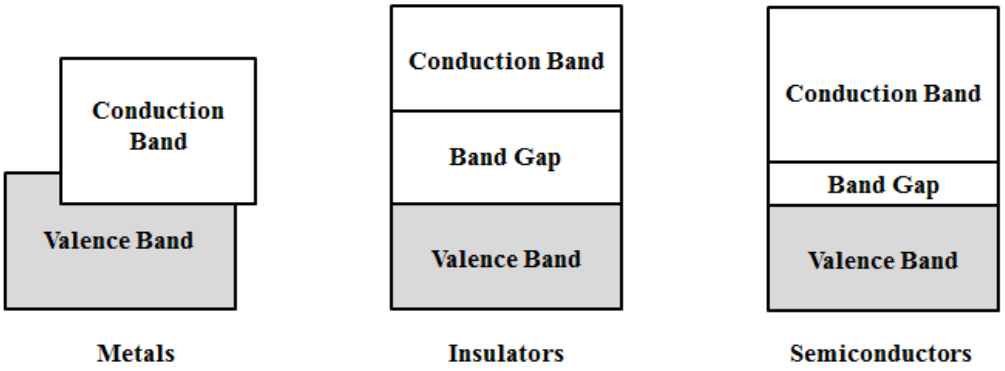

Figure 2.3 Schematic representation of the electronic band structure of metals, insulators and semiconductor materials

There have been studies on semiconductors with various band gap values (Figure 2.4).

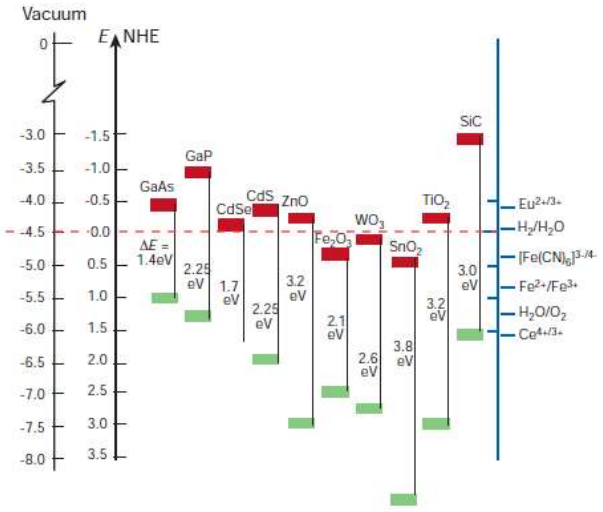

Figure 2.4 Band structures and energies for various semiconductors[8]

The Fermi level is an important concept in semiconductors. It is based on the Fermi-Durac distribution which describes the distribution of electrons into available electronic levels within a material. The probability of occupying an electron state is described by this distribution. The Fermi level is the energy level at which the probability of electron occupation is 50%.[25] This energy also corresponds to the electrochemical potential (μ) of the semiconductor.[26] The Fermi level lies in the middle of the band gap for an intrinsic semiconductor where the density of electrons is equal to density of holes (Figure 2.5).

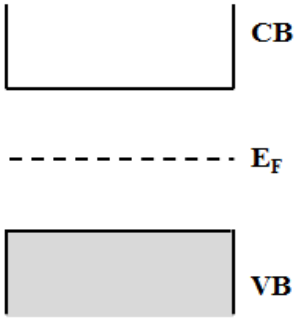

Figure 2.5 Fermi level of an intrinsic semiconductor

The density of electrons (n_i) and holes (p_i) are given by the following equations:[27]

$$n_i = N_C \exp\left(-\frac{E_c - E_{f,n}}{kT}\right) \qquad \text{Eqn (2.1)}$$

$$p_i = N_V \exp\left(-\frac{E_V - E_{f,p}}{kT}\right) \qquad \text{Eqn (2.2)}$$

where k is Boltzmann constant, T is absolute temperature, N_c and N_v are the density of energy states at conduction and valence band, E_c and E_v are the energy conduction and valence band, $E_{f,n}$ and $E_{f,p}$ corresponds to Fermi level of electrons and holes.

Since $n_i = p_i$; the equation yields:

$$n_i\, p_i = \; n_i^2 = N_C N_V \exp\left(-\frac{E_C - E_V}{kT}\right) = \; N_C N_V \exp\left(-\frac{E_g}{kT}\right) \quad \text{Eqn (2.3)}$$

The Fermi level can be shifted by altering the density of electrons or holes. This is the case for extrinsic semiconductors. For an n type material where electrons are the majority carriers, the Fermi level lies just below the conduction band. The Fermi level is just above the valence band for p-type materials where holes are the majority carriers (Figure 2.6).[28]

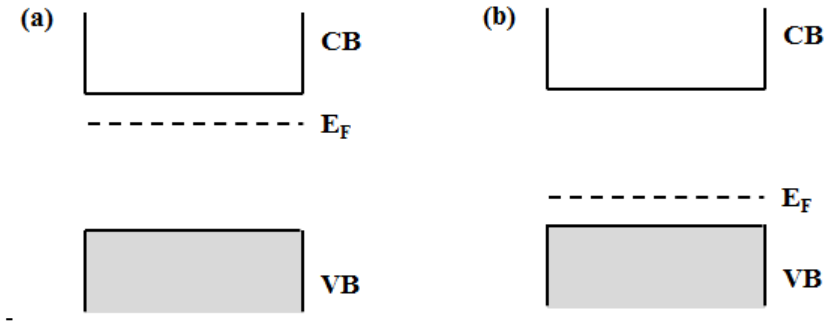

Figure 2.6 Fermi level of an (a) n-type and (b) p-type semiconductor

2.1.3. Semiconductor/Electrolyte Interface

When a semiconductor and an electrolyte are in contact, they can form rectifying junctions similar to the semiconductor/metal or semiconductor/semiconductor (pn) junctions.[7] The equilibrium is achieved on the condition that the electrochemical potentials of semiconductor and electrolyte are the same. The electrochemical potential of the semiconductor is the Fermi level, E_F, whereas it is the redox potential, $E_{F,redox}$, for the electrolyte solution. If E_F and $E_{F,redox}$ are not in the same energy level initially, there is a flow of charges between the two phases and band bending occurs until the potentials align at the same energy level, that is, $E_F = E_{F,redox}$.[29] The transfer of charges forms three charged layers at the semiconductor/electrolyte interface: the Gouy layer (G), the Helmholtz layer (H) and the Space charge layer (SCR). The

Gouy and Helmholtz layer are present in the electrolyte whereas Space Charge Layer is formed within the semiconductor. This accumulation of charges creates a potential difference and a corresponding electric field within the layers (Figure 2.7).[30]

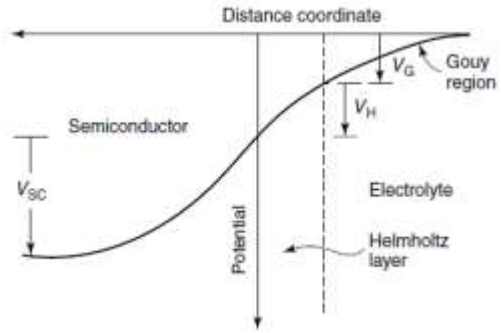

Figure 2.7 The three double layers formed at semiconductor/electrolyte interface: Space Charge layer, Helmholtz layer and Gouy layer[30]

The thickness of the Gouy and the Helmholtz layers are short; 1-10nm for Gouy and 0.4-0.6nm for Helmholtz layers. Hence, their contribution to charge transfer kinetics is often neglected. The total kinetics is therefore defined by the characteristics of the space charge region (SCR).[31] The charge distribution at the SCR depends on the conductivity type of the semiconductor. If it is an n-type semiconductor, the bands are bent upward when it is in contact with the electrolyte. The electrons migrate to the electrolyte leaving positively charged donor sites within the semiconductor (Figure 2.8).[32]

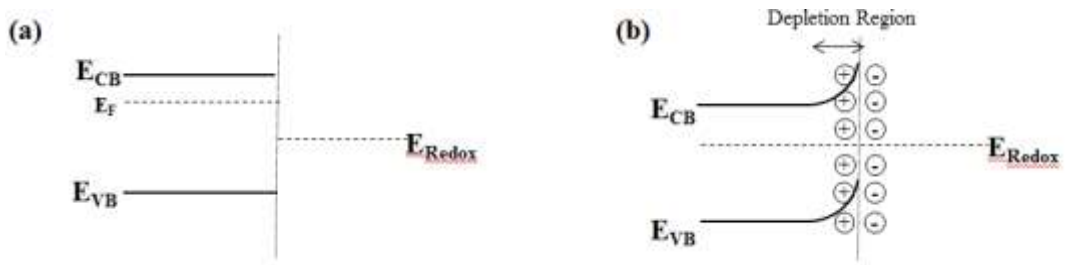

Figure 2.8 Schematic representation of energy band levels of n-type semiconductor and electrolyte (a) before and (b) after contact

However, a p-type semiconductor is opposite to this, whereby the bands are bent downward. The transfer of electrons from the electrolyte creates negatively charged acceptor sites within the semiconductor (Figure 2.9).

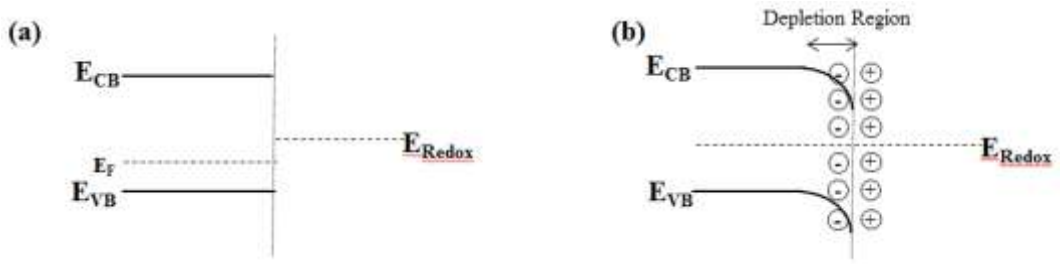

Figure 2.9 Schematic representation of energy band levels of p-type semiconductor and electrolyte (a) before and (b) after contact

2.1.4. Photocurrent Under External Bias

The Fermi level energies, direction and degree of band bending vary when there is external bias applied to the system. The voltage is applied by an electronic instrument called potentiostat (Figure 2.10). The potentiostat controls a three-electrode cell system which consists of three electrodes; namely, the working, reference and counter electrode. An external bias is applied between the reference and working electrode and the current between the working and counter electrode is subsequently measured. The electrodes are connected to each other with metal wiring and the system is in an electrolyte solution. The working electrode is the semiconductor material. Commonly used reference electrodes are Ag/AgCl and Standard Calomel Electrode. Platinum wires or mesh and glassy carbon rod are commonly used counter electrodes.

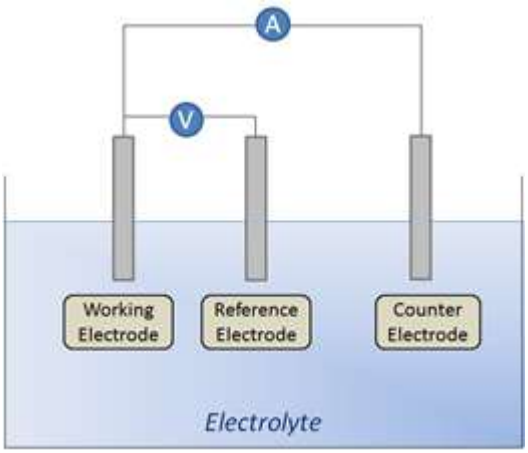

Figure 2.10 Schematic showing of a potentiostat with three electrodes

N-type semiconductors show photoanodic behaviour in a photoelectrochemical cell. The electrons are dragged from the conduction band of the n-type semiconductor to the counter electrode. Conversely, electrons are injected to the p-type semiconductor's conduction band from the counter electrode and a photocathodic performance is shown (Figure 2.11).

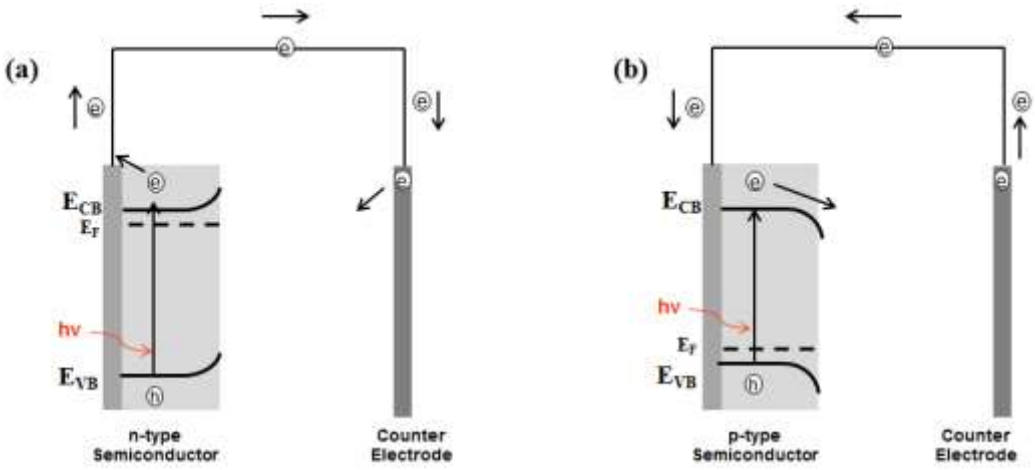

Figure 2.11 Schematic showing of electron flows between the electrodes when working electrode is an (a) n-type or (b) p-type semiconductor

The semiconductor/electrolyte junction characteristics change once the system is exposed to solar irradiation. The absorbed photon excites the charge carriers and

electrons move to the conduction band leaving behind holes in the valence band. Overflow of photogenerated electron and hole pairs split the Fermi level into two: a quasi-Fermi level for electrons (F_n) and another quasi-Fermi level for holes (F_h) (Figure 2.12).[33]

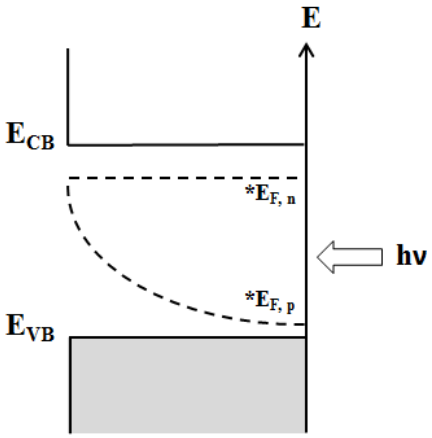

Figure 2.12 Fermi level splitting for holes and electrons under illumination

For an n-type semiconductor, the photoexcited electrons at the CB are driven to the - bulk of the electrode and then to the external circuit via the conductive substrate. Holes move to the semiconductor/electrolyte by the same potential gradient formed at the space charge region. The potential can be altered by externally applied linear sweep voltammetry. When cathodic voltages are applied, the band bending decreases and subsequently diminishes the potential gradient at the SCR leading to a decrease in the photocurrent. At the flat band potential (V_{fb}), where there is no band bending, there is no photocurrent. This potential value can therefore be coined as the onset potential (V_{ONSET}) as photocurrent is formed at potentials more anodic than this value.[34] Band diagrams of an n-type semiconductor and a corresponding hypothetical j-v curve under different voltages is shown in Figure 2.13:[35]

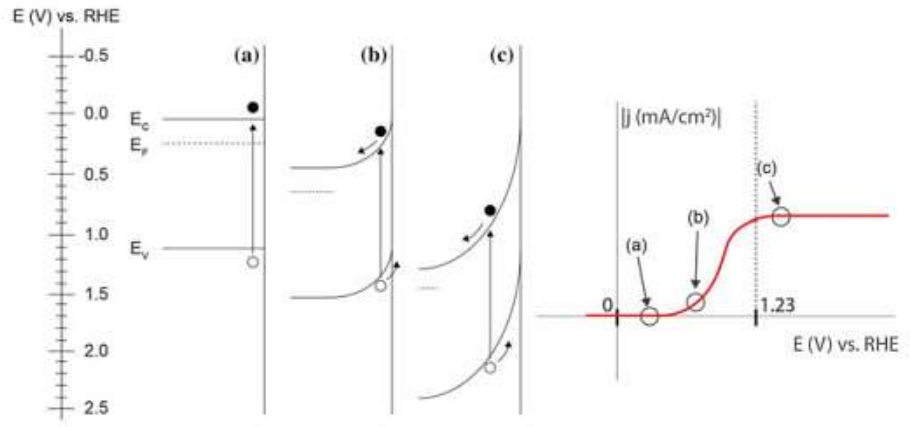

Figure 2.13 Band diagrams and corresponding j-v curve for an n-type semiconductor (a) at flat band potential, (b) sufficient potential to form photocurrent and (c) potential that saturates photocurrent[35]

The photocurrent depends on the charge transfer at the semiconductor/electrolyte and also the semiconductor/conductive substrates interfaces.

2.1.5. Electrochemical Impedance Spectroscopy (EIS)

Electrochemical Impedance Spectroscopy (EIS) is a useful technique that analyses charge transfer kinetics at the semiconductor/electrolyte. The concept of impedance was first introduced by Olivier Heaviside in 1800s. Thanks to the improvements in instrumentation and development of better understanding of the concept, electrochemical impedance spectroscopy is now a well-established electrochemical analysis method used for many applications such as semiconductors, fuel cells, batteries and biological sensors.[36]

The electrochemical kinetics in semiconductor applications is determined by the capacitance and potential formed at the semiconductor/electrolyte interface. The total capacitance formed is the combination of each layer's capacitance:[31]

$$\frac{1}{C_{total}} = \frac{1}{C_G} + \frac{1}{C_H} + \frac{1}{C_{SC}} \qquad \text{Eqn (2.4)}$$

where C_G, C_H and C_{SC}, are the capacitance of Gouy layer, Helmholtz layer, Space Charge layer respectively.

However, the thicknesses of the Gouy and the Helmholtz layers are small and so their contribution to total capacitance is often neglected. Therefore, the total capacitance is approximated as the capacitance of the space charge layer:[31]

$$\frac{1}{C_{SC}^2} = \left(\frac{2}{\varepsilon\varepsilon_0 e N_D S^2}\right)\left(V_B - V_{fb} - \frac{kT}{e}\right) \quad \text{Eqn (2.5)}$$

where ε is the permittivity of the semiconductor, ε_0 is the vacuum permittivity, e is the electron charge, N_D is the donor density, S is electrode's surface area, k is the Boltzmann and T is the absolute temperature. V_B is the applied potential and V_{fb} is the flat band potential.

The interface acts as both a capacitor and a resistor. The capacitance comes from the double layer capacitance formed between the electrode and the electrolyte with an insulating space layer in-between. The resistance originates from the polarised electrode due to charge transfer and corresponding electrolysis processes that occur at a specific voltage. The resistance of the electrolyte between the reference, counter and working electrodes should also be considered, and depends on the ionic concentration and temperature.[36]

Electrical resistance is classified as the resistance of a conductor against the flow of electrons. It follows the Ohm's Law and can be defined as the ratio between the voltage (V) and current (I) as in equation 2.6:[24]

$$R = \frac{V}{I} \quad \text{Eqn (2.6)}$$

Electrical resistance can also be expressed with the material's resistivity (ρ), which is a specific material property. For a conductor with an area of A and length of d, electrical resistance becomes:[24]

$$R = \rho \frac{d}{A} \qquad \text{Eqn (2.7)}$$

Capacitance is related to electrical energy storage. It is defined as[24]:

$$C = \frac{\varepsilon_0 \varepsilon A}{d} \qquad \text{Eqn (2.8)}$$

where ε_0 and ε are the electrical permittivity of a vacuum and the material. ε is a specific material property which outlines the material's ability to store electrical energy.[37] A is the area and d is the distance between the two electrodes.

Electrical impedance combines the two concepts whereby both capacitance and resistance are analysed under direct current (DC) and alternating current (AC). Impedance is commonly termed as complex electrical resistance. The real term of impedance is represented by the resistivity whereas the imaginary impedance is represented by the capacitance (Figure 2.14).[36]

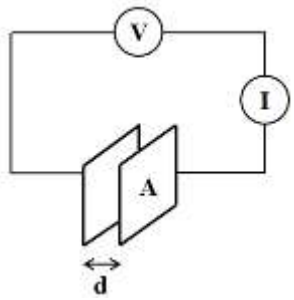

Figure 2.14 Impedance experiment: measuring resistance and capacitance at electrolyte/semiconductor interface

In semiconductor electrochemistry, electrical impedance is measured by applying an AC potential to the electrochemical cell at a specific frequency (*f*) and then measuring the resulting AC current. The AC voltage is applied with small excitation

signals that have an amplitude of V_A. The sinusoidal function of AC voltage with time V(t) becomes:[38]

$$V(t) = V_A \sin(\omega t) \qquad \text{Eqn (2.9)}$$

where ω is the radial frequency of the applied voltage, that is, ω= 2π*f*. The current response, I(t), to this voltage is also a sinusoidal function at same frequency but with a shift in the phase (ϕ):

$$I(t) = I_A \sin(\omega t + \phi) \qquad \text{Eqn (2.10)}$$

Applied voltage and current response at an impedeance experiment can be plotted as in Figure 2.15:

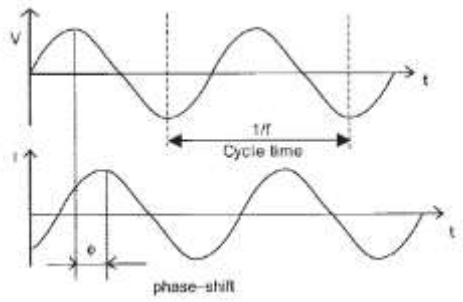

Figure 2.15 Voltage input and current output in an impedance experiment[186]

Comparable to electrical resistance following Ohm's law, the impedance is the ratio between applied sinusoidal voltage and current:

$$Z = \frac{V_t}{I_t} = \frac{V_A \sin(\omega t)}{I_A \sin(\omega t + \phi)} = Z_A \frac{\sin(\omega t)}{\sin(\omega t + \phi)} \qquad \text{Eqn (2.11)}$$

Impedance is expressed with the magnitude of $|Z_A|$ and the phase shift (ϕ). Further, to define impedance as a complex function, Euler's relationship is used:[38]

$$exp(j\phi) = cos\phi + jsin\phi \qquad \text{Eqn (2.12)}$$

$$V(t) = V_A \exp(j\omega t) \quad \text{Eqn (2.13)}$$

$$I(t) = I_A \exp(j\omega t - j\phi) \quad \text{Eqn (2.14)}$$

$$Z = \frac{V_t}{I_t} = Z_A \exp(j\phi) = Z_A (\cos\phi + j \sin\phi) = Z_{REAL} + jZ_{IM} \quad \text{Eqn (2.15)}$$

Where Z_{REAL} is the in-phase real part and Z_{IM} is the out-of-phase part of the complex function[38]. Impedance data can be presented by Nyquist plots where Z_{IM} is plotted against Z_{REAL} under different frequencies (from high to low) (Figure 2.16).

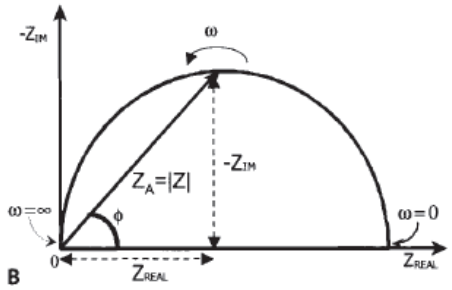

Figure 2.16 Nyquist plot of an impedance measurement plotting Z_{IM} versus Z_{REAL}[186]

The Nyquist plot can be presented as an equivalent circuit. The capacitance (C) and the resistance (R_C) of the interface are connected in parallel where the resistance of the solution (R_S) is connected in series (Figure 2.17).[39]

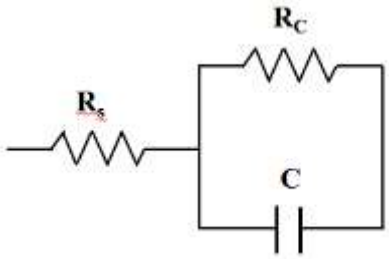

Figure 2.17 Equivalent circuiut of an impedeance mesurement

EIS is a powerful technique to understand the charge kinetics at the interface of the system. It is a crucial analysis method in photoelectrochemistry as the kinetics affact the charge transfer efficiency, hence, the electrochemical performance.

2.1.6. Flat Band Potential and Mott Schottky

Flat-band potential (E_{fb}) is an important concept in photoelectrochemistry. Photoelectrolysis of water occurs when the E_{fb} is higher than the potential of hydrogen reduction level (H^+/H_2).[40] Flat-band values for various semiconductors are shown in Figure 2.18[41]:

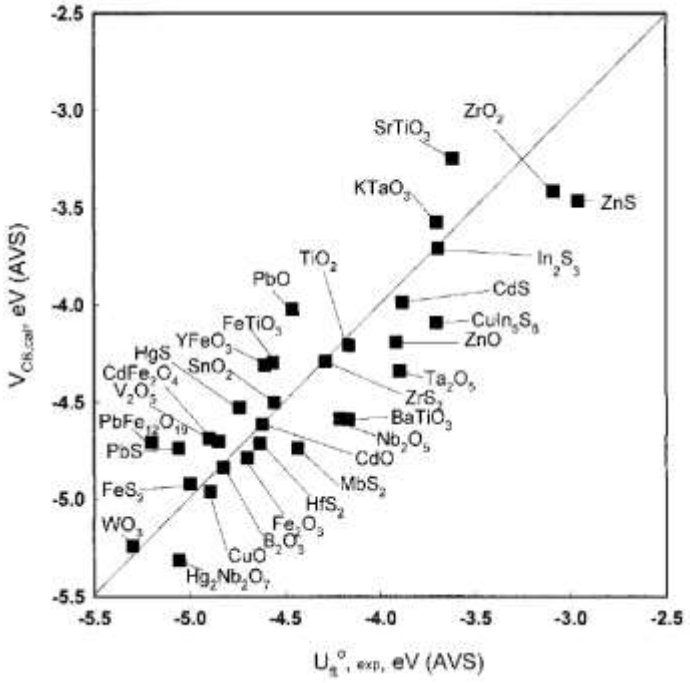

Figure 2.18 Flat band potential (U_{ft}) values for various semiconductors in absolute vacuum scale[41]

E_{fb} can be calculated from EIS measurements. Using Eqn 2.5, $1/(C_{SC})$ is plotted as function of applied potential (V_B) in Mott-Schottky curves. The slope of the curve is extrapolated to zero. The interception is the flat band potential, E_{fb}. The space charge region in p-type semiconductors is occupied by electrons; therefore, the slope of the curve is negative in an Mott-Schottky plot (Figure 2.19b).[35] It's the opposite for an n-

type semiconductor, of which Mott-Schottky curve has a positive slope (Figure 2.19a).

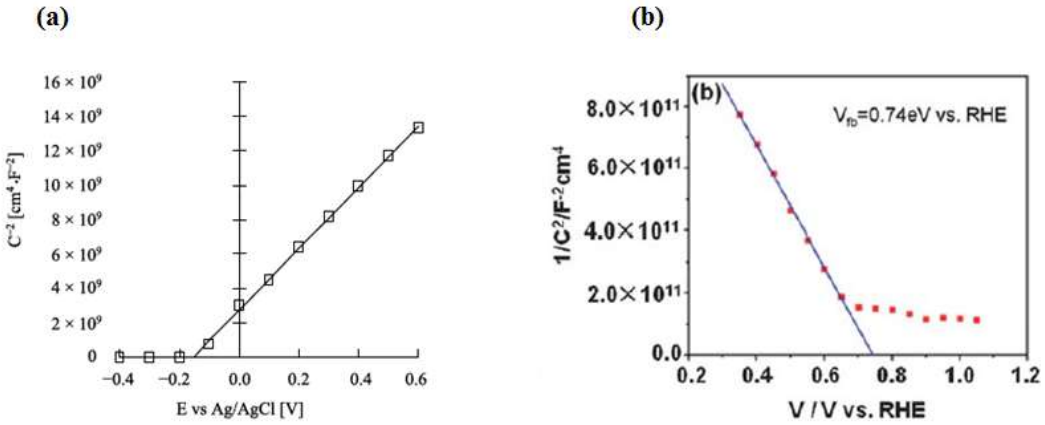

Figure 2.19 Mott Schottky plots for an n-type TiO_2 with a positive slope[187] and (b) a p-type CuO with a negative slope[188]

The Mott Schottky measurements can be done at different frequencies. The plots still extroplate to the same flat band potentials (Figure 2.20).

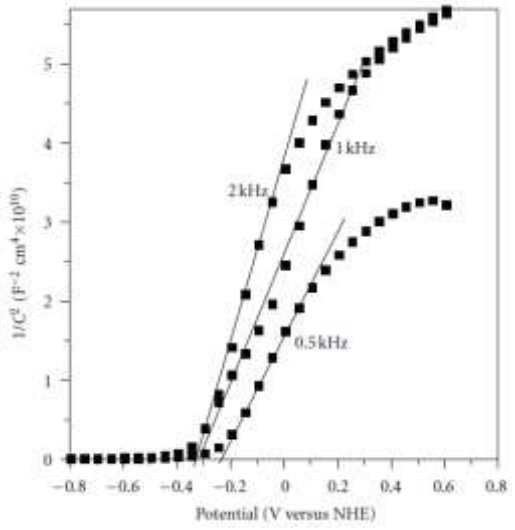

Figure 2.20 Mott Schottky plots of an n-type TiO_2 at different frequencies in 0.1M $LiClO_4$ (pH 6)[34]

The only difference is the slope which is proportional to donor carrier density. Charge carrier density can be calculated from Mott-Schottky plots using the following equation:

$$N_D = \frac{2}{e\,\varepsilon_0\varepsilon}\left(\frac{dE}{d\left(\frac{1}{C^2}\right)}\right) \qquad \text{Eqn (2.16)}$$

where e is elementary charge (1.6 x 10^{-19}C), ε_0 is the permittivity of vacuum (=8.86x10^{-12} F/m), ε is the relative permittivity of the semiconductor. [$dE/d(1/C^2)$] value is determined from the slope at the Mott-Schottky plots.

2.2. Semiconductor Photocatalysis

2.2.1. Overview and History

Photoelectrolysis of water was first studied with a system that contains of a single crystal n-type rutile structure of titanium dioxide (TiO_2) which is an inexpensive, chemically stable and non-toxic semiconductor.[2] The system is shown in Figure 2.21 where TiO_2 and platinum black were used as two electrodes which are separated by an ionically conducting separator.

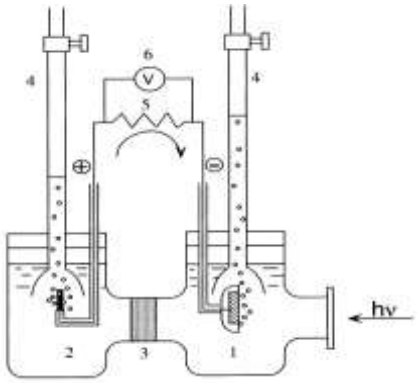

Figure 2.21 Schematic diagram of Fujishima et al.'s photocell model. (1) TiO_2 electrode (2) platinum black counter electrode (3) separator (4) gas burette (5) load resistance (6) voltmeter[42]

The band structure of TiO_2 and the potential values for both the reduction and oxidation reactions of water is shown in Figure 2.22. By exposition to UV light

followed by charge generation, the decomposition of water into hydrogen and oxygen occurs at the redox potentials.

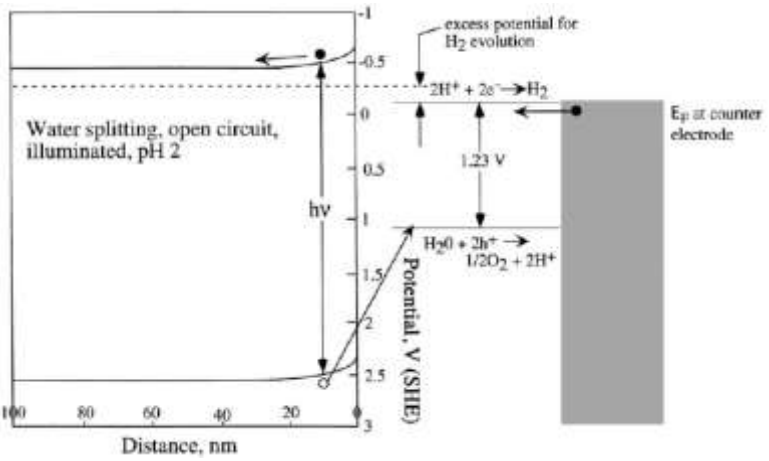

Figure 2.22 Schematic illustration of photoelectrochemical water electrolysis[42]

Fujishima et al. continued to do experiments for the decomposition of water to H_2 and O_2 by powder systems; however, it was found that the reproduction and efficiency was low. One of the suggested reasons for this was the recombination of H_2 and O_2 to generate water again before the gases are collected. Also, TiO_2 can absorb only 5% of the solar light which is too low to get a good efficiency out of the photoelectrochemical processes. Consequently, Fujishima et al. shifted their interest from photoelectrolysis of water to photo-induced degradation which is the decomposition of harmful organic molecules such as dyes, and microorganisms using light as the initiator for the process. Instead of working with big amounts of wastewater or chemical solutions, Fujishima et al. decided to first apply photocatalysis to the substances adsorbed on the catalyst surface. Stearic acid which was adsorbed on rutile TiO_2 (100) surface was completely decomposed to CO_2. This study has established a huge potential for applications of TiO_2 films such as self-cleaning walls or glasses to be used in hospitals, buildings, tunnels and many more.[2]

The mechanism for photocatalysis was found to be similar to photoelectrolysis whereby the charges generated by absorption of photons and the transfer of these charges resulted in the decomposition of the compounds. In addition, an advantage of photocatalysis over photoelectrolysis is that there was no need for counter electrodes or conductive separators to be used, as the photocatalyst semiconductor could perform compound degradation on its own.[42] The mechanism for this is shown in Figure 2.23 for the case of photodegradation by TiO_2. The electrons are excited from the valence band to the conduction band of the semiconductor and O_2 is reduced to O_2^-. Holes at the valence band are highly oxidising and oxidise the compounds to highly reactive radicals of $OH^{\cdot}$, $O^{\cdot}$ and $HO_2^{\cdot}$. These reactive radicals have been suggested to be the responsible initiators for the decomposition of the organic compounds within the system.[43]

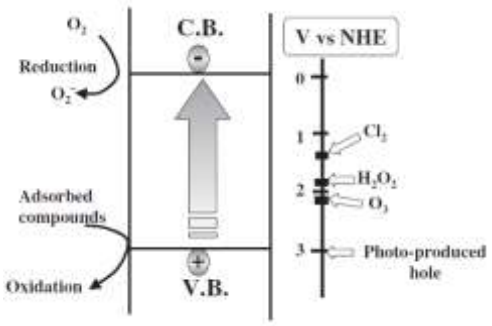

Figure 2.23 Energy band diagram for TiO_2 [42]

2.2.2. Dye Degradation

Organic dyes are one of the most commonly and greatly used chemicals within the industry. Due to large-scale production of the industry, an extensive amount of organic dyes are used for applications such as textiles, fabric, paper, cosmetics, food and agricultural research, pharmaceuticals and many more.[6] However, more than 10-

15% of the annual production of $7x10^5$ of organic dyes is wasted and joins the wastewater during manufacturing.[44]

Organic dyes present in wastewater are an environmental and health concern as their by-products have been found to cause pollution and diseases.[45] "Advanced oxidation processes" (AOPs) has been offered as an alternative to conventional treatment methods in the recent years one of which is heterogeneous photocatalysis. This process consists of a semiconductor catalyst, light irradiation and the dye solution. The in situ generation of highly reactive species such as hydroxyl and superoxide radicals, which are formed by redox reactions of electrons and holes created by photon absorptions, are the main initiators for the degradation of dye compounds.[6]

The mechanism of photocatalysis consists of three steps. The initial step is the charge generation; that is, electron-hole generation by the absorption of a photon with energy greater than the bandgap of the semiconductor. The next is the separation of electrons and holes. The separated electrons and holes drive the redox reactions with the aqueous solution whereby holes oxidise water and hydroxyl ions to form hydroxyl radicals ($OH^{\cdot}$); and electrons reduce the oxygen to form superoxide radical anions ($O_2^{\cdot -}$). It is important that recombination of electrons and holes should be avoided at this stage. The final step of photocatalysis is the attack of these radicals to the dye compounds which is called dye degradation. A schematic illustration and the redox reactions of the photocatalysis are shown below (Figure 2.24):

$$Semiconductor + hv \rightarrow e_{CB}^{-} + h_{VB}^{+} \qquad \text{Eqn (2.17)}$$

$$h_{VB}^{+} + H_2O \rightarrow OH^{\cdot} \qquad \text{Eqn (2.18)}$$

$$h_{VB}^{+} + OH^{-} \rightarrow OH^{\cdot} \qquad \text{Eqn (2.19)}$$

$$e_{CB}^{-} + O_2 \rightarrow O_2^{\cdot -} \quad \text{Eqn (2.20)}$$

$$Dye + OH^{\cdot} + O_2^{\cdot -} \rightarrow Dye\ Degradation\ Products \quad \text{Eqn (2.21)}$$

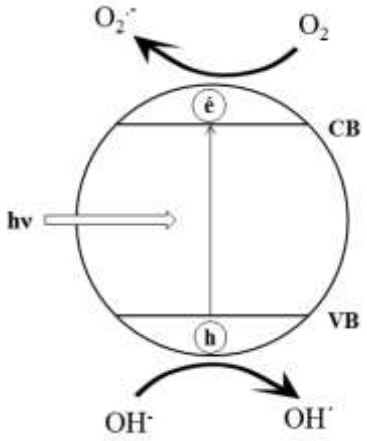

Figure 2.24 Schematic illustration of photocatalysis process

Dye degradation refers to the mineralisation of the organic molecules. This occurs either by ring opening or removal of bonds within the organic dye molecules resulting in the formation of intermediate oxidised species.[6] These species along with the oxidising radicals can be detected by characterisation techniques such as Electron Paramagnetic Resonance Spectroscopy (EPR) or Electron Spin Resonance (ESR).[46,47,48]

2.2.3. Photoelectrochemical Water Splitting

Redox reactions at PEC water splitting by electrons and holes is the combination of two half reactions which are driven simultaneously; namely, oxidation of water to run the oxygen evolution reactions (OER) at the anodic surface and hydrogen evolution reactions (HER) at the cathodic.[7] The reactions are as follows:

Charge Generation by Photon Absorption $\quad Semiconductor + 2hv \rightarrow 2e^{-} + 2h^{+}$ Eqn (2.22)

Half-reaction: Oxygen evolution reaction (OER)	$H_2O + 2h^+ \rightarrow O_2 + 2H^+$	Eqn (2.23)
Half-reaction: Hydrogen evolution reaction (HER)	$2H^+ + 2e^- \rightarrow H_2$	Eqn (2.24)
Net Water Splitting	$H_2O + 2hv \rightarrow H_2 + {}^1/_2\, O_2$	Eqn (2.25)

The overall reaction splits the water into hydrogen and oxygen gas with a 2:1 ratio. The standard reversible potential required for this reaction to occur is 1.23V. This is determined by the Gibbs Free Energy ($\Delta G^{\ominus}$ =237.18kJ/mol) required for this photo-driven water splitting whereby two pairs of electrons and holes are used for redox reactions.

Standard reversible potential $V_{rev}^{\ominus} = \Delta G^{\ominus} / nF = 1.23V$ Eqn (2.26)

The energy levels of a semiconductor's conduction and valence bands with respect to the potentials of the water decomposition are important. The energy level of the semiconductor's conduction band should be negative and near to the standard hydrogen electrode (SHE). Also, the band gap of the semiconductor should be bigger than 1.23 eV which is the equilibrium cell potential for water electrolysis at 25^{o}C and 1 atm. In brief, the band structure of the semiconductor should straddle the redox potentials so that redox reactions by both electrons and holes are thermodynamically and kinetically favourable.[7]

Since n-type semiconductors show photoanodic behaviour in a photoelectrochemical cell, the counter electrode becomes the cathode where the electrons dragged from the n-type semiconductor reduces hydrogen ions to hydrogen gas (Figure 2.25a). Conversely, p-type semiconductors become the photocathodes to evaluate H_2 whereas oxygen evolution reactions are at the counter electrode (Figure 2.25b).

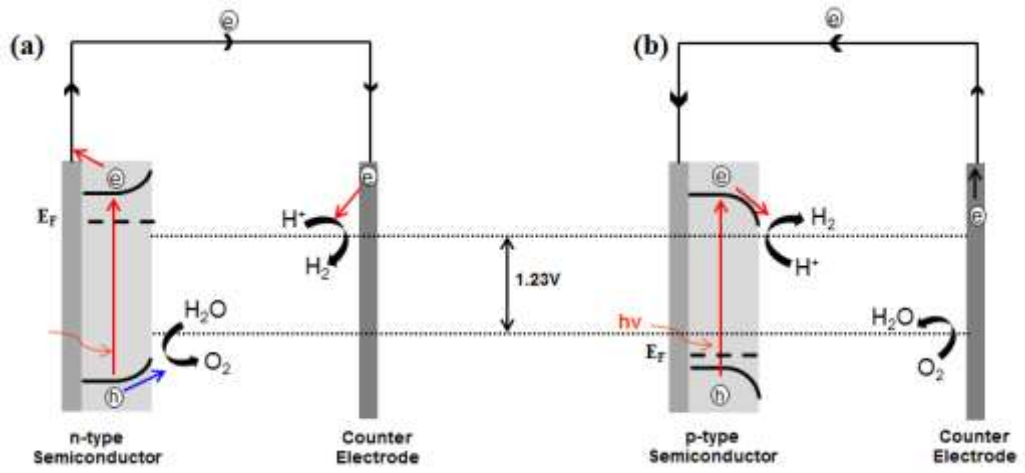

Figure 2.25 Schematic illustration of water-splitting with (a) n-type and (b) p-type semiconductor

The potential applied or obtained from the system must exceed the standard reversible potential for water splitting to occur. However, this value doesn't include overpotentials associated with potential losses at the anode and cathode, as well as losses due to the ionic conductivity of the electrolyte and wirings. These losses add up to the standard reversible potential and the operating voltage needed to overcome becomes to 1.6-1.9V for water splitting:

$$V_{op} = V^{o}_{rev} + \eta_a + \eta_c + \eta_{conductivity} \qquad \text{Eqn (2.27)}$$

where the overpotential is denoted by η.

To summarise, water-splitting is thermodynamically plausible under the conditions that the quasi Fermi level of the holes and electrons straddle the potentials that includes hydrogen reduction and water oxidations together with overpotentials (Figure 2.26).[7]

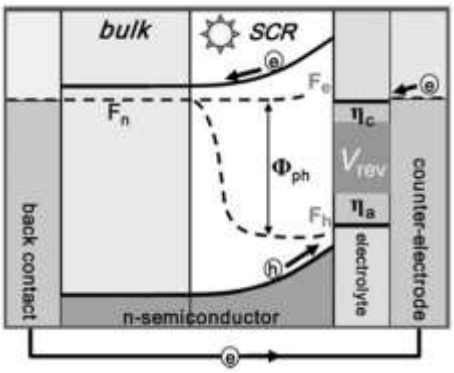

Figure 2.26 Schematic illustration of water-splitting with an n-type semiconductor including quasi fermi level and overpotentials[7]

2.2.4. Efficiency Calculations

Different definitions of efficiency exist to report a material's performance for PEC water-splitting. Still, a standardisation has not been reached which makes it difficult to compare the performances of PEC materials.[49] The primary measures of efficiency for PEC water splitting include solar-to-hydrogen conversion efficiency (STH), applied bias photon-to-current efficiency (ABPCE), incident photon-to-current efficiency (IPCE) and absorbed photon-to-current efficiency (APCE).[50]

2.2.4.1. Solar-to-hydrogen conversion efficiency (STH)

STH efficiency is the ratio of "chemical energy produced" to "solar energy input". Rate of H_2 production multiplied by the change in Gibbs free energy per mole of H_2 at 25^{o}C gives the chemical energy produced. Solar input energy is the power density obtained from the solar simulator multiplied by the illuminated photoelectrode area.

$$STH = \left[\frac{r_{H_2}(mmolH_2/s)\ x\ \Delta G_{H_2}(237\ kJ/mol)}{P_{total}\,(mW/cm^2) x\ Area\ (cm^2)}\right]_{AM\ 1.5G} \qquad \text{Eqn (2.28)}$$

Another equation to measure STH efficiency involves the power output at the system instead of chemical energy product. The power output is the product of voltage,

current and faradaic efficiency. Voltage is 1.23V (E^0) which is the water-splitting potential at 25°C. Current is the photocurrent density of the electrode.

$$STH = \left[\frac{j_{SC}(mA/cm^2)\ x\ E^0(1.23V)\ x\ \eta_F}{P_{total}\ (mW/cm^2)}\right]_{AM\ 1.5G} \quad \text{Eqn (2.29)}$$

Faradaic efficiency (η_F) is the efficiency of charges transferred to the electrode to be utilised for chemical reactions.[51] Therefore, (η_F) for water splitting becomes the amount of H_2 produced divided by (Q/2F) since 2 electrons are needed to reduce one mole of H_2:

$$\eta_F = \left[\frac{n_{H_2}\ (moles)}{Q\ (C)/\ 2F\ (96500\ C/moles)}\right]_{AM\ 1.5G} \quad \text{Eqn (2.30)}$$

where F is Faraday's constant, Q is the amount of charges in the system which is equal to photocurrent multiplied by time.

It should be noted that STH can only be valid in the condition that the gas evolution is stoichiometric gas evolution and faradaic efficiency is 100%. Externally applied bias or any sacrificial donors/acceptors should not be used when reporting STH.

2.2.4.2. Applied Bias Photon-to-current efficiency (ABPCE)

Another expression of efficiency is required under applied bias since STH cannot be reported under such conditions. ABPE can be used in this respect which is also termed as photo-conversion efficiency:

$$ABPE = \left[\frac{j_{ph}(mA/cm^2)\ x\ (1.23-|V_b|)(V)}{P_{total}\ (mW/cm^2)}\right]_{AM\ 1.5G} \quad \text{Eqn (2.31)}$$

where j_{ph} is the photocurrent density obtained at applied bias of V_b. Similar to the conditions of STH reporting, sacrificial donors/acceptors or chemical bias due to different pH conditions cannot be included.

2.2.4.3. Incident photon-to-current efficiency (IPCE)

IPCE is the ratio of photocurrent obtained to the flux of incident photons at a given wavelength. It is the ratio of electrons out to photons in. It is also termed as External Quantum Efficiency (EQE). IPCE is expressed as a function of wavelength:

$$IPCE(\lambda) = EQE(\lambda) = \frac{electrons/cm^2/s}{photons/cm^2/s} \quad \text{Eqn (2.32)}$$

$$IPCE(\lambda) = EQE(\lambda) = \left[\frac{|j_{ph}(mA/cm^2)|\ x\ 1239.8\ (V\ x\ nm)}{P_{mono}\ (mW/cm^2) x\ \lambda\ (nm)}\right]_{AM\ 1.5G} \quad \text{Eqn (2.33)}$$

2.2.4.4. Absorbed photon-to-current efficiency (APCE)

During illumination, there could be losses of photons due to reflection and transmittance. APCE excludes this fact and is based on photocurrent obtained from only absorbed photons. It is also termed as Internal Quantum Efficiency (IQE).

$$APCE(\lambda) = IQE(\lambda) = \left[\frac{|j_{ph}(mA/cm^2)|\ x\ 1239.8\ (V\ x\ nm)}{P_{mono}\left(\frac{mW}{cm^2}\right) x\ \lambda\ (nm) x\ (1-10^{-A})}\right]_{AM\ 1.5G} \quad \text{Eqn (2.25)}$$

The term $(1\text{-}10^{-A})$ comes from the Beer-Lambert law. Absorbance equals to $\log(I_0/I)$ where I_0 is the intensity of incident light and I is the intensity light that passes through.

In this research, the efficiencies of the photoelectrocatalytic experiments were expressed in Faradaic efficiency. This is due to the fact that sacrificial donors were used and external bias was applied to the systems where STH and ABPCE cannot be used for reporting. Additionally, there was no access to facilities to report IPCE and APCE.

2.3. Photocatalysts used in this Research

2.3.1 Titanium Dioxide: TiO_2

Since the discovery of TiO_2's capability for water-splitting and the photocatalytic degradation of organic compounds, there has been an extensive research on a variety of semiconductors for environmental and energy applications.[12] TiO_2 has been the most important semiconductor material that has been studied over the years due to its band gap structure, high stability and low cost.[52] In addition, TiO_2 can be synthesized in different structural forms including nanoparticles,[53] thin films[54] and nanorods/nanotubes.[55,56] A number of production methods have been studied to synthesize these different structures such as sol-gel, chemical vapour deposition, hydrothermal synthesis, pulsed laser deposition, sputtering and anodisation. The growth mechanism and correspondingly physical, chemical and optical properties differ in each of the production methods.

The crystal structure of TiO_2 consists of 3 forms: namely, anatese, rutile and brookite (Figure 2.27).[57] Rutile has a tetragonal structure with lattice constants of a = 0.4584 and c = 0.2953nm. Anatese also has a tetragonal structure with lattice constants of a = 0.3733 and c = 0.937nm. Brookite has a rhombohedral with a = 0.5436, b = 0.9166, c = 0.5135[58]. Rutile is regarded as the most thermodynamically stable phase whereas anatase and brookite are metastable.[59]

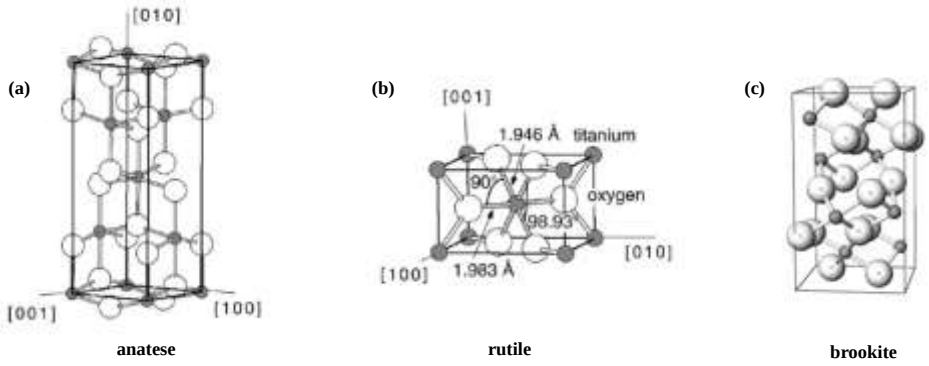

Figure 2.27 Crystal structures of TiO_2: (a) anatese, (b) rutile and (c) brookite [57]

Due to the differences between the three crystal phases, such as band structures and crystal growth orientations, the photocatalytic activities of each phase has been found to vary. In general, anatase is reported to have the highest photocatalytic performance and although a general consensus has not been held in this respect, some explanations have been suggested. Anatase has a larger band gap (~3.2eV) compared to rutile (~3.0eV) and brookite (~3.1eV).[60] Although this decreases the amount of light absorbed, the valence band is at a higher energy level, that is, closer to oxidation potentials of adsorbed molecules resulting in more effective oxidation reactions.[61] Morever, photoexcited electrons and holes have longer lifetimes within the anatase structure which is related to its indirect band structure. Recombination is more difficult in indirect band gap semiconductors as indirect transitions needed for electrons and holes to meet require more energy. Finally, it has been reported that, the charge carrier mobility of the photoexcited electrons and holes are higher in anatase compared to rutile and brookite and they manage to reach to the surface within their lifetime.[61] Therefore, with delayed recombination and more suitable band structure compared to rutile and brookite, anatase has the highest photocatalytic performance among the three TiO_2 crystal structures.[62] The photoreactivity of certain facets of TiO_2 crystal differs from each other due to their surface

chemistry.{001} facet of anatase TiO_2 and (110) plane of rutile have been reported to be most photoreactive among the other facets.[63,64] Therefore, facet engineering has been studied to grow the crystals at such certain directions and planes during the synthesis of TiO_2.[65]

Although TiO_2 is the most commonly used photocatalyst due to its superior properties such as high chemical stability, the material still exhibits low efficiency for water-splitting under solar energy. The main reason for this is that TiO_2 has a large band gap energy (~3.2eV); therefore, it can only use UV light. Since UV light is only 5% of the total solar energy, the efficiency of solar hydrogen production is limited.[14] It is important that a photocatalyst also utilises visible light which compromises 50% of solar energy.[11] One other disadvantage of TiO_2 is the short lifetime of photoexcited carriers.[13] The photogenerated electrons may recombine with holes at lower energy states. Efficient charge separation before recombination is essential. There has been extensive research on the modification of TiO_2 to resolve these problems.

2.3.2. Bismuth Ferrite: $BiFeO_3$

Ferroelectric materials hold some interesting promise in photocatalytic and photovoltaic applications due to their materials properties associated with carrier separation and chemical stability under illumination in aqueous environments.[15,16] Among ferroelectric photocatalysts such as $BaTiO_3$ (3.2eV) and $LiNbO_3$ (4.7eV) with large band gaps, $BiFeO_3$ (BFO) stands out as a visible light driven photoactive material due to its narrow band gap (2.0-2.2eV).[17] $BiFeO_3$ has been investigated extensively for its structural, optical and electrical properties to understand its complex structure induced by its varying band positions, indirect/direct band gap characteristics and type of conductivity.[66,67,68,69]

$BiFeO_3$'s phase at room temperature is R3c with a perovskite-type unit cell (Figure 2.28).[70] The valence band of $BiFeO_3$ is composed of O 2p states mixed with Fe 3d and Bi 6p states whereas Fe 3d state dominates the formation of conduction band hybridised with Bi 5p states in the region.[71]

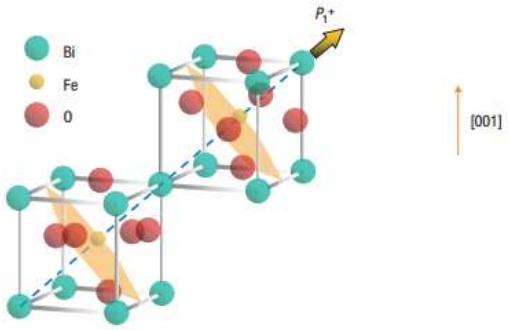

Figure 2.28 Crystal lattice structure of $BiFeO_3$ [70]

The hybridisation between the orbital states and the valence state of Fe, which depends on oxygen vacancies and stoichiometry, can introduce a momentum or a shift to the energy level of conduction and valence band. Therefore, a wide range of band gap, from 2.0eV to 2.8eV, has been reported for $BiFeO_3$ thin films where indirect/direct band gap characteristics have been both observed with small phonon participation. Density functional theory (DFT) has been the most commonly studied computational method using local spin density approximation (LSDA) to calculate the density of states of local orbitals in $BiFeO_3$ and correspondingly map the band levels.[71,72] The classical Tauc approach from experimental UV-vis spectroscopy supports computational values whereas Neaton et al. has calculated an indirect band gap of approximately 1.9eV using the LSDA+U approximation.[73] Clark has estimated a value of 2.8eV with direct band gap characteristics.[74] Ihlefeld et al. has also estimated a direct band gap of 2.77eV since the Tauc plot lacked characteristic shape when plotted for $(\alpha h\nu)^{1/2}$, therefore suggesting an indirect band gap.[67]

$BiFeO_3$'s type of conductivity depends on the intrinsic defects of the crystal structure. The bonding between the three elements and vacancies result in a variation in density of states, hence, band structures. Both p and n type conductivity have been reported for $BiFeO_3$ depending on its element deficiencies. $BiFeO_3$ grown in reducing conditions with oxygen vacancies has n-type conductivity whereas Bi and Fe vacancies result in p-type conductivity. [75,76,74] Maso and West studied conductivity of Bi deficient Ca doped $BiFeO_3$ under different processing conditions and found that the changing processing atmosphere from N_2 to air or O_2 increased the p-type conductivity.[77]

However, $BiFeO_3$ has inherent disadvantages for water splitting and photocatalysis applications. One main drawback is the high leakage current which affects the dielectric and ferroelectric properties. This is due to varying valence state of Fe (from Fe^{3+} to Fe^{2+}).[78] One other drawback is its low conductivity as a result of defects and grain boundaries. This influences photovoltaic and photocatalytic performances where efficient charge transport is essential.[79] Photoelectrocatalysis reports for $BiFeO_3$ thin films or particles mostly include half reactions of water splitting, that is, the photo-oxidation of water to evaluate oxygen gas. The studies for H_2 evolution by BFO are however limited. The limitation for hydrogen production by $BiFeO_3$ is attributed to the band positions as the conduction band of $BiFeO_3$ is below the hydrogen reduction potential. Modifications on $BiFeO_3$ such as metal deposition or coupling with another semiconductor have also been reported to enhance the photocatalytic activity.[80,81,82]

2.4. Modifications of Photocatalysts

Fundamental process of photocatalysis comprises of three steps; charge generation at the solid state, charge separation and electrochemical product by redox reactions of charges. The competence of each step plays a crucial role in photocatalytic efficiency. Therefore, modifications of photocatalysts aim to improve:[11]

- Wavelength range response to boost charge generation
- Charge separation to avoid recombination
- Charge transfer between the photocatalyst and adsorbed molecules to enhance redox reactions

Techniques for photocatalyst modifications include metal loading, ion doping, semiconductor coupling and dye sensitisation. Surface area enhancement to improve the rate of chemical reactions[83,84] and addition of sacrificial reagents[85] to prevent backward reaction of water splitting are also other methods to improve photocatalytic efficiency.

This section focuses on each of the modification techniques and explains the mechanisms behind them. Example studies on TiO_2 and $BiFeO_3$ have also been reviewed.

2.4.1. Metal Deposition

Precious metals or rare earth metals deposition on semiconductors is one of the most commonly studied methods for photocatalyic enhancement. There are two main reasons responsible for such achievement:

1. Formation of Schottky junction for efficienct charge separation (Co-catalyst)

2. Localised surface plasmon resonance (LSPR) for increased charge generation due to the absorption of visible light.

LSPR is defined as the oscillation of metal's free electrons in phase with the surrounding electrical field of an incident photon. This oscillation depends on the size of the metal particle and which light range it corresponds to. If the size can be tailored into the visible light range, then the metal photoresponses to visible light (Figure 2.29).[86] Accordingly, the photoexcited electrons are generated at the metal and then injected into the semiconductor's conduction band.

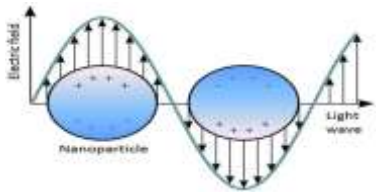

Figure 2.29 Schematic representation of localise surface plasmon resonance where the metal's free electrons oscillate due to electric field of incident light[189]

On the other hand, the photoexcited electrons created at the photocatalyst by UV light is trapped by the co-catalyst noble metal. This is related to the Fermi level position of the metals relative to the conduction band of the semiconductor. The electrons trapped by the metal can also do redox chemistry at the surface with the adsorbed molecules. A detailed schematic representation can be seen in Figure 2.30:

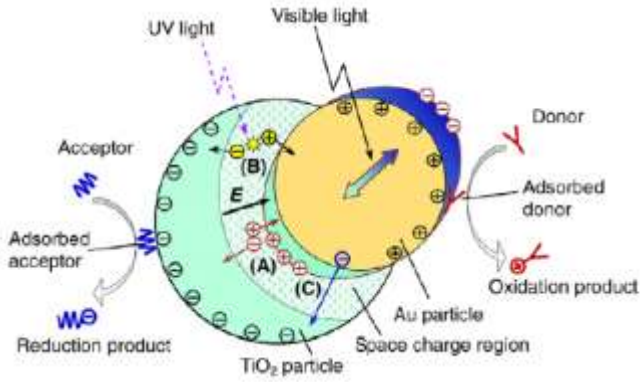

Figure 2.30 Mechanism of photocatalysis with a metal deposited photocatalyst[86]

The enhancement of photocatalytic activity by LSPR was firstly introduced by Kamat's group in 2000. He studied tailoring synthesis of metals such as Ag and Au nanoparticles on TiO_2 and the improvement of photoelectrochemical performance of TiO_2.[87,88,89] It was Awazu et al. in 2008 who defined the term "plasmonic photocatalysis" for photocatalytic enhancement by noble metals when they analysed the LSPR effect on TiO_2 by Ag nanoparticles.[90]

Ag NPs decorated $BiFeO_3$ were superior compared to bare $BiFeO_3$ due to efficient electron trapping by Ag which then reacted with dye molecules at the surface (Figure 2.31).[17,91,92] Recombination is also prevented as photoactive holes are left behind in the valence band. Photocatalytic oxygen evolution is therefore enhanced in photo-oxidation processes that have used $BiFeO_3$ particles decorated with Au NPs.[80,93]

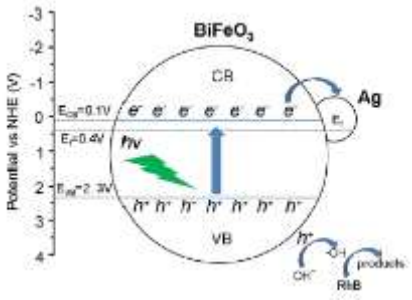

Figure 2.31 Mechanism of RhB decolourisation with Ag NPs decorated $BiFeO_3$[91]

For TiO_2, Au[94,95,96] and Ag[90,97,98,99] are the most popular noble metals to enhance the photcatalytic activity but photoactivity improvements by Pt[100,101], Pd[102,103,104] and Ru[105] have also been reported. Comparative studies on different metals have been done based on the work function of the metals.[106,107] The effect of Pd as a co-catalyst to TiO2 was studied in this research. In literature, Pd quantum dots deposited on TiO_2 nanotubes have immensely increased the photocurrent density, hence, promoted photocatalytic hydrogen production such as in Ye et al.'s study. There was a positive shift in flat band potential and the donor charge density was doubled after Pd

deposition. Ye et al. related such improvements to Pd acting as electron sinks leading to reduced recombination.[104] The extent of metal loading should be discussed because an excessive amount can have detrimental effects on the resulting photoreactivity due to the formation of recombination centres.[108] Plasmon resonance also depends on the size, loading amount and the morphology of the nanoparticles.[86]

2.4.2. Ion Doping

Another way of improving photocatalytic efficiency is metal cation or anion doping into the crystalline catalyst lattice as it expands the photo-response of the catalyst to a wider spectrum. This occurs due to the impurity energy levels that are introduced into the catalyst's bandgap.[109] Plus, charge trapping, that is scavenging electrons or holes from the semiconductor, and further transferring the charges to the surface also helps as recombination is prevented. Therefore, metal's Fermi level and semiconductor's valence and conduction band level relative to each other are important. The Fermi level of the metal should be more positive than that of semiconductor's CB so that it can trap the electrons. For scavenging holes, the Fermi level of the metal should be less positive than that of the semiconductor's VB (Figure 2.32). It is also important that the ions are doped near the catalyst surface rather than deep in the lattice with an optimum amount of ion doping[11]. This is because a higher amount of ion doping in the lattice can act as recombination centres leading to reduction in efficiency.[110]

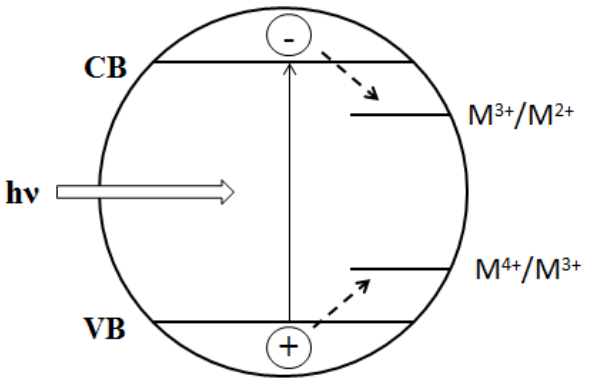

Figure 2.32 Schematic representation of band gap engineering at ion doping of semiconductors. M stands for a transition metal

Choi et al. have doped 21 metals into TiO_2 and investigated the correlation between photoreactivity and charge carrier recombination dynamics with varying concentrations. They have found that doping with metals such as Fe^{3+}, Mo^{5+}, Ru^{3+}, Os^{3+}, V^{4+} and Rh^{3+} ions has increased the photocatalytic dechlorination of CCl_4 whereas doping with Co^{3+} and Al^{3+} had negative effects on the photoreactivity.[111] Fe doping into TiO_2 has increased the hydrogen production in Dholam et al.'s study while the hydrogen production decreased with Cr doping compared to undoped TiO_2 due to formation of recombination sites.[112] The effect of doping of anions such as N, F and S into TiO_2 on photocatalysis have also been reported due to band gap narrowing leading to a shift in the photo-response to visible light, hence, improving the photocatalytic activity.[113,114,115,116]

$BiFeO_3$ has been doped by cations of Mg, Y, Al, Sr and Gd for photocatalytic purposes. Favourable band structures with narrower band gaps turned out to have the best photoreactivity.[117,118,119] In this research, Ag was chosen as the element to be doped into $BiFeO_3$; however, the Ag rather stayed on the surface or the grain boundaries instead of $BiFeO_3$'s perovskite lattice.

2.4.3. Semiconductor Coupling

Semiconductor coupling is another method that can increase the photocatalytic activity by broadening the wavelength response range whereby two different semiconductors with different band gap energies are combined together in the system[6]. The small band gap semiconductor can be excited by visible light and inject electrons into the large band gap semiconductor's conduction band. Therefore, it is essential that the conduction band of the small band gap semiconductor is more negative than that of the large band gap semiconductor. Also, the conduction band of the large band semiconductor should be more negative than the reduction potential level (H^+/H_2).[11] The electron migration between the semiconductors enables an efficient charge separation leading to enhancement in photocatalytic activity. This mechanism is shown in Figure 2.33. The coupling can be done by deposition or coating of one semiconductor onto another semiconductor.

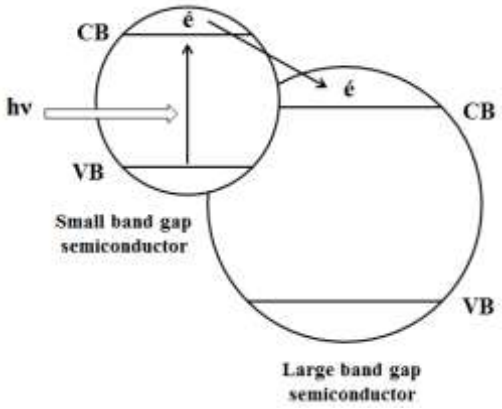

Figure 2.33 Schematic illustration of photocatalysis when the semiconductor is coupled with another semiconductor

Compensation for TiO_2's main disadvantage, which is its large band gap, has been attempted by coupling with a small band gap semiconductors such as SnO_2[120], CdS[121,122] and CdSe[123]. Heterojunctions with $BiFeO_3$ have been formed by making composites with CuO[124] and

$SrTiO_3$[125]. There have been studies on coupling TiO_2 and $BiFeO_3$ together as well to improve photocatalysis of organic dyes[81,82]. The smaller band gap of $BiFeO_3$ enables visible light harvesting whereas p-n heterojunction helps to improve charge separation (Figure 2.34).

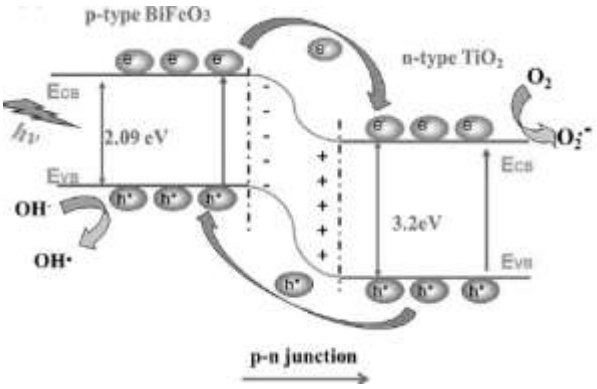

Figure 2.34 Schematic illustration of photocatalysis with $BiFeO_3/TiO_2$ heterojunctions[82]

2.4.4. Dye Sensitisation

Dye sensitisation is another method to enhance photocatalytic activity by using photoactive dyes. This is also a widely used method for solar cells. Some dyes have redox potentials and can be excited by photons as well. These photoexcited electrons are then injected from the dye into the semiconductor's conduction band (Figure 2.35).[126] If the dye's redox potential is suitable for the visible light range, this will enhance the photoresponse of the photocatalyst, hence, the photocatalytic activiy. Plus, efficienct charge separation is achieved because the electron injection is fast relative to recombination in dyes.[11] However, it is important dyes should be regenerated. Regenaration can be done by adding mediators with sacraficial agents such as I_3^-/I^- and EDTA so that he cycle of electrons can be achieved.[127,128]

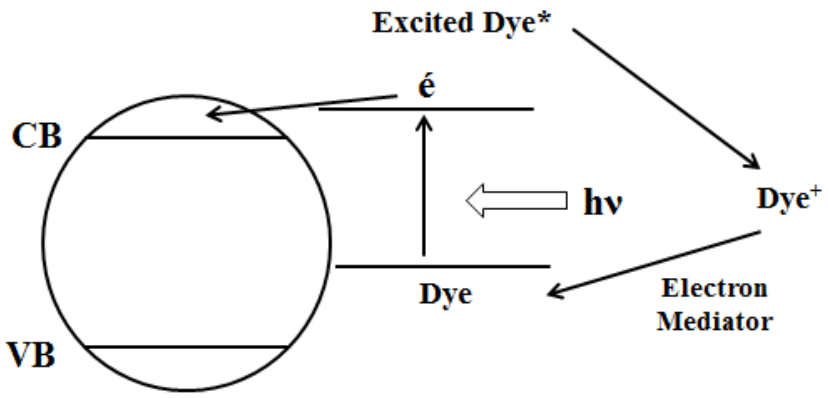

Figure 2.35 Schematic illustration of photocatalysis when the semiconductor is coupled with another semiconductor

This chapter aimed to summarise the mechanism of photoelectrochemistry together with background on semiconductor physics. Structural and optical properties of TiO_2 and $BiFeO_3$, which are the two photocatalysts that were used in this PhD project, were introduced. The limitations in photoelectrochemical performance of these photocatalysts and corresponding modifications that can be done to improve their performance were discussed in the context of fundamentals of photoelectrochemistry. Each of the modification techniques was explained by schematic illustration of their mechanism which shows how the photoactivity of the photocatalysts can be enhanced. The example reports of modifications of TiO_2 and $BiFeO_3$ in the literature were also included which gives a further insight to the project.

CHAPTER 3: EXPERIMENTAL PROCEDURE

3.1. Materials Synthesis

3.1.1. ZnO

3.1.1.1. ZnO Nanorods Growth

Prior to growing ZnO nanorods, a seed layer was deposited on the glass fibre substrates. The seed layer is formed by small ZnO crystals. The woven glass substrates were cut into 7x7 cm pieces. The substrates were washed with acetone and isopropanol for 15 minutes subsequently and rinsed with DI water. Two different methods were tried for the deposition of ZnO seed layer. First method was proposed by Liu et al.[129] A solution of zinc acetate dihydrate (Sigma Aldrich, ACS, ≥98%) (4mM) in 40 ml ethanol was stirred at 50°C for 30 mins. On the side, another solution of NaOH (Sigma Aldrich) (4mM) in 40 ml ethanol was stirred at 50°C for 1h. Upon cooling, NaOH solution was added dropwise to the zinc acetate solution. The mixed solution was kept in bath water of 70°C for 2h while the stirring was kept on. The solution obtained was colloidal. The glass fibres were placed in this colloidal solution for 15 minutes and were then dried at 150°C for another 15 minutes. This process was repeated for 3 times. The second method followed for the deposition of ZnO seed layer was proposed by Greene et al.[130] A solution of 0.03M NaOH and 0.01M zinc acetate in methanol was prepared. The solution was stirred at 60°C for 2 hours. The glass fibre substrates were in the seeding solution for 15 minutes and were then dried at 150°C for 15 minutes. This process was again repeated for 3 times. The first method failed to produce a seed layer of ZnO in this research, therefore the second method was used for further ZnO nanorods growth.

An aqueous solution method was used for the growth of ZnO nanorods.[131] A solution of 25mM of each precursors zinc nitrate hexahydrate (Alfa Aesar, 99%) and hexamethylenetetramine (Alfa Aesar, 99+%) was prepared in small jars (Figure 3.1). The glass fibre substrates with the ZnO seed layer were placed in the solution. The jars were put in the furnace at 90^{o}C for 2.5 hours. This process was repeated for 6 times with a refreshed solution.

Figure 3.1 Sealed jars used for growing ZnO nanorods with an aqeous method

3.1.1.2. Conversion of ZnO Nanorods to TiO_2 Nanorods

An aqueous solution method was used for the conversion of ZnO nanorods to TiO_2 nanorods.[132] A solution of 0.15M boric acid (Fluka, 4%) (23 ml) and 0.05M of ammonium hexafluorotitanate (AHFT) (Alfa Aesar, 99.99%) (0.9878g in 77ml of deionized water) was prepared. The glass fibres substrates, on which ZnO nanorods were grown, were placed in the solution for 3 hours at room temperature. The samples were then annealed at 450^{o}C for 2 hours (3^{o}C/min).

3.1.2 TiO_2

3.1.2.1. TiO_2 Nanorods Growth

TiO_2 nanorods were synthesised with a hydrothermal method. The nanorods were directly grown on substrates using Teflon-lined stainless steel autoclaves (Figure 3.2).

FTO coated glass substrates were cut into 2cm x 7cm pieces; glass fibres substrates were in the dimensions of 0.5cm x 7cm. The substrates were washed with acetone and isopropanol for 15 minutes subsequently and rinsed with DI water. The substrates were placed into the Teflon container with an angle where conductive FTO side was facing down. Glass fibres were replaced at the bottom of the Teflon container.

Figure 3.2 Teflon-lined stainless steel autoclave (Toption Group Co Ltd, China)

A solution of 90mL HCl (6M) (VWR International, 37%) and 2.1ml Titanium (IV) Butoxide (Sigma Aldrich, Reagent Grade 97%) was prepared and stirred vigorously under room temperature for 30 minutes. The solution was transferred to the Teflon container which was then placed in the stainless steel autoclave. The autoclave was sealed and placed in an electric oven (Memmert). The oven temperature was set to 150^{o}C and the autoclave was kept at 150^{o}C for 4 hours.[55] After cooling the autoclave to room temperature, the samples were removed from the autoclave to be rinsed with DI water and dried in air (Figure 3.3).

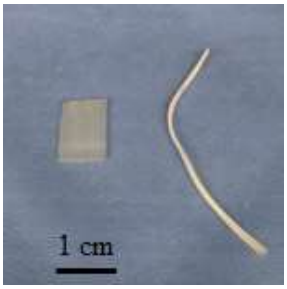

Figure 3.3 TiO_2 nanorods synthesized on FTO coated glass and glass fibre substrates

The TiO_2 nanorods grown on FTO substrates were annealed at 550°C for 3 hours with a heating rate of 3°C/min in a box furnace (Lenton). TiO_2 nanorods grown on glass fibre substrates were at 600°C for 3h (3°C/min).

3.1.2.2. Palladium (Pd) Nanoparticles Deposition onto TiO_2

Pd nanoparticles were deposited on TiO_2 nanorods via a photochemical process. In this process, Pd^{2+} ions from metal salt solution are reduced to Pd^0 nanoparticles under UV irradiation and are deposited on TiO_2 nanorods. The metal salt solution is composed of $PdCl_2$ (Sigma Aldrich, Reagent Plus 99%) dissolved in 0.01M HCl solution (VWR International, 37%) since $PdCl_2$ is not soluble in water. TiO_2 nanorods on FTO substrates (2cmx7cm) were placed into 20ml of 0.01M $PdCl_2$ in 0.1M HCl. The sample was irradiated under UV light for 30 seconds from top where TiO_2 nanorods were facing up. The sample was then turned upside down and irradiated for another 30 seconds from bottom. ~~The concentration of $PdCl_2$ (Sigma Aldrich, Reagent Plus 99%) and the length of irradiation varied for some samples to compare photoelectrochemical performance.~~ The glass fibres with TiO_2 nanorods were dived into 20ml of 0.1M of $PdCl_2$ solution. It was irradiated under UV light once for 30 seconds. The samples were then rinsed with deionised water and dried in air (Figure 3.4).

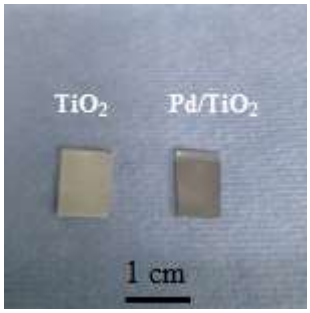

Figure 3.4 Colour change after Pd deposition on TiO_2 nanorods on both FTO coated glass

3.1.3. $BiFeO_3$

3.1.3.1. $BiFeO_3$ Thin Film Production

The BFO sol was prepared by mixing 8 grams of Bismuth Nitrate pentahydrate ($BiN_3O_9.5H_2O$, Sigma Aldrich >= 98%) and 6.06g of Iron (III) Nitrate nonahydrate ($Fe(NO_3)_3.9H_2O$, Sigma Aldrich >= 98%) in 20ml of 2-methoxyethanol ($C_3H_8O_2$, Sigma Aldrich). The solution was stirred at room temperature for 30 minutes until the powders were completely dissolved. 0.1ml of ethanolamine (C_2H_7NO, Sigma Aldrich) and 10ml of acetic anhydride ($C_4H_6O_3$, Sigma Aldrich >= 99%) were added to the solution and stirred for another 60 minutes.

The sol was deposited onto FTO substrates by spin coating at 5000rpm for 50 seconds. For pre-annealing, the thin films were placed onto a hot plate at 100°C for 5 minutes before being transferred onto another hot plate at 350°C for another 5 minutes.

Heat treatment was done in a box furnace with the following annealing intersteps:

1. Ramp up to 400°C (4°C/min)
2. Dwell for 7 minutes
3. Ramp up to 600°C (1°C/min)

4. Dwell for 3 hours
5. Ramp down 400°C (2°/min)
6. Dwell for 5 minutes
7. Ramp down to room temperature (4°C/min)

The process described above is for 1 layer of BFO thin film production on FTO coated glass. For multiple layers, the sol-gel deposition and annealing were repeated for subsequent layers (Figure 3.5).

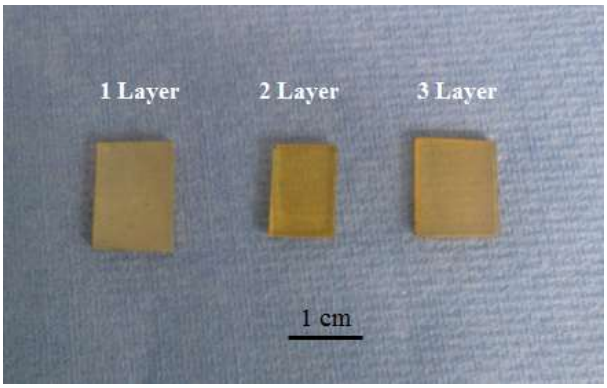

Figure 3.5 $BiFeO_3$ thin films grown on FTO substrates as 1 layer, 2 layers and 3 layers

3.1.3.2. Silver (Ag) Modification on $BiFeO_3$ Thin Films

The Silver (Ag) was incorporated in $BiFeO_3$ during the sol-gel preparation in two distinct manners:

- Precipitation of metallic Ag particles
- The addition of Ag nanowires

In case of metallic Ag particles, different concentrations of Silver Nitrate ($Ag(NO_3)_3$, Alfa Aesar 99.9%) powder was added to the solution at the initial stage of BFO sol-gel preparation. The concentration of Ag was based on molar concentration ratio between $AgNO_3$ and $BiFeO_3$ solution.

Ag nanowires (Sigma Aldrich, ϕ x L 115nm – 20-50μm in 0.5% isopropyl alcohol suspension) were added to the BFO solution at the final stage. The mixed solution was sonicated before the deposition so that the Ag nanowires were homogeneously dispersed in the sol. The concentration of Ag NWs was based on volume ratio of BFO sol and isopropyl suspension Ag NWs.

3.2. Materials Characterisation Techniques

3.2.1. Scanning Electron Microscope (SEM)

The morphology of TiO_2 nanorods and $BiFeO_3$ thin films on FTO substrates was studied using Scanning Electron Microscope (SEM, FEI Inspect F). Measurements for the thickness of thin films and the length of nanorods were also done during SEM imaging. The samples were fixed onto a steel stub with a sticky carbon tape. Any type of conductive film coating was not needed for these samples. However, to avoid charging of electrons within the SEM chamber, gold coating was done for TiO_2 nanorods on glass fibres substrates and the samples that were prepared for cross-section as they had insulating substrates. Energy-dispersive x-ray (EDX) spectrometer was also used for elementary composition analysis.

3.2.2. Transmission Electron Microscopy (TEM)

Transmission Electron Microscope (TEM, Jeol 2010) was used to investigate the microstructures of thin film, nanorods and also size and dispersion of metal nanoparticles deposited on the nanorods. For the case of TiO_2, the nanorods were scratched off from the FTO and dispersed in ethanol with ultrasonication. They were then placed into the copper grid that is fixed to the sample holder. Once the ethanol evaporated, the sample holder was inserted into the vacuum chamber. Sample preparation for $BiFeO_3$ thin film was rather difficult since it was not possible to

scratch the BFO thin film off the FTO substrate. The sample was prepared in-stu in SEM where the film was made thinner by electron beams. The edges were coated by a thin layer of Pt.

3.2.3. X-Ray Diffraction (XRD)

X-ray diffraction (XRD) patterns of the TiO_2 nanorods and $BiFeO_3$ thin films on FTO substrates were obtained with a Panalytical Xpert Pro diffractometer using Cu K_α radiation. The scan range was from 5^o to 70^o.

3.2.4. X-Ray Photoelectron Spectorscopy (XPS)

The valence states of deposited metal nanoparticles and Ag modifications at the surface of the photocatalysts were analysed by by Thermo Scientific K-Alpha X-ray photoelectron spectroscopy at NEXUS facility in University of Newcastle. The XPS was based on an Al K_α source (1486 eV). All the binding energies were calibrated according to C 1s peak at 284 eV. The software used for analysis was CasaXPS.

3.2.5. Brunauer-Emmett-Teller (BET) Surface Area Measurement

The BET surface area of TiO_2 nanorods on glass fibre substrates were analysed by Micromeritics Gemini VII. N_2 gas was used as the adsorptive gas. The BET method is based on determination of the amount of gas adsorbed on the surface of the sample at a given pressure. The samples were dried overnight at 100^oC in N_2 atmosphere. The sample was then loaded in a tube into which N_2 was introduced. There is an empty tube as a reference where N_2 was also intrdouced. By comparing the values of pressure difference, the volume of the surface area was measured.

3.2.6. UV-Vis Spectroscopy

Absorption, transmission and reflectance spectra of TiO_2 nanorods and $BiFeO_3$ thin films on FTO substrates were obtained by UV-Vis Spectometer (Perkin Elmer,

Lamda 950). The spectra range varied depending on the material. The concentration change during dye decolourisation was also measured by UV-Vis Spectometer. Dye solution samples taken at certain intervals during decolourisation process were put in 1.5ml of cuvettes for the UV-Vis scan. Following the Beer-Lambert law, absorption of the light by the dye will correspond to the dye concentration.

3.3 Photoelectrochemical Measurements

All photoelectrochemical measurements including Mott-Schottky and electrochemical impedance (EIS) were performed in a three-electrode electrochemical system with a potentiostat (Gamry Potetiostat Interface 1000), using a Ag/AgCl reference electrode and Platinium wire as the counter electrode. 0.01M Na_2SO_4 (pH= 7) was used as electrolyte.

A special cell was fabricated for photoelectrochemical measurements. The cell is composed of three parts (Figure 3.6):

Part 1: Metal plate to which the sample is attached

Part 2: Teflon chamber for the electrolyte

Part 3: Teflon side cover with a rubber sealing

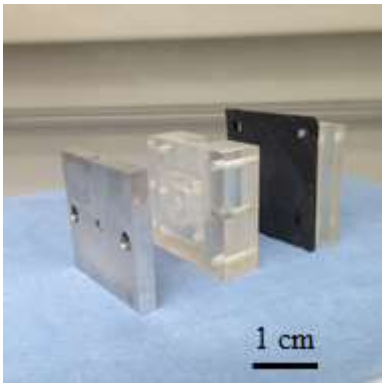

Figure 3.6 PEC cell for photoelectrochemical measurements

The samples were cut into 1cm x 1.5cm pieces. A small part of the TiO_2 nanorods from the edge (1cm x 0.2cm) was scratched off from the substrate so that FTO coated glass can be used as a contact. $BiFeO_3$ thin films could not be scratched off easily; therefore, a small part of $BiFeO_3$ was covered by a scotch tape during spin coating of the $BiFeO_3$ solution.

The samples were attached to metal plate as the working electrode (WE) from the FTO side by a silver paint. The material side of the substrate with the thin film or nanorods was facing up. The silver paint dried in air in 10 minutes. A droplet of electrolyte was dipped on the sample for wetting the material. A small rubber o-ring was placed to the hole to prevent electrolyte leakage. The metal plate along was fixed to the Teflon chamber by two small screws (3.7).

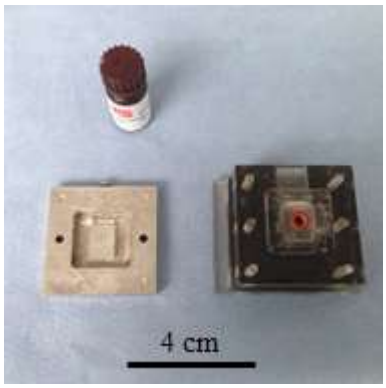

Figure 3.7 Sample preparation for photoelectrochemical measurements

The reference (RE) and counter electrode (CE) were placed into the chamber and 2 ml of electrolyte was added. The cell was fixed to a metal holder with a clamp. The electrodes were connected to the potentiostat with the alligator clips. The system was placed under the solar simulator. The light was reflected to the cell via a mirror bent at 45^o. The sample was illuminated through a hole at the metal plate. The hole has a diameter of 4mm (A= 0.125cm^2) (Figure 3.8).

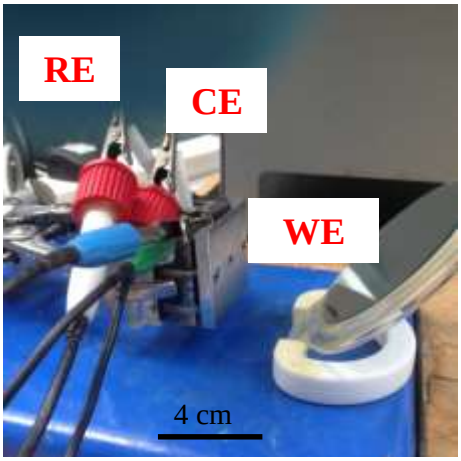

Figure 3.8 Experimental set up for photoelectrochemical measurements

3.4. Dye Decolourisation

A commonly used textile dye - Rhodamine B (RhB) was used for photocatalysis experiments. The chemical structure of RhB is shown in Figure 3.9a.[133] 5mg of Rhodamine B powder was dissolved in 500 ml deionised water to prepare 10 ppm of dye solution (Figure 3.9b).

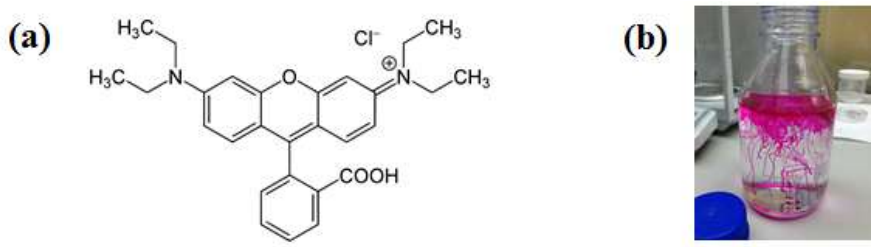

Figure 3.9 (a) Chemical structure of RhB[133] (b) Rhodamine B preparation (500ml)

For RhB decolourisation by TiO_2 nanorods grown on glass fibres substrates, following methodology was used: 8 pieces of photocatalyst (0.5cm x 7cm) samples were dispersed in 30ml of RhB dye solution (10 ppm). The system was kept under dark for 30 minutes to provide the adsorption equilibrium. The system was then illuminated from the top with a solar simulator (Figure 3.10).

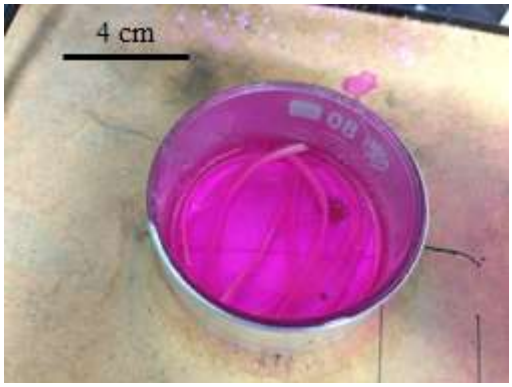

Figure 3.10 Experimental set up for dye decolourisation by TiO_2/glass fibre system after the adsorption equilibrium and just before illumination

For photoelectrocatalytic experiments by TiO_2 nanorods grown on FTO substrates, the photocatalysts were fixed in the metal plate and attached to the PEC cell just as in PEC measurements. 2ml of RhB (10ppm) dye solution was put into the PEC cell (Figure 3.11). The system was kept under dark for 30 minutes to provide the adsorption equilibrium before illumination under solar simulator. The illumination area was 0.125cm^2. Different voltages were applied to the system. Dye solution samples were not taken at certain intervals as the solution amount (2ml) is small. Only one dye solution sample per experiment was analysed by UV-Vis Spectroscopy.

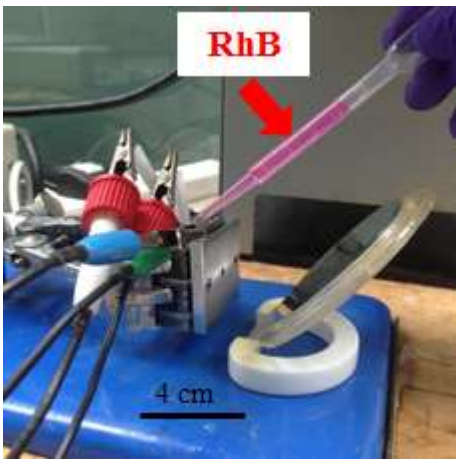

Figure 3.11 Experimental set up for photoelectrocatalysis of Rhodamine B

The calculations for concentration change using UV-Vis Spectroscopy were based on Beer-Lambert law. Beer-Lambert law indicates the relation between the absorbance (A) of a material and molar absorptivity (ε), concentration of the solution (C), and the length of the solution through which the light passes through (*l*).

$$A = \varepsilon \, l \, C \qquad \text{Eqn (3.1)}$$

where absorbance is the logarithmic ratio of the intensity of light passing through a reference cell and that of the sample cell: $\log_{10}(I_0/I)$. It can be seen from the formula that there's a linear relation between the absorbance and the concentration of the material. By plotting a calibration curve by Beer Lambert law with absorbance of different but accurately known concentrations, one can measure the concentration of an unknown solution by looking at its absorbance value at the specific wavelength.[134]

Absorbance curve for every dye solution sample taken at different time intervals was measured by UV-Vis Spectroscopy. The wavelength which gives the maximum absorbance peak for the initial dye solution sample was selected. This sample is the dye solution sample that was taken right after stirring in the dark for 30 minutes. The maximum absorption peak is at 554nm for RhB dye solution. Concentration change is determined by the following formula:

$$Concentration\ Change\ at\ i^{th}\ time\ (\%) = \left(1 - \frac{C_0 - C_i}{C_0}\right) x\ 100 \qquad \text{Eqn (3.2)}$$

where C_0 and C_i is the absorbance value of the sample taken right after stirring in the dark and at i^{th} time at 554nm, respectively.

The performance of a photocatalyst in dye decolourisation or organic compound degradation can be reported by the kinetic rates of the photocatalysis processes. The

kinetics of heteregenous photocatalysis is generally accepted to follow Langmuir-Hinselwood model.[135] The equation for rate of kinetics by this model is given as:

$$r = -\frac{dC}{dt} = \frac{kKC}{1+KC} \qquad \text{Eqn (3.3)}$$

where r is the rate of the dye decolourisation process, C is the concentration at i^{th} time, k is the reaction rate constant and K is the adsorption equilibrium constant. The equation can be simplified depending on the order of kinetics. Photocatalytic processes generally have pseuodo first order kinetics as it is accepted that $KC_i << 1$. Therefore the equation for the rate becomes:

$$r = -\frac{dC}{dt} = kKC \qquad \text{Eqn (3.4)}$$

Integrating the Eqn 3.4,

$$ln\left(\frac{C_0}{C}\right) = k_{app}t \qquad \text{Eqn (3.5)}$$

where C_0 is the initial dye concentration, C is the dye concentration at time t. k_{app}=kK is the apparent rate constant which can be determined from the slope by plotting $\ln(C_0/C)$ versus time. This value can be used to compare the efficiency of different photocatalytic systems.

3.5. Water Splitting

Water splitting processes were conducted in a sealed vessel. Two types of PEC cells were used: PEC Series 948307 and PEC Series 946621 (Adams and Schittenden Scientific Glass). PEC Series 948307 has one compartment where all of the electrodes were placed. The amount of solution put was 100ml (Figure 3.12).

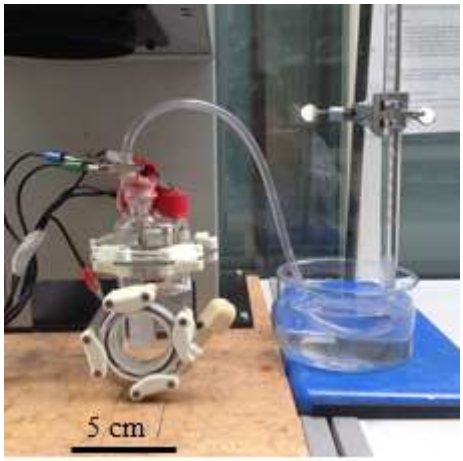

Figure 3.12 Experimental set up for water splitting with one compartment PEC Cell (Series 948307)

PEC Series 946621 has two compartments for better separation of hydrogen and oxygen after gas evolution. Working and reference electrode was put in one compartment whereas the counter electrode was put in another. Total amount of solution was 300ml (Figure 3.13). An 80 mesh platinum gauze electrode was used as counter electrode instead of glassy carbon rod for water splitting processes. The reference electrode was Ag/AgCl. The size of the photoelectrode for $BiFeO_3$ was 2cm x 3.5cm whereas it was 2 cm x 4 cm for TiO_2 samples. The photoelectrodes were illuminated through a quartz glass at the side of the PEC cells. The light was reflected from the solar simulator by a help of mirror with an angle of 45^o. The distance between the mirror and the cell was arranged in a way that the intensity of light reaching to the photolectrode was 1.0AM Sun. The cells were sealed by threads with hose barbs and septum to avoid gas leakage.

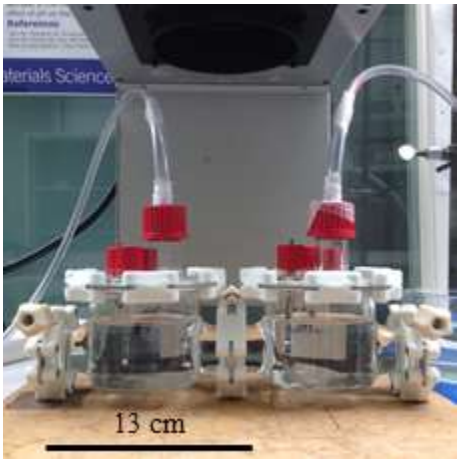

Figure 3.13 Experimental set up for water splitting with two compartments PEC Cell (Series 946621)

The system was purged with N_2 for 30 minutes before illumination to remove the dissolved oxygen from the water. Gas samples were taken manually from the vessel with a syringe for Gas Chromatography (GC) analysis.

3.6. Gas Chromatography

The gas samples were analysed by SRI 310 Gas Chromatography (Figure 3.14). Silica Gel column was fitted into the GC where Nitrogen (N_2) gas was used as carrier gas. The column was conditioned to remove any traces of gas before the analysis. The column was heated to 250^{o}C from 50^{o}C with a heating rate of 3^{o}C/min. It was kept at 250^{o}C for 3h and then cooled back to 80^{o}C. Gas samples were injected to the column manually with syringe in volume of 0.1ml. The temperature of the column was 80^{o}C for better resolution between H_2 and O_2 peaks. 100% pure H_2 gas and air was used as reference for the calibration of the gas analysis. An average value of potential (mV) with the specific retention time for was noted for the 100% H_2 peak. The retention time of the gas samples from the water splitting processes were then compared to those of the calibration samples to identify the gas type. The amount of the gas was also analysed using the potential value of reference gas where it was

considered as 100%. The percentage of the H_2 in the sample gas was then calculated by comparing its potential value (mV).

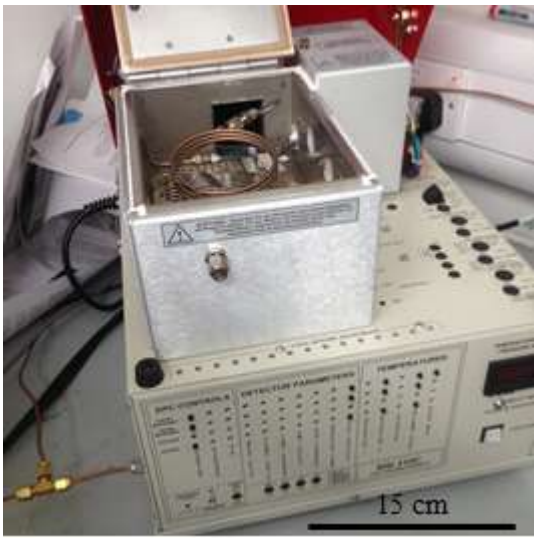

Figure 3.14 SRI 310 Gas Chromatography

CHAPTER 4: DEVELOPMENT OF HIGH SURFACE AREA TiO_2 ON GLASS FIBRE SUPPORTS FOR PHOTOCATALYSIS

Advances in Science and Technology Vol. 93 (2014) pp 196-202
© (2014) Trans Tech Publications, Switzerland
doi:10.4028/www.scientific.net/AST.93.196

Submitted: 2014-05-19
Accepted: 2014-07-10
Online: 2014-10-31

Development of high surface area titania on glass fibre supports for photocatalysis

Pelin Yilmaz[1,a], Armando Marsden Lacerda[1,b] Igor Larrosa[2,c] and Steve Dunn[1d*]

[1]School of Engineering and Materials Science, Queen Mary University of London, Mile End Road, London E1 4NS, United Kingdom

[2]School of Biological and Chemical Sciences, Queen Mary University of London, Mile End Road, London E1 4NS, United Kingdom

[a]p.yilmaz@qmul.ac.uk, [b]a.m.lacerda@qmul.ac.uk, [c]i.larrosa@qmul.ac.uk, [d]s.c.dunn@qmul.ac.uk

Keywords: Titania, glass fibre support, catalyst immobilization, palladium nanoparticles, localised surface plasmon resonance (LSPR)

Abstract

We show that we have developed a hydrothermal process that produces a high surface area TiO_2 on glass fibre supports. The as produced titania shows good photocatalytic activity against a standard commercial dye – Rhodamine B– giving full decolourisation within 3 hours under UV and visible light irradiation. The samples are mechanically robust and can act as a photocatalytic filter for waste streams and pollutants. In addition to testing the standard titania we also photochemically deposit nanostructures of Pd. These hybrid catalysts show enhanced decolourisation by an order of magnitude over the native titania systems. This enhanced performance is due to the increased energy harvesting of the hybrid system through a visible light plasmon interaction and the direct injection of electrons from the noble metal into the adsorbed dye molecules. There is a clear relationship between the absorbed light and photochemical reactivity of the system which is further explained in terms of electron hole generation and separation and plasmonic interaction. In summary, we have generated a high performance catalyst that is produced on a bulk commodity substrate with enhanced activity due to control of the surface plasmon and direct band gap transition of electron hole pairs in the semi-conductor.

Introduction

Since the discovery of TiO_2's capability for water-splitting and the photocatalytic degradation of organic compounds[1], there has been an extensive research on a variety of semiconductors for environmental and energy applications[2]. The most heavily investigated is TiO_2 due to the chemical stability, low cost and good photocatalytic efficiency.[3] In addition the range of structural forms of TiO_2 such as nanoparticles[4], thin films[5] and nanorods/nanotubes[6,7] for use as photocatalysts have further increased the interest in the material. Production methods include sol-gel[5], chemical vapour deposition[4] and anodisation.[7,8] Photocatalytic treatment of textile dye compounds such Rhodamine B, Methyl Orange-Red-Blue and organic compounds such as toluene and benzoic acid by TiO_2 have been reported over the years.[9] Among a number of experimental setups for photocatalytic treatment, most conventionally used systems are powder slurry systems where powders of the TiO_2 catalyst are mixed within the organic compound solutions that are to be photodegraded.[10] However, this application needs a post-treatment separation for the powder which can be difficult, slow and expensive.[11] Immobilisation of TiO_2 on substrates has been proposed in this respect so that catalyst/substrate can be easily removed from the solution after the photocatalytic treatment. The main drawback of the immobilisation of TiO_2 is the significant reduction in the surface area hence the decrease in the photocatalytic efficiency compared to the powder form.[12] Therefore, research on immobilisation of TiO_2 has focused on the production of

All rights reserved. No part of contents of this paper may be reproduced or transmitted in any form or by any means without the written permission of Trans Tech Publications, www.ttp.net. (ID: 156.61.160.1-30/10/15,13:31:01)

4.1. Introduction

Among a number of different experimental setups for photocatalytic treatment by TiO_2, most conventional use powder slurry systems where powders of the catalyst are mixed in the organic compound solutions that are to be photodegraded.[136] However, this application requires post-treatment separation for the powder which can be difficult, slow and expensive.[137] Immobilisation of TiO_2 on substrates has been proposed in this respect so that the catalyst/substrate can be easily removed from the solution after the photocatalytic treatment. The main drawback of the immobilisation of TiO_2 is the significant reduction in the surface area hence a subsequent decrease in the photocatalytic efficiency compared to the powder form.[138] Therefore, research on immobilisation of TiO_2 has focused on the production of systems with increased surface area of both the catalyst and the substrate.

Nanorod/nanotube structures of TiO_2 with high surface area on fibrous substrates are good candidates for such applications.[139,140] This chapter discusses the development of a catalyst system where high surface area titania nanorods were grown on glass fibre substrates. The substrates were chosen as glass fibres due to their high strength, robustness, good pH stability and low cost.[141] The samples are mechanically robust and can act as a photocatalytic filter for waste streams and pollutants. The photocatalytic performance of the catalyst systems was studied through the photodecolourisation of a standard commercial textile dye Rhodamine B (RhB).

Two different fabrication methods were tried to produce the catalyst system. Firstly, an aqueous method of conversion of ZnO nanorods to TiO_2 nanorods was used. The idea was to achieve a better uniformity and distribution of TiO_2 nanorods as it is easier to obtain uniformly distributed arrays of ZnO by an aqueous method.[142] However, the photocatalytic activity of such system was low due to limited

crystallinity and surface area. Therefore, production method was altered to a hydrothermal method where highly crystalline and high surface area TiO_2 nanorods were directly grown on glass fibre substrates in one template synthesis.

The as-grown TiO_2 showed good photocatalytic activity against RhB giving full decolourisation within 3 hours under visible light irradiation. Furthermore, Pd nanoparticles were photochemically deposited onto TiO_2 nanorods to enhance the decolourisation performance through efficient charge separation and localised surface plasmonic resonanace (LSPR) with the presence of Pd. The effect of crystallisation on photoactivity was also investigated with recyclability studies included.

4.2. Fabrication and Characterisation of the Catalysts Systems

The morphology of ZnO nanorods grown on glass fibre substrates before the conversion into TiO_2 nanorods were analysed using SEM imaging. The growth of ZnO nanorods on the glass fibres was a difficult process; it was successful only after a few attempts with different methods. A successful seeding layer is essential for the growth of ZnO nanorods. Once the ZnO seeding layer is deposited onto the surface of any substrate, the growth of ZnO nanorods are subsequently possible. The seeding layer is formed of small ZnO crystallites which are deposited on the substrate on which the nanords begin to grow. The thickness of the ZnO seed layer has been reported to range between 5nm to 10nm. It determines the direction and alignment of the nanorods along with the dimensions of the nanorods. It has been stated that the smaller ZnO crystallites lead to the growth of thinner nanorods.[143]

Two different seeding processes and surface treatments were tried before the growth of ZnO nanorods. These included washing the glass fibre mats intensively with

acetone, iso-propanol and also NaOH. The mats were also subjected to heating at 500^{o}C for 1h before the seeding process. This is because the as-received glass fibre mats stick to each other by an epoxy resin. The organic resin makes it difficult for the deposition and growth of crystallite on the glass fibres; therefore, it had to be removed.

The first seeding process followed Lui et al.'s method using zinc acetate and sodium hydroxide. Figure 4.1 shows the SEM micrographs of ZnO nanords grown on the seed crystals deposited with the above method. It can be observed that ZnO growth on glass fibre substrates was not successful. There were only some singles fibres on which partly ZnO were grown but full coverage of the outer surfaces were not achieved. This is because the seed layer was failed to be deposited on the glass fibres. This could be due to surface interactions between the ZnO crystals and the glass fibres substrates.

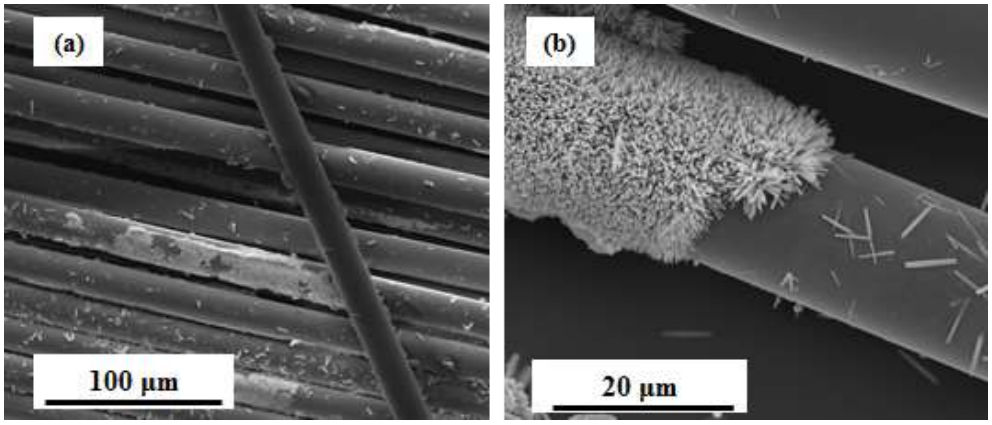

Figure 4.1 SEM micrographs of ZnO nanorods grown on glass fibres with an aqueous method. (a) Growth is not successful on most of the fibres. (b) A single glass fibre on which ZnO growth partially occurred

The processing of seeding layer was then changed to Greene et al.'s method where the precursors were again zinc acetate and NaOH but different processing temperatures and concentrations were used. Full growth of ZnO nanorods on glass

fibres was finally achieved. Figure 4.2 shows an SEM micrograph of a highly uniform and densely packed array of ZnO nanorods. The nanorods entirely cover the outer surface of the glass fibres. The length of the nanorods is around 2µm with diameters in range of 60-80nm. The diameter of the glass fibre is 17µm.

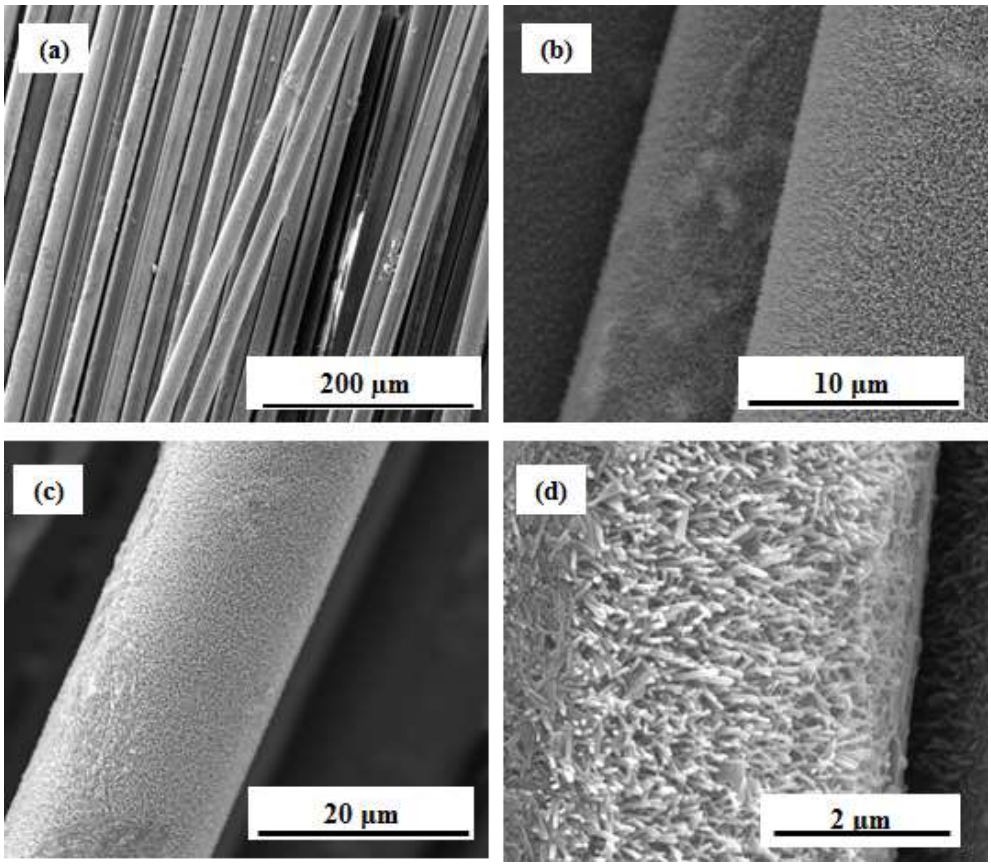

Figure 4.2 SEM micrographs of ZnO nanorods grown on glass fibres with an aqueous method

The growth of ZnO involves two steps: the nucleation of the ZnO molecules and the growth/fabrication of nucleated nanorods.[144] Solid phases of ZnO are nucleated from the dehydration of hydroxyl species such as $ZnOH^{+}$(aq), $Zn(OH)_2$(aq), $Zn(OH)_3^{-}$(aq) and $Zn(OH)_4^{2-}$(aq). Zn^{2+} ions are obtained from zinc nitrate solution ($Zn(NO_3)_2.6H_2O$). Hexamethylenetetramine (HMT) dissolves in water to give ammonia which later hydrolises to form ammonium ions (NH_4^{+}) and hydroxyls ions (OH^{-}). Zn^{2+} ions react with four molecules of ammonia (NH_3) and forms the zinc complex ($Zn(NH_3)_4^{2+}$). Finally, the zinc complex reacts with hydroxyls to form ZnO.

The reaction mechanism for the growth of ZnO nanorods can be summarized by the following chemical reactions:[145]

$$Zn(NO_3)_2 \rightarrow Zn^{2+} + 2NO_3^- \quad \text{Eqn (4.1)}$$

$$(CH_2)_6N_4 + 6H_2O \rightarrow 6HCHO + 4NH_3 \quad \text{Eqn (4.2)}$$

$$4NH_3 + H_2O \leftrightarrow NH_4^+ + OH^- \quad \text{Eqn (4.3)}$$

$$Zn^{2+} + 4NH_3 \rightarrow Zn[(NH_3)_4)]^{2+} \quad \text{Eqn (4.4)}$$

$$Zn^{2+} + OH^- \leftrightarrow Zn(OH)_2 \quad \text{Eqn (4.5)}$$

$$Zn(OH)_2 \rightarrow ZnO + H_2O \quad \text{Eqn (4.6)}$$

ZnO nanorods were then converted to TiO_2 nanorods with an aqueous solution method. Figure 4.3 shows the SEM micrographs of the samples after the conversion process and subsequent annealing (450°C, 2h, 3°C/min). The morphology didn't change as TiO_2 nanorods had the same rod structudielere. However, there was an increase in diameter as TiO_2 was firstly deposited around the ZnO nanorods. There were observable cracks in the array of nanorods at many parts of the substrate. Most of the nanorods came off the glass fibre substrates. This is due to thermal stresses formed during the heat treatment. The internal stresses formed during conversion process and heat change firstly created cracks which then led to nanorods falling off the substrate.

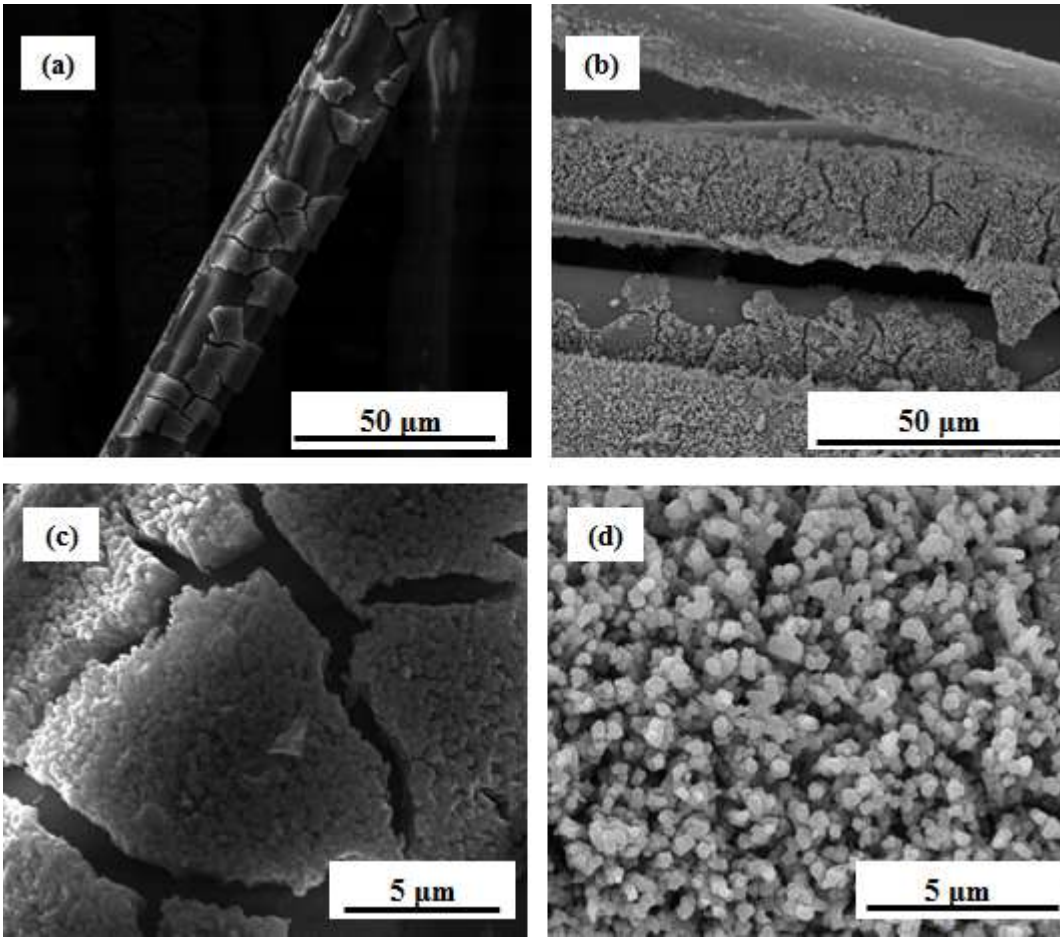

Figure 4.3 SEM micrographs of TiO_2 nanorods converted from ZnO nanorods grown on glass fibres with a two-step aqueous solution method

X-Ray diffraction (XRD) analysis was used to investigate the phase composition of the samples before and after the conversion process to see the conversion of ZnO to TiO_2 was successful. Figure 4.4 shows the XRD pattern of the ZnO nanorods on glass fibres and TiO_2 nanorods converted from the ZnO nanorods. All crystalline peaks can be indexed to wurtzite ZnO before the conversion with high peaks at (100), (002) and (101) planes. Broad peaks in between the crystalline peaks are ascribed to the amorphous glass fibre substrate. The crystalline peaks after the conversion process are indexed to a mix phases of anatase and rutile TiO_2. There was no trace of ZnO nanorods after the aqueous conversion process; therefore, it can be concluded that the full conversion of ZnO to TiO_2 was achieved successfully.

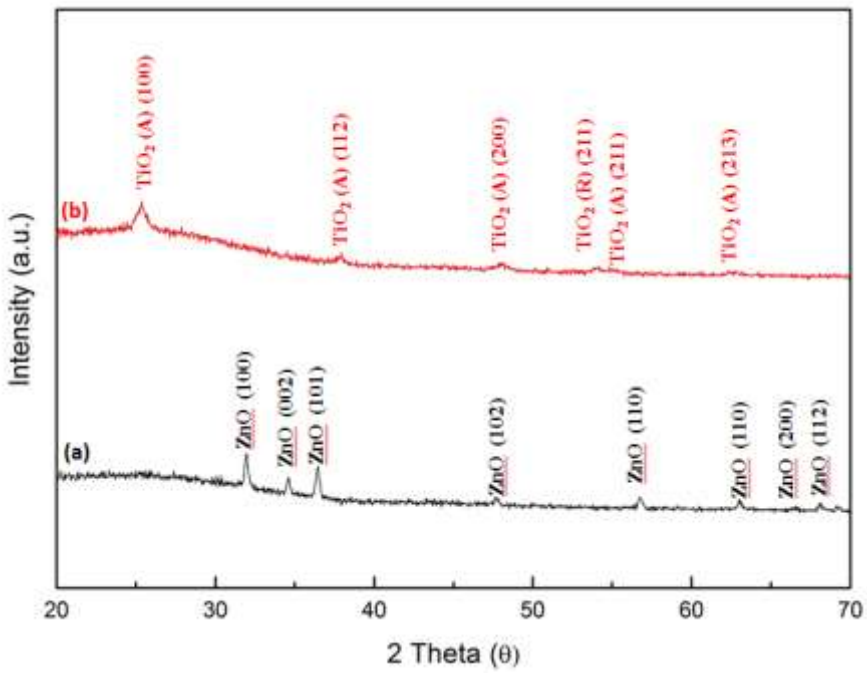

Figure 4.4 XRD pattern of (a) ZnO nanorods grown on glass fibre substrates and (b) TiO_2 nanorods after the conversion process

The chemistry behind the conversion of ZnO nanorods to TiO_2 nanorods with an aqueous method is explained in equations 4.7-4.9.[132] The conversion process from ZnO nanorods to TiO_2 nanorods is the deposition of TiO_2 on ZnO which simultaneously occurs with the dissolution of ZnO. The TiO_2 aparted from the metal-fluoro complex (AHFT) is deposited as thin layer and covers the ZnO nanorod. Then with the addition of boric acid, which is an F scavenger, the equilibrium reaction is shifted towards right. ZnO is dissolved by the H^+ ions where a ZnO/ TiO_2 core-sheath is produced. TiO_2 continues to precipitate and TiO_2 nanorods are formed. The process is illustrated in Figure 4.5 and the chemical reactions during the process are as follow:

$$MF_x^{(x-2n)-} + nH_2O \leftrightarrow MO_n + xF^- + 2nH^+ \quad \text{Eqn (4.7)}$$

$$H_3BO_3 + 4H + 4F^- \leftrightarrow BF_4^- + H_3O^+ + 2H_2O \quad \text{Eqn (4.8)}$$

$$ZnO + 2H^+ \rightarrow Zn^{2+} + H_2O \quad \text{Eqn (4.9)}$$

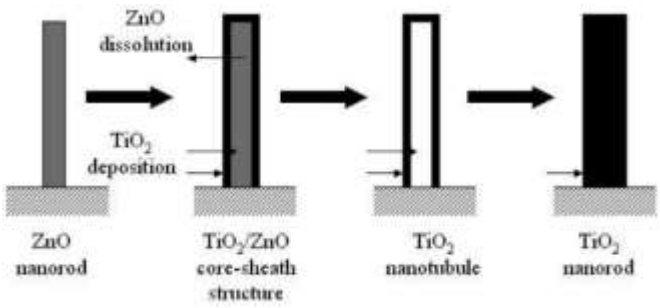

Figure 4.5 Schematic illustration of conversion process of ZnO nanorods to TiO_2 nanorods[132]

The photocatalytic activity of the TiO_2 nanorods converted from ZnO nanorods grown on glass fibres was investigated by the photodecolourisation of RhB (10ppm). A solar simulator (Newport, class ABB) fit with an AM 1.5 filter was used for illumination of the system for the photocatalysis experiments. The intensity of the light was fixed at 1 Sun (100mW/cm^2 at AM 1.5G condition) with a silicon reference cell. The spectrum of the solar simulator is shown in Figure 4.6.

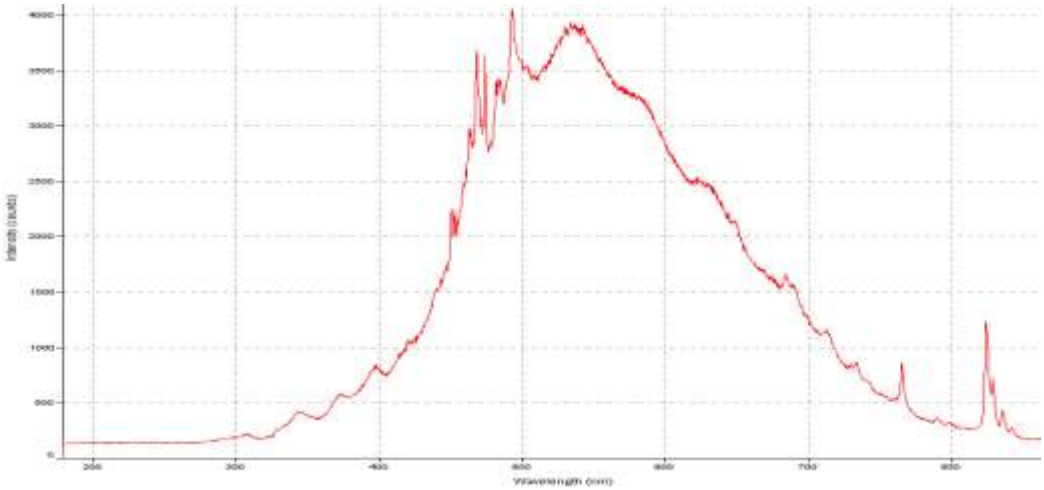

Figure 4.6 Spectrum of Solar Simulator

The sample with TiO_2 nanorods converted from ZnO nanorods grown on the woven glass fibre substrate (3cm x 4cm) was put in 30ml of RhB (10ppm) under the solar simulator. The system was kept in the dark for 30 minutes prior to illumination to

obtain the adsorption equilibrium between the dye molecules and catalyst system. The photodecolourisation profile of the RhB (10ppm) by this catalyst system is shown in Figure 4.7. The photocatalytic performance of the sample was low giving only 17% decolourisation in 3 hours. This could be attributed to the low crystallinity and low surface area as most of the catalyst nanorods peeled off from the glass fibre substrate. At this stage of the study, it was decided to change the production method for TiO_2 nanorods as conversion process was time consuming and failed to produce a catalyst system with significant photocatalytic activity.

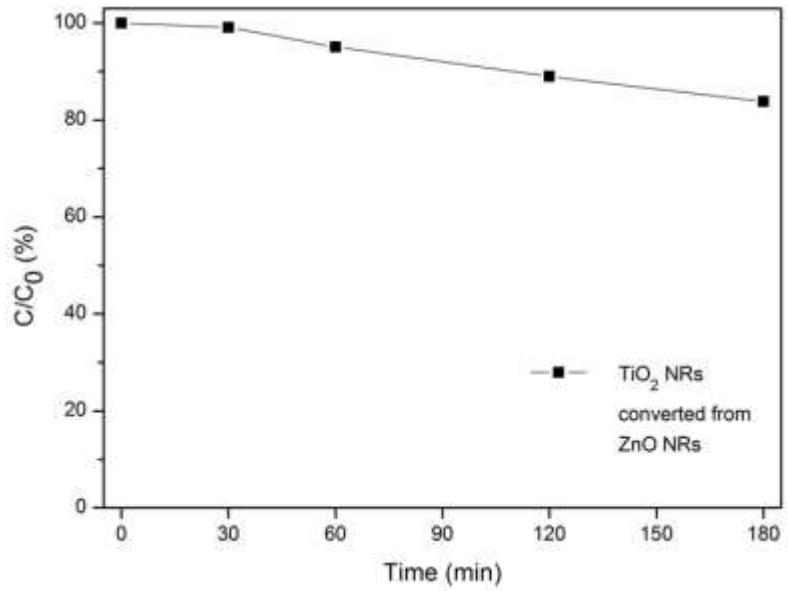

Figure 4.7 Photodecolourisation curve of RhB with TiO_2 nanorods converted from ZnO nanorods

The new fabrication technique for production of TiO_2 nanorods was hydrothermal method where TiO_2 nanorods were directly grown on the substrates. The morphology of TiO_2 nanorods hydrothermally grown on glass fibre substrates was analysed under SEM imaging (Figure 4.8). The SEM micrographs show a uniformly and densely packed array of TiO_2 nanorods covering the entire outer surface of the glass fibres. The rods show nanoflower-like morphology where they started to grow from a centre point outwards in different directions. At high magnifications, TiO_2 nanorods can be

seen to have rectangular shapes with conical heads (Figure 4.8d). The length of the nanorods ranges between 2-2.5µm with diameters of 100-150nm.

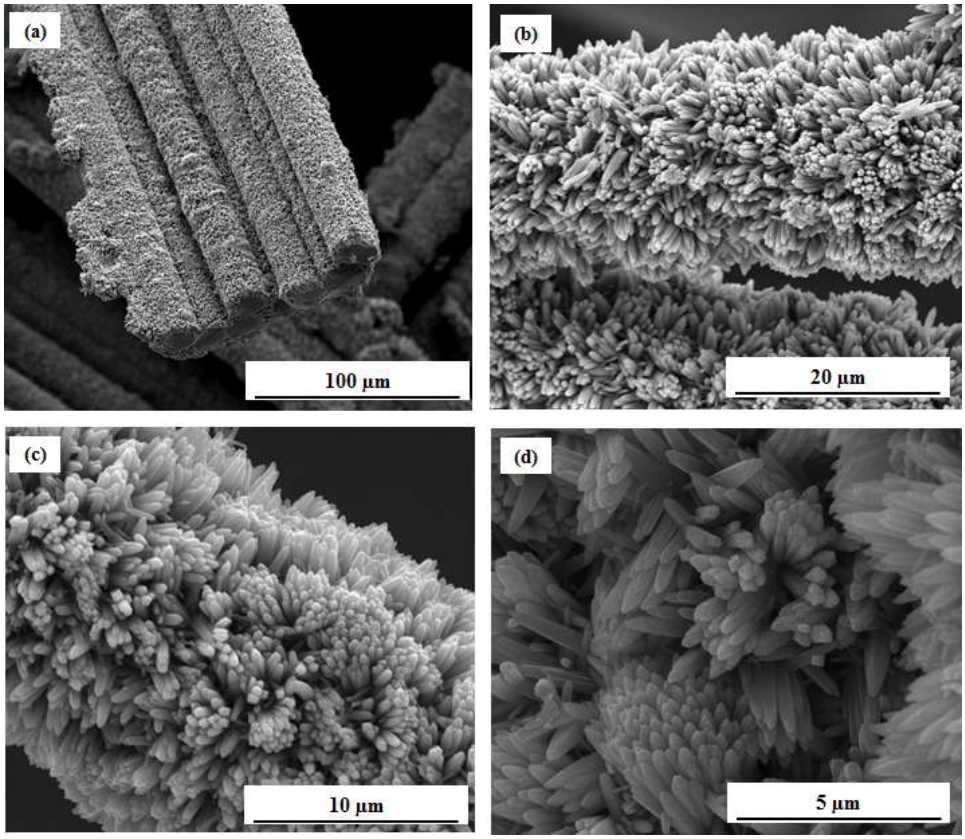

Figure 4.8 SEM micrographs of TiO_2 nanorods hydrothermally grown on glass fibres substrates

The hydrothermal method is one of most commonly used production techniques for producing TiO_2 as it produces highly crystalline and high surface area TiO_2 nanostructures which are beneficial for photovoltaic and photocatalytic applications.[146,147,148] The chemical reactions taking place during the hydrothermal process are as follow in Equations 4.10-4.12. Titania species from the precursor, Titanium Butoxide, react with HCl to form $TiCl_3$. This compound form is not stable in aqueous solutions; therefore, $TiOH^{2+}$ is formed by hydrolysis. $TiOH^{2+}$ is further oxidised to Ti (IV) oxygen species which are the growth units for TiO_2:[149]

$$2Ti + 6HCl \rightarrow 2TiCl_3 + 3H_2(g) \qquad \text{Eqn (4.10)}$$

$$2Ti^{3+} + H_2O \rightarrow TiOH^{2+} + H^+ \qquad \text{Eqn (4.11)}$$

$$TiOH^{2+} + O_2^- \rightarrow Ti(IV) - oxo\ species + O_2^- \rightarrow TiO_2 \qquad \text{Eqn (4.12)}$$

The samples were further annealed at 600ºC for 3h to investigate whether there was an effect on morphological and crystal structure and the corresponding photocatalytic activity. Figure 4.9 shows the SEM micrographs of the as-grown TiO_2 nanorods and the annealed TiO_2 nanorods hydrothermally grown on glass fibre substrates. The arrays of nanorods become denser for the annealed TiO_2 sample where aggregation occurred during annealing. This is because the size of the crystallite sites of TiO_2 grows bigger with increasing temperature. Bigger crystallites results in more compact nanorods.

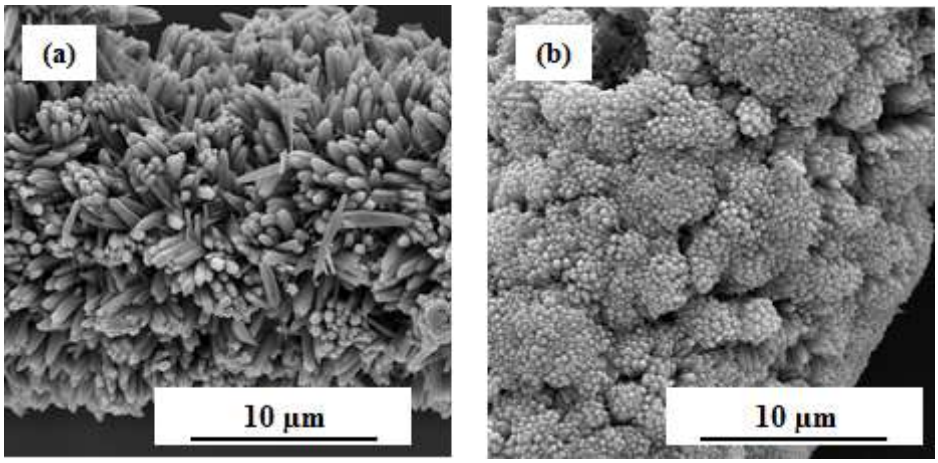

Figure 4.9 SEM micrographs of (a) as-grown TiO_2 nanorods and (b) annealed TiO_2 nanorods (600ºC, 3h) hydrothermally grown on glass fibre substrates

X-Ray diffraction (XRD) analysis was used to investigate the phase composition of the samples. The XRD patterns of as-grown and annealed TiO_2 on glass fibres are shown in Figure 4.10. All crystalline peaks can be indexed to rutile TiO_2. Broad peaks in between the crystalline peaks belong to the amorphous glass fibre substrate. No phase transformation from rutile to brookite or anatase was observed after

annealing; however, the crystallinity of TiO_2 nanorods was slightly enhanced. The crystalline peaks for planes (002) and (310) have become more distinctive for the annealed TiO_2 sample. This is because heat treatment promotes the energy for atomic diffusion to more thermodynamically stable structural arrangements which implies an enhancement in crystallinity.[150]

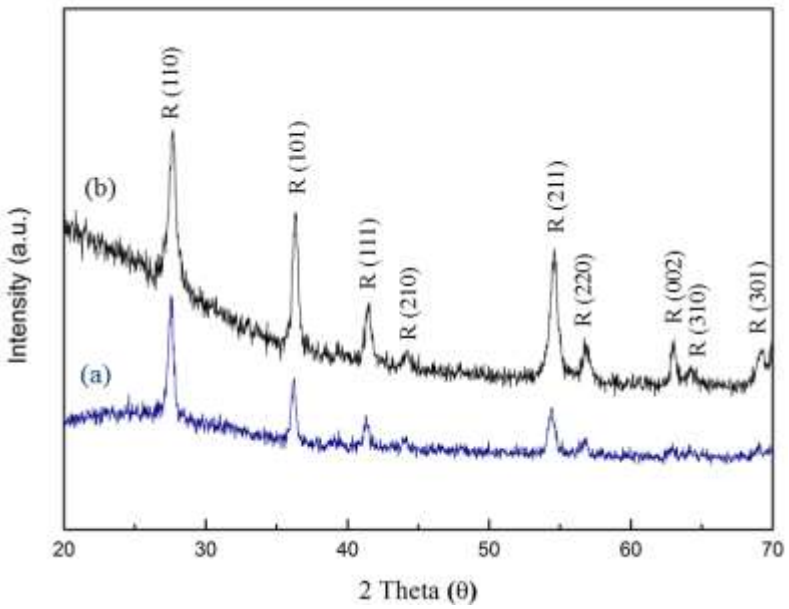

Figure 4.10 XRD patterns of (a) as-grown TiO_2 nanorods and (b) annealed TiO_2 nanorods (600°C, 3h) hydrothermally grown on glass fibre substrates

The surface area of hydrothermally grown TiO_2 nanorods on glass fibres was determined by BET analysis. The analysis indicates a surface area of 1.46 m^2 for TiO_2 per gram of the catalyst/substrate. This was calculated by subtracting the BET surface area of TiO_2 nanorods grown on glass fibres from the surface area of glass fibres without the TiO_2 growth. This value is small compared to commonly used Degussa P25 of which the surface area is approximately 45m^2/g.

Pd nanoparticles were then deposited onto the TiO_2 nanorods using a photochemical process. The glass fibres with TiO_2 nanorods were dipped into a 0.1M $PdCl_2$ solution which is the precursor for the Pd ions. Pd^{2+} ions were reduced to Pd^0 under UV irradiation and were deposited on TiO_2. The electrons that reduce Pd^{2+} to Pd^0 are the

photogenerated electrons at the conduction band of TiO_2 which were excited by UV irradiation:[151]

$$Pd^{2+}\ 2e \xrightarrow{hv\ (UV)} Pd^{0} \qquad \text{Eqn (4.13)}$$

UVA cube was used for metal nanoparticle deposition on TiO_2 nanorods. A mercury lamp that was placed in metal housing was used as UV irradiation source (Honle UV Technology, UVA Cube 100). The housing dimensions are 24cm x 23cm x 20cm and the inner part of the housing is covered with an aluminium shade for reflection. The spectrum of the UVA cube is shown in Figure 4.11.

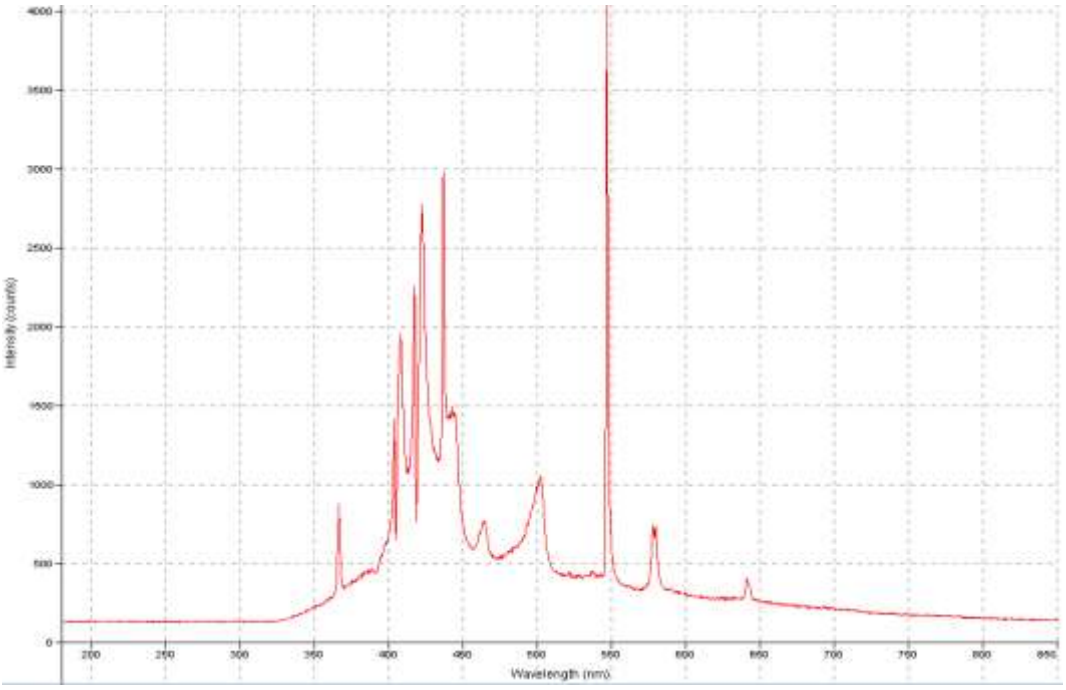

Figure 4.11 Spectrum of UVA Cube

The colour of the TiO_2 samples changed from white to brown after Pd deposition (Figure 4.12):

Figure 4.12 Colour change after Pd deposition on TiO_2 nanorods on glass fibre substrates

Pd nanoparticles were not observed during SEM imaging due to its nanoscale size. However, EDX analysis used for elemental composition detected the presence of Pd with a content of 0.78 wt% and 0.17at% (Figure 4.13). Elemental composition of the sample in atomic and weight percentages are shown in Table 4.1:

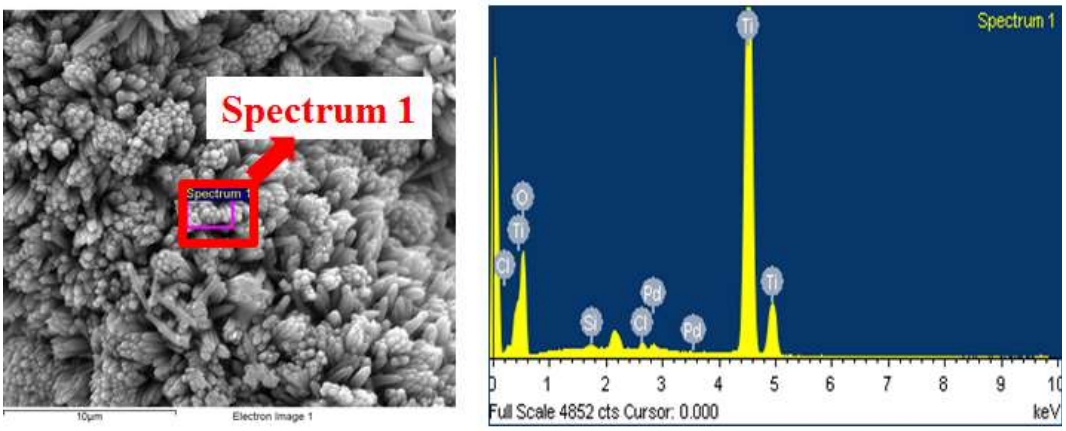

Figure 4.13 SEM micrograph of Pd deposited TiO_2 nanorods hydrothermally grown on glass fibres and corresponding EDX analysis of the selected area

Table 4.1 Elemental Composition of Pd/TiO_2 nanorods on glass fibre substrates

Element	Weight (%)	Atomic (%)
O	50.99	75.76
Si	0.15	0.13
Cl	0.44	0.30
Ti	47.64	23.64
Pd	0.78	0.17

The morphology of the photochemically deposited Pd nanoparticles can be observed by TEM imaging. The nanoparticles were distributed on the sides of the nanorods. The high resolution images show that the Pd nanoparticles are spherical in shape with a diameter ranging between 5 and 10nm (Figure 4.14).

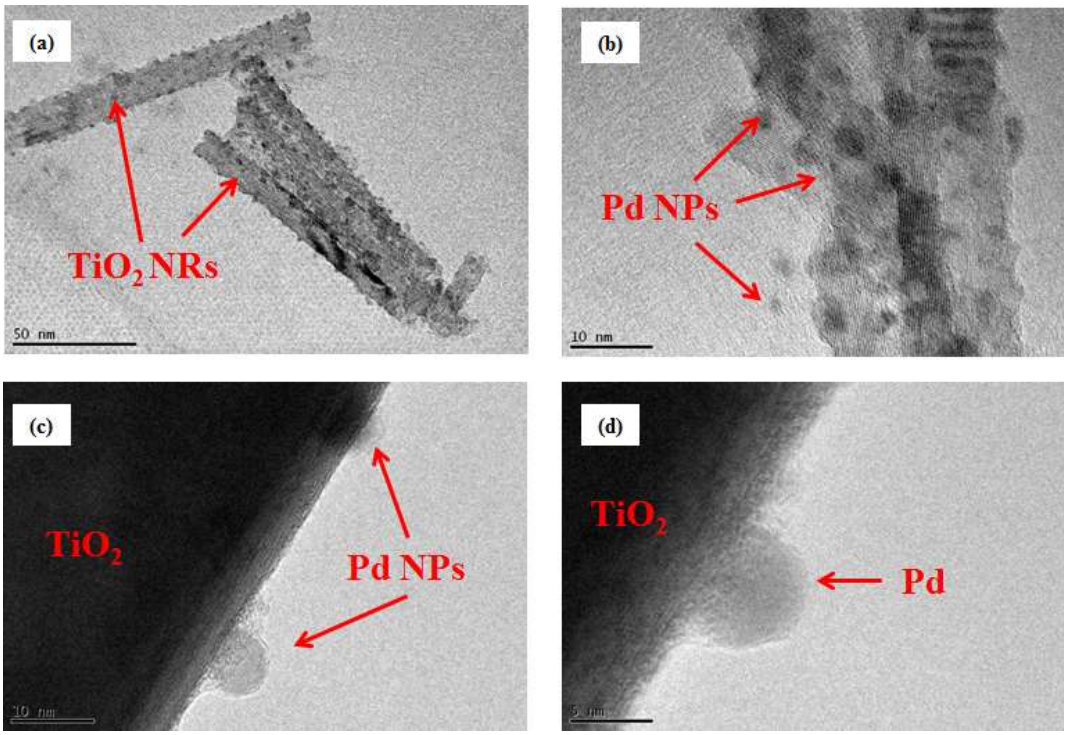

Figure 4.14 TEM images of Pd nanoparticles deposited on TiO_2 nanorods: (a) (b) Spherical shaped Pd nanoparticles were distributed onto the TiO_2 nanorods on glass fibres. (c) (d)Pd nanoparticle at high magnifications shows a diameter of 5-10nm

Further characterisation was performed using XPS where the surface elemental compositions were analysed. The XPS spectra confirmed the existence of Pd along with Ti and O from the photocatalyst. Peaks for elements such as Si and Cl were obtained from the glass fibre substrate (Figure 4.15).

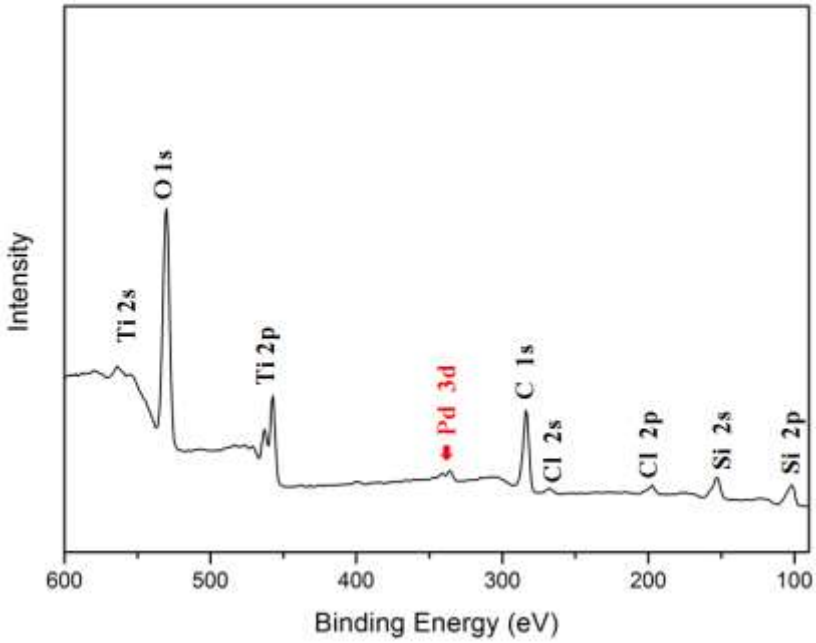

Figure 4.15 XPS spectra of Pd/TiO_2 nanorods hydrothermally grown on glass fibres: the existence of Pd was confirmed

High resolution spectrum of Pd shows that the spin orbit splitting of 3d is 5.2eV with two characteristic peaks at $3d_{3/2}$=340.9eV and $3d_{5/2}$=335.7eV (Figure 4.16). The peak values confirmed that the Pd deposited onto TiO_2 nanorods is in the metallic Pd^0 form.[152,153,154] Pd was not oxidised into PdO during deposition under irradiation.

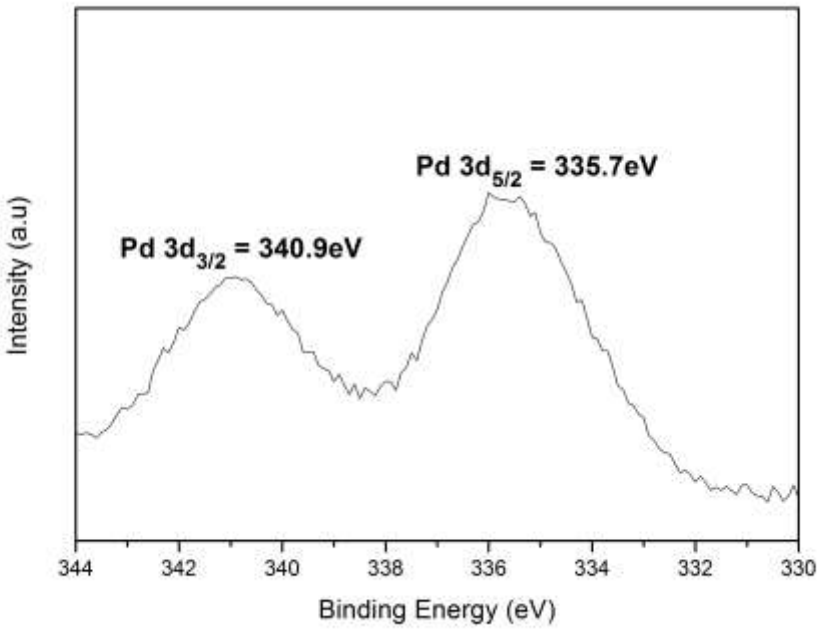

Figure 4.16 High resolution XPS spectrum of Pd 3d: Binding energies confirm the existence of metallic Pd^0

Figure 4.17 shows the normalised absorbance curves for TiO_2 and Pd/TiO_2 structures grown on glass fibre substrates. It can be clearly seen that TiO_2's optical response, which is limited to UV light, was shifted and widened to the visible light range. This is due to the plasmonic interaction of Pd nanoparticles with visible light. To show this interaction, a fitting curve for the plasmon peak was plotted in the absorbance curves. A plasmon peak can be observed at 425nm.

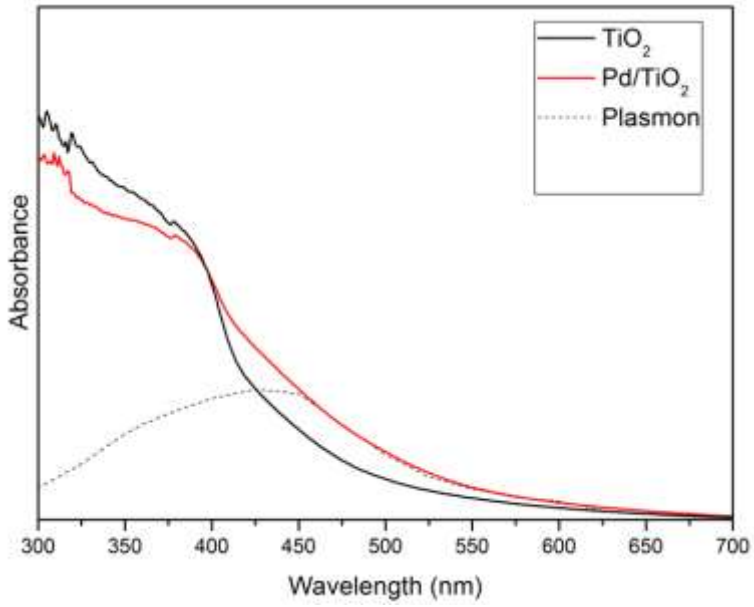

Figure 4.17 UV-Vis spectroscopy for absorbance curves of as-grown TiO_2 and Pd deposited TiO_2 nanorods on glass fibre substrates

4.3. Effect of Crystallisation on Photodecolourisation of RhB

The photocatalytic activity of the as-grown TiO_2 nanorods on glass fibres and the effect of annealing were investigated by the decolourisation of RhB. 8 samples (0.7cm x 7cm) were dispersed in 30ml of RhB (10ppm) under a solar simulator. The system was kept in the dark for 30 minutes prior to illumination to provide the adsorption equilibrium between the dye molecules and catalyst system. Dye solution samples were taken at certain intervals and kept in sample tubes for analysis by UV-Vis Spectroscopy. The UV-Vis absorption spectra of the RhB dye solution was taken at specific time intervals during decolourisation with as-grown TiO_2 nanorods (Figure 4.18). The drop in absorption intensity at different irradiation times can be clearly seen which indicates that the decolourisation of RhB by the photocatalyst system was successfully achieved. The maximum absorption peak of RhB solution (10ppm) is at 554nm. The absorption value at 554nm for zero minutes was taken as C_0 which belongs to the sample solution just before exposure to illumination. The

absorption values for other sample solutions were taken as C_i for irradiation times at i^{th} minutes. These values were used to calculate the decolourisation profile using Beer-Lambert law which assesses the direct proportional relation between absorption and dye concentration.

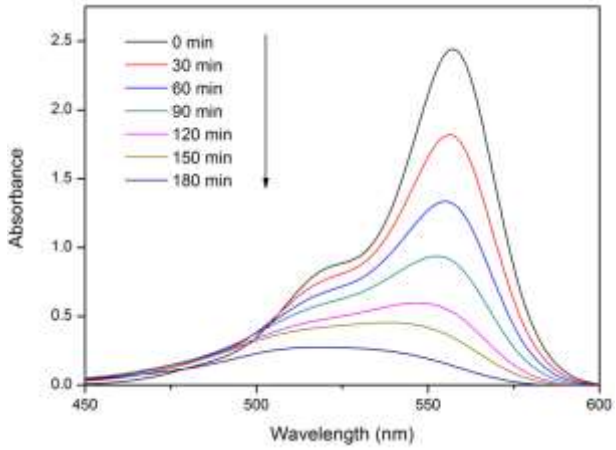

Figure 4.18 UV-Vis absorption spectra of RhB solution at different times under illumination with as-grown TiO_2 nanorods on glass fibre substrates

The colour change of the dye solution at different irradiation times can be seen clearly whereby the solution became transparent by the end of the process (Figure 4.19).

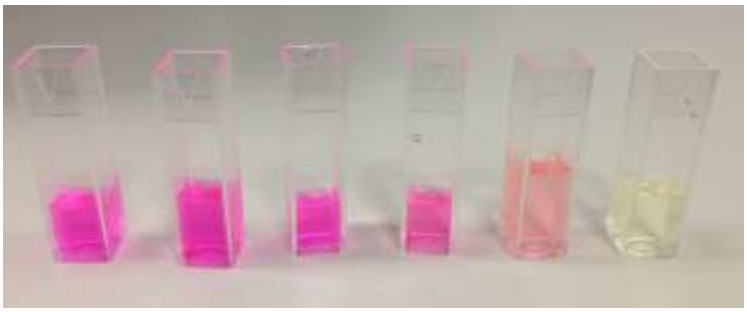

Figure 4.19 Sample dye solutions taken at different irradiation times for UV-Vis Spectroscopy

The photodecolourisation curves of RhB by the as-grown TiO_2 nanorods and the annealed TiO_2 nanorods hydrothermally grown on glass fibre substrates are shown in Figure 4.20. The photocatalytic performance of the two samples was similar giving

full decolourisation within 3 hours. A slight improvement in photoreactivity was expected by the annealed TiO_2 samples. This is because annealing enhances crystallinity and reduces crystal defects which decreases the probability of electron and hole recombination.[155] The slight enhancement crystallinity in annealed TiO_2 catalyst system was confirmed by the XRD pattern (Figure 4.10). However, the photodecolourisation curves of RhB by samples show that the annealing did not have any effect on the photoactivity. This is because the slight enhancement in crystallinity of TiO_2 nanorods was apparently not significant enough to make a noticeable difference. The annealing process was then decided to be unnecessary and further photocatalysis experiments were conducted with as-grown TiO_2 samples.

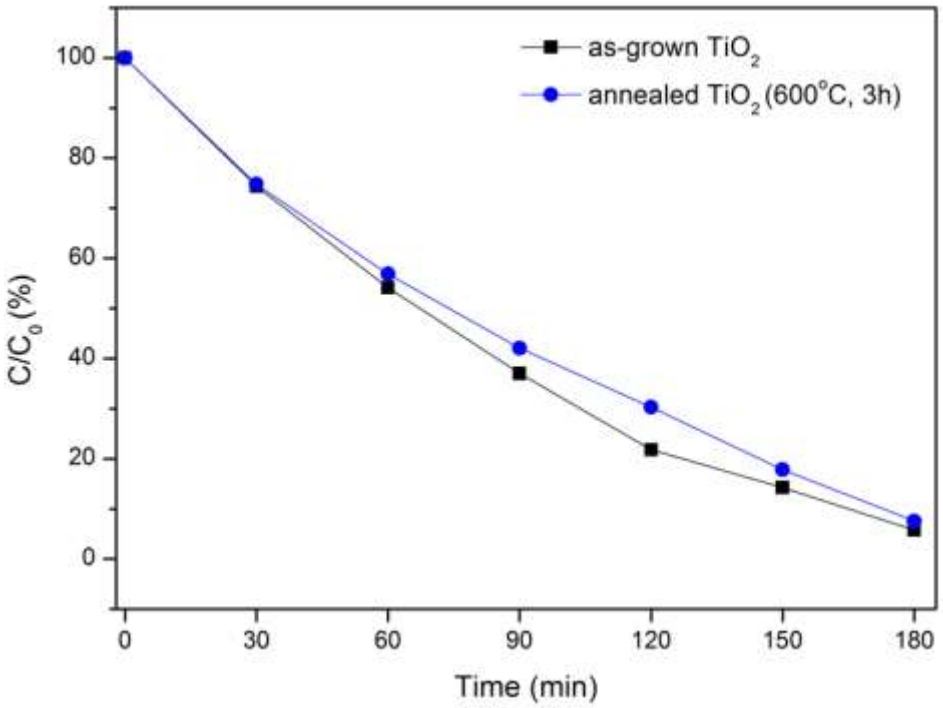

Figure 4.20 Photodecolourisation curves of RhB with as-grown TiO_2 and annealed TiO_2 nanorods (600°C, 3h) on glass fibre substrates

The reaction pathways for the photodegradation of dye molecules have been previously reported in literature. These reports have studied the reaction intermediates where intermediate species were detected by spectroscopy techniques such as Electronic Paramagnetic Resonance (EPR), Nuclear Magnetic Resonance (NMR) and Gas Chromatography (GC).[156,157] The proposed mechanism for photocatalysis of RhB by TiO_2 is shown in Figure 4.21.[146] The photons are absorbed by TiO_2 and electrons are excited to the CB which leaves holes in the VB. The electrons are also injected from the dye into the CB as the LUMO level of RhB has a higher energy than the CB of TiO_2. The electrons react with the aqueous solution to form superoxide radical anions ($O_2^{\cdot -}$). Holes are transferred to the dye from TiO_2 as the VB of TiO_2 is lower in energy than the HOMO level of the dye. The aqueous solution is then oxidised by the holes where hydroxyl radicals ($OH^{\cdot}$) are produced. These radicals degrade the RhB dye molecules. The main intermediate degradation product for RhB was reported to be benzoic acid.[48] The redox reactions of the RhB are shown below:

$$TiO_2 + hv \rightarrow e_{CB}^- + h_{VB}^+ \qquad \text{Eqn (4.14)}$$

$$h^+ + OH^- \rightarrow OH^{\cdot} \qquad \text{Eqn (4.15)}$$

$$e^+ + O_2 \rightarrow O_2^{\cdot -} \qquad \text{Eqn (4.16)}$$

$$RhB + OH^{\cdot} + O_2^{\cdot -} \rightarrow Dye\ Degradation\ Products \qquad \text{Eqn (4.17)}$$

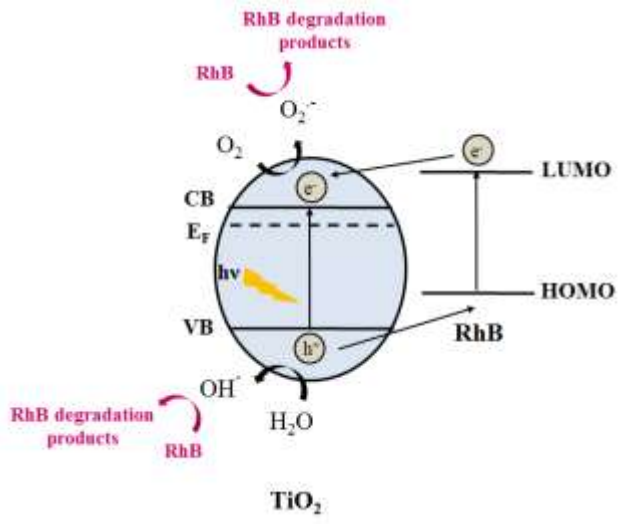

Figure 4.21 Proposed mechanism for RhB decolourisation by TiO_2

4.4. Effect of Pd Nanoparticle Deposition on Photodecolourisation of RhB

The effect of Pd nanoparticle deposition on the photoactivity of TiO_2 was investigated through the photodecolourisation of RhB. The system was again kept in the dark for 30 minutes prior to illumination to provide the adsorption equilibrium. The concentration change of the dye solution after 30 minutes in the dark for the equilibrium state was calculated. It was found that the concentration dropped after 30 minutes. The amount of concentration change is an important aspect in photocatalysis as it indicates the degree of dye molecules adsorbed on the catalyst surface which influences the photocatalytic activity.

For the as-grown TiO_2 nanorods, the adsorption percentage was calculated to be 3% whereas it was 6% for Pd/TiO_2. This is related to the surface area and active sites of the photocatalyst system. Pd/TiO_2 hybrid catalyst samples have more active sites for dyes molecules compared to bare TiO_2 as the deposition of Pd nanoparticles onto the TiO_2 increased the surface area of the catalyst system. More active sites indicate an

increased charge transfer to the dye molecules for redox chemistry. This leads to an increase in photocatalytic activity.

Figure 4.22 shows the decolourisation curves for RhB (10ppm) by as-grown TiO_2 and Pd deposited TiO_2 grown on glass fibres. Full decolourisation within 3 hours was achieved by the as-grown TiO_2 under visible light irradiation. This time was improved to 90 minutes by the hybrid catalyst Pd/TiO_2.

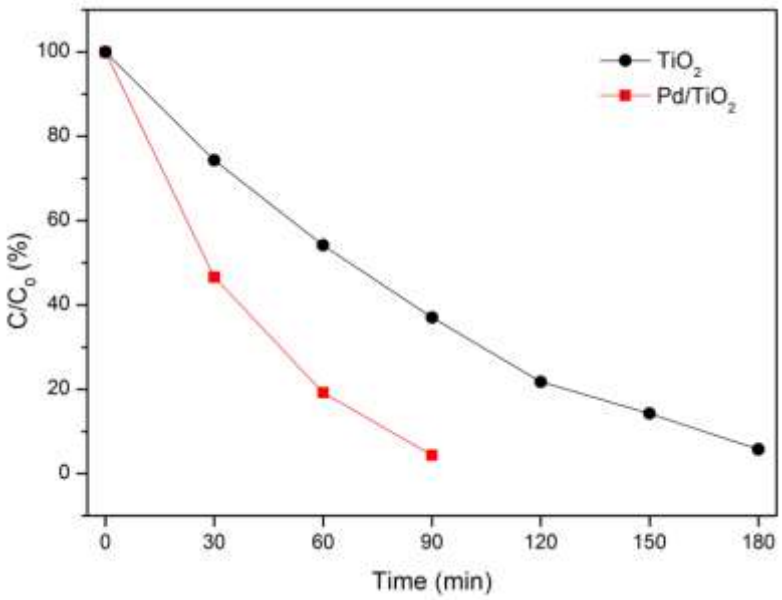

Figure 4.22 Photodecolourisation curves of RhB with as-grown TiO_2 and Pd deposited TiO_2 nanorods on glass fibre substrates

Figure 4.23 shows the first-order kinetics for RhB decolourisation by the as-grown TiO_2 and Pd deposited TiO_2 grown on glass fibre substrates where a linear relation was sought between the concentration changes and the time. A straight line was fitted between the data points. The last data points however deviate from the first order kinetics and are unfitting to the drawn straight line. This can be ascribed to the agglomeration of the undegraded dye molecules on the catalyst surface and dye intermediates competing at the active surface sites.[158] Therefore, the initial the concentration changes in the first hour were used in order to calculate the k_{app} values

for each sample. The calculated kinetic rates for both systems are shown in Table 4.2. It has been observed that the kinetic rate was doubled by the Pd deposition to the bare TiO_2 catalyst system.

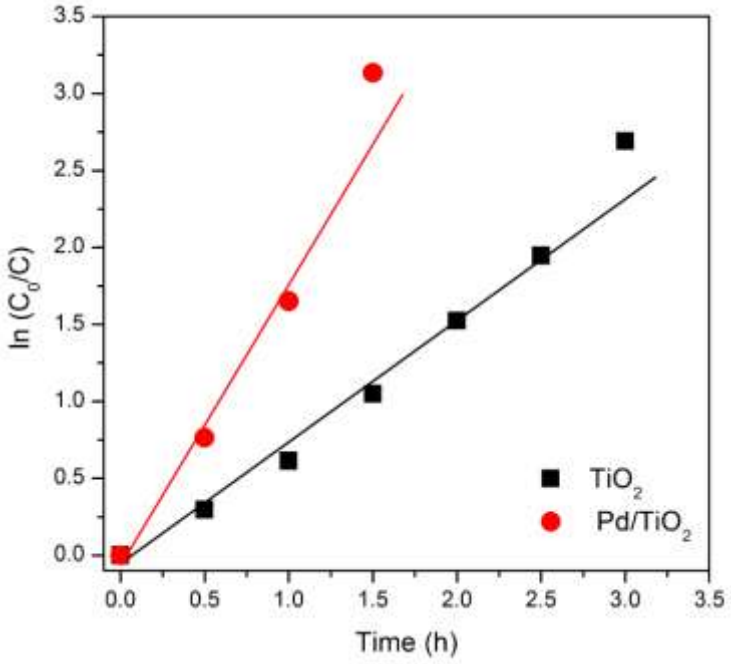

Figure 4.23 Kinetic rates for RhB decolourisation with as-grown TiO_2 and Pd deposited TiO_2 nanorods on glass fibre substrates

Table 4.2 Calculated k_{app} values for TiO_2 and Pd deposited TiO_2 nanorods on glass fibre substrates

Catalyst	Kinetic Rate (k_{app})
TiO_2	0.013
Pd/ TiO_2	0.029

The superior performance of Pd/TiO_2 compared to the as-grown TiO_2 was attributed to two prominent features; the interaction of Pd nanoparticles with visible light through localised surface plasmon resonance (LSPR) and the enhanced charge separation due to Pd nanoparticles acting as electron sinks.

LSPR results from the interaction of Pd nanoparticles with visible light. According to the fundamental mechanism of LSPR effect, the free electrons of Pd that are in

resonance with the incoming photon get excited with varying electric field of the photon. If the photoexcited electrons have energy higher than that of the conduction band of TiO_2, they are then directly transferred to the conduction band. The electrons respond to the visible right provided that the size of the Pd nanoparticles can be tailored in the visible range. The oscillations of these electrons by the surrounding electric field lead to a stronger absorption in the visible range. The red shift to optical absorption in visible light range by Pd/TiO_2 was shown in Figure 4.17. This leads to an increase in charge generation compared to bare TiO_2 of which optical response is limited to UV light – only 5% of the total solar energy. On the other hand, the hybrid catalyst system of Pd/TiO_2 is receptive to visible light which compromises 50% of solar energy. Therefore, a greater number of charge carrriers are excited. Enhanced availability of photoactive charge carriers corresponds to an increase of redox reactions with the dye solution, that is, an increase in photocatalytic activity (Figure 4.24a).

The separation of the photoinduced electron and hole pairs is also improved by the Schottky junction that is formed at interface of TiO_2 nanorods and Pd nanoparticles. The Fermi level of Pd is below the conduction band of TiO_2 (E_F = 0.8eV at RHE).[159] Hence, the transfer of electrons from TiO_2's CB to Pd is thermodynamically favourable. The electrons are therefore scavenged by Pd from the conduction band of TiO_2 and then directly injected into the adsorbed dye molecules from the metal which leaves photoactive holes in behind. This leads to efficient charge separation of the electrons and holes which prohibits the recombination at lower energy states. Suppressed recombination increases the amount of photoactive charge carriers and eventually results in higher photoactivity (Figure 4.24b).

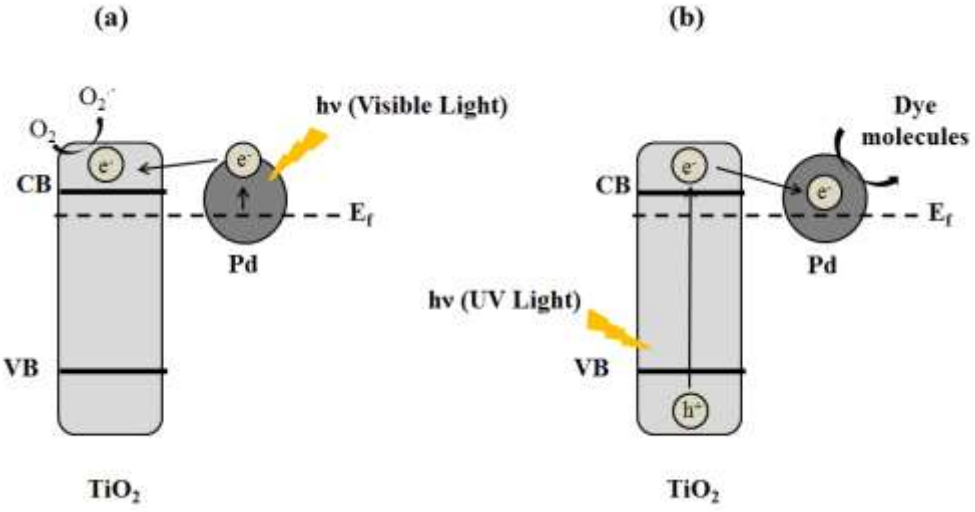

Figure 4.24 Proposed mechanism for charger transfer and dye decolourisation with Pd/TiO_2 system under (a) visible light for LSPR effect and (b) under UV light for charge trapping

4.5. Recyclability Test

The photodegradation experiments were repeated under the same conditions with the used samples to test the recyclability of the catalysts. The used samples were left in DI water under solar simulator overnight and were then dried in air. Figure 4.25 shows the decolourisation curves with the repeated experiments under same conditions for TiO_2 and Pd/TiO_2. Reused Pd/TiO_2/glass fibres hybrid catalyst showed a good catalytic performance that implies a good recyclability. Full decolourisation of RhB was achieved within 120 minutes compared to 90 minutes by the original Pd/TiO_2. However, the reuse of native TiO_2/glass fibres showed poorer photocatalytic efficiency compared to the original samples. Additionally, it has been observed that the order of kinetics has vastly deviated from the first order kinetics that the original samples have followed. This could be related to the accumulation of the adsorbed dye molecules on the surface after the initial photodecolourisation process. The

clusters of dye molecules cover the active sites of the photocatalysts and inhibit the penetration of light and charge transfer for the redox chemistry.

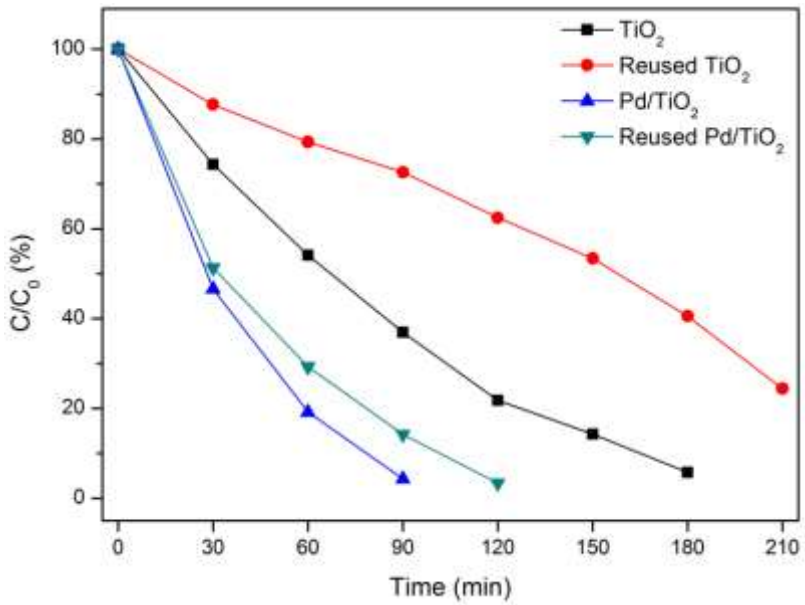

Figure 4.25 Photodecolourisation curves of RhB(10ppm) with repeated samples of as-grown TiO_2 and Pd deposited TiO_2 nanorods on glass fibre substrates

4.6. Summary

This chapter has outlined the development of a mechanically robust photocatalyst system which can be used as a photocatalytic filter for waste water treatment and dye degradation. The photocatalytic activity of system was studied through the decolourisation of a textile dye Rhodamine B. The photocatalyst system consisted of TiO_2 nanorods immobilised on glass fibre supports. Two different fabrication methods were used to produce such system. Firstly, an aqueous method of conversion of ZnO nanorods to TiO_2 nanorods was used. The photocatalyst failed to show a good photocatalytic activity due to insufficient crystallinity and stability. Therefore, the production method was altered to a hydrothermal method. By hydrothermal process, high surface area TiO_2 nanorods were successfully grown on

glass fibre substrates. Full decolourisation was achieved within 3 hours with as-grown TiO_2 nanorods. The photoactivity of the system remained unchanged after annealing. Furthermore, Pd nanoparticles were deposited onto TiO_2 nanorods via photochemical method to enhance photoreactivity of bare TiO_2. Successful deposition of Pd was shown by characterisation methods such as SEM, EDX, TEM and XPS. It was found that the hybrid Pd/TiO_2 catalyst system showed higher photoactivity with a doubled kinetic rate. Full decolourisation occurred within 180 minutes with TiO_2 whereas it was only 90 minutes for Pd/TiO_2. This enhancement in photoactivity was attributed to the electron trapping role of Pd with efficient charge separation and localised surface plasmon resonance (LSPR) effect due to interaction of Pd with visible light. The shift from UV light to visible light in the catalyst's optical response was shown by UV-Vis spectroscopy. The recyclability of the samples was also tested by reusing the samples under the same experimental conditions. Reused Pd/TiO_2/glass fibres hybrid catalyst showed a good catalytic performance that is similar to the original samples.

CHAPTER 5: PHOTOELECTROCATALYSIS OF RHODAMINE B AND SOLAR HYDROGEN PRODUCTION BY TiO_2 and Pd/TiO_2 CATALYST SYSTEMS

5.1 Introduction

Since the discovery of TiO_2's capability for water-splitting and the photocatalytic degradation of organic compounds, almost every suitable semiconductor has been analysed for environmental and energy applications.[2,160] The most heavily investigated is still TiO_2 due to its chemical stability, low cost and good photocatalytic efficiency.[161] The main drawback of TiO_2 is its limited optical response and high recombination rate of photogenerated holes and electrons. There has been extensive research on a variety of modifications of TiO_2 for improvement to the wavelength range response, efficient charge separation, and redox reactions between the photocatalyst and adsorbed molecules by an efficient charge transfer.[11]

The deposition of precious metals or rare earth metals on semiconductors is one of the most commonly studied methods for photocatalytic enhancement of TiO_2. For TiO_2, Au[88,94] and Ag[87,97] are the most popular noble metals to enhance the photocatalytic activity but photocatalytic studies with Pt,[100,101] Pd[103,102] and Ru[105] have also been reported. However, the photoelectrochemical performance of TiO_2 is not always enhanced by metal deposition. Declines in photoactivity and photocurrent by the addition of Ag[162] and Au[163] onto TiO_2 have been observed. This is related to the complex charge transfer mechanisms between the metal, TiO_2, substrate, counter electrode and the surrounding electrolyte solution. The relative positions of band levels of the semiconductor, work function of the deposited metal and redox potentials of the solution are the key aspects for understanding the mechanism.

Chapter 5 focuses on the photoelectrochemical analysis of bare TiO_2 and Pd/TiO_2 that were synthesized for use in the photoelectrocatalytic degradation of RhB and for solar hydrogen production. Rutile TiO_2 nanorods were grown on FTO coated glass by a hydrothermal method and annealed at 550^oC for 3h. The annealing process immensely improved the photocurrent, and so metallic Pd nanoparticles were photochemically deposited onto annealed TiO_2 nanorods to form the hybrid Pd/TiO_2 photocatalyst system. The analysis of phase composition and morphology of the TiO_2 nanorods and Pd nanoparticles were performed by characterisation methods such as SEM, XRD, TEM and XPS. The samples were then photoelectrochemically analysed using a potentiostat including tests for i-v and i-t measurements under dark and illumination. Mott-Schottky curves for estimation of flat-band potential and electrochemical impedance scpectroscopy (EIS) to understand the charge transfer kinetics at the Pd/TiO_2/electrolyte interface were also performed.

The photoelectrochemical performance of the bare TiO_2 and hybrid Pd/TiO_2 samples were compared through the decolourisation of RhB and through the moles of photogenerated hydrogen gas produced in different electrolyte solutions at various applied voltage values. The solutions used for solar hydrogen production were 0.01M Na_2SO_4 aqueous solution, pure deionised water and methanol solution (methanol:deionised water with 1:4 ratio) at applied voltages of 0V, 0.7V and 1.2V vs NHE. The hybrid photocatalyst Pd/TiO_2 showed enhanced photoelectrocatalytic activity for the decolourisation of RhB in aqueous solution. A higher moles of hydrogen by Pd/TiO_2 was photogenerated in methanol solution. However, bare TiO_2 samples produced a higher amount of hydrogen in 0.01M Na_2SO_4 and pure deionised water under same conditions. These results were explained by the possible

mechanisms of photoelectrochemistry which were proposed for both processes; dye degradation and solar hydrogen production.

5.2. Characterisation of TiO_2 and Pd/TiO_2 Nanorods on FTO coated glass

The morphology of the TiO_2 nanorods hydrothermally grown on FTO coated glass were analysed using SEM imaging. Figure 5.1 shows the SEM micrographs of the as-grown and annealed TiO_2 nanorods (550^{o}C, 3h) on FTO. The SEM micrographs show a highly uniform and densely packed array of nanorods for each sample. The length of the nanorods ranges between 2.2-2.5µm with diameters of 80-100nm. Nanorods appear denser for the annealed TiO_2 sample due to the expansion that occurs during annealing.

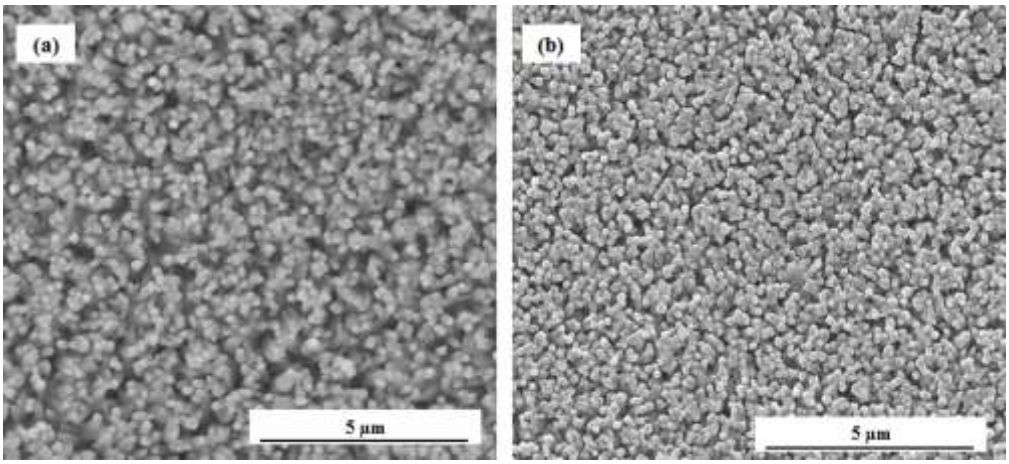

Figure 5.1 SEM micrographs of (a) as-grown and (b) annealed (550^{o}C, 3h) TiO_2 nanorods hydrothermally grown on FTO coated glass substrates

The aggregation of nanorods due to annealing can be seen more clearly in the cross-section SEM micrographs (Figure 5.2). Single nanorods of as-grown TiO_2 can be distinguished clearly whereas annealed nanorods have merged into each other. The crystallite sites of TiO_2 grow larger with heat treatment resulting in greater compaction of nanorods, whereby there is also a slight increase in the diameter.

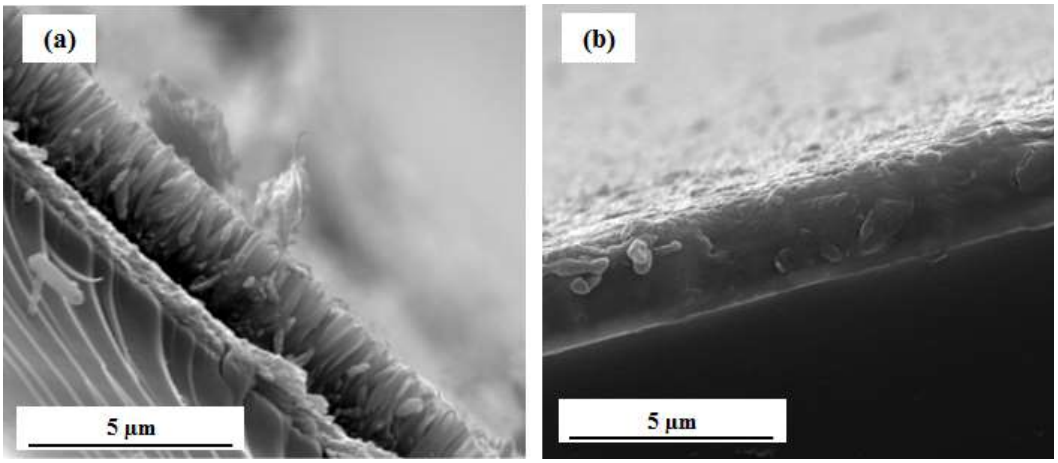

Figure 5.2 SEM micrographs of cross-section of (a) as-grown and (b) annealed (550°C, 3h) TiO_2 nanorods hydrothermally grown on FTO coated glass substrates

X-Ray diffraction (XRD) analysis was used to investigate the phase composition of the samples. The XRD patterns of the as-grown and annealed TiO_2 hydrothermally grown on FTO are shown in Figure 5.3. All crystalline peaks of TiO_2 can be indexed to the rutile phase whereby the remaining peaks are ascribed to FTO substrate (SnO_2). As it can be seen from the XRD patterns, there was a significant increase in crystallinity after annealing where the peaks observed are more distinctive with increased intensities post annealing. Similar to the discussion for the heat treatment of TiO_2 nanorods grown on glass fibres, the enhancement of crystallinity is a result of more thermodynamically stable structural arrangements developing within the nanorods, due to the diffusion of atoms promoted by the heat.

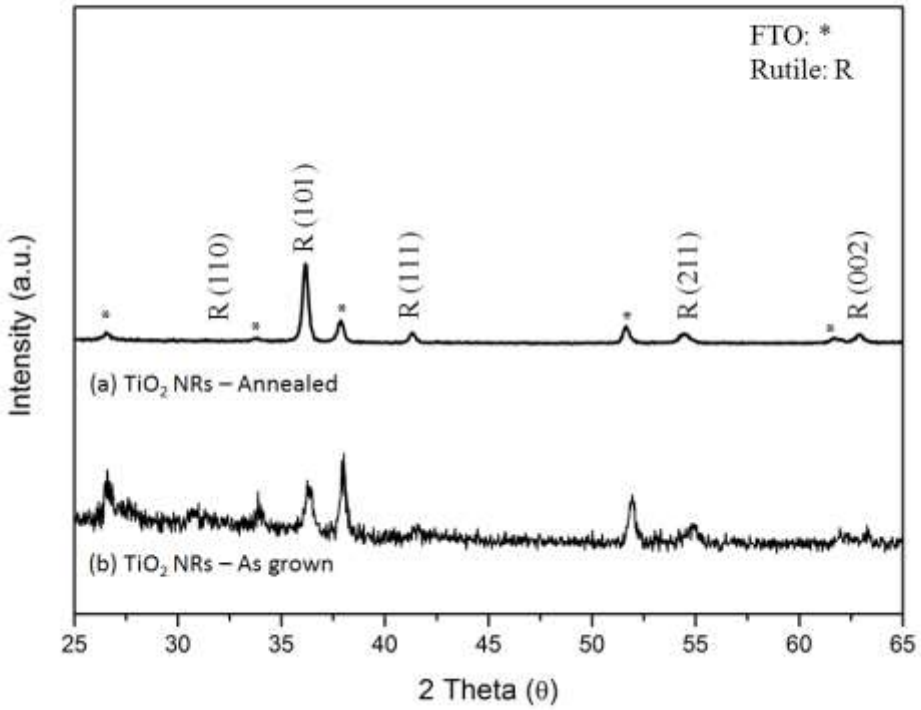

Figure 5.3 XRD patterns of (a) annealed (550ºC, 3h) and (b) as-grown TiO_2 nanorods hydrothermally grown on FTO coated glass substrates. R: Rutile, *: SnO_2.

The photocurrent produced by the as-grown and annealed TiO_2 nanorods under dark and light conditions was investigated. Significantly higher photocurrent was obtained by the annealed TiO_2 nanorods which will be discussed in details in the next section. Further modifications to the TiO_2 such as Pd loading and PEC experiments such as photoelectrocatalysis of Rhodamine B and solar hydrogen production have been performed using the annealed TiO_2 nanorod samples.

Pd nanoparticles were deposited onto the annealed TiO_2 nanorods using a photochemical process. The TiO_2 nanorods were dipped into a 0.01M $PdCl_2$ solution which was then irradiated under UVA Cube for 30 seconds from above and below the sample. Pd^{2+} ions from the precursor $PdCl_2$ were reduced to Pd^0 by the

photogenerated electrons at the conduction band of the TiO_2, represented in Equation 5.1.:

$$Pd^{2+}\ 2e \xrightarrow{hv\ (UV)} Pd^{0} \qquad \text{Eqn (5.1)}$$

The Pd nanoparticle deposition onto TiO_2 nanorods did not affect the morphological structure as observed by SEM imaging (Figure 5.4). Pd nanoparticles couldn't be observed under SEM imaging or EDX which is due to the nanosize of the deposited Pd nanoparticles (<10nm) and the low quantity deposited, which is below the detection threshold of EDX.

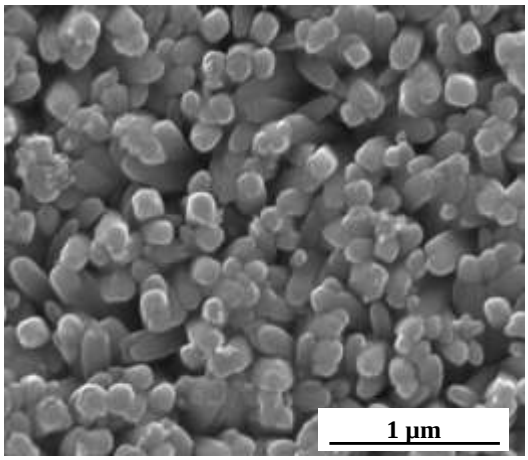

Figure 5.4 SEM micrographs of Pd/TiO_2 samples. Pd couldn't be observed under SEM imaging

However, the morphology of the photochemically deposited Pd nanoparticles was observed under TEM imaging. TEM images show that the photochemically deposited Pd nanoparticles were distributed on the sides of the nanorods (Figure 5.5a). The high resolution images in Figure 5.5b show that the Pd nanoparticles deposited are spherical in shape with a diameter ranging between 5 and 10nm.

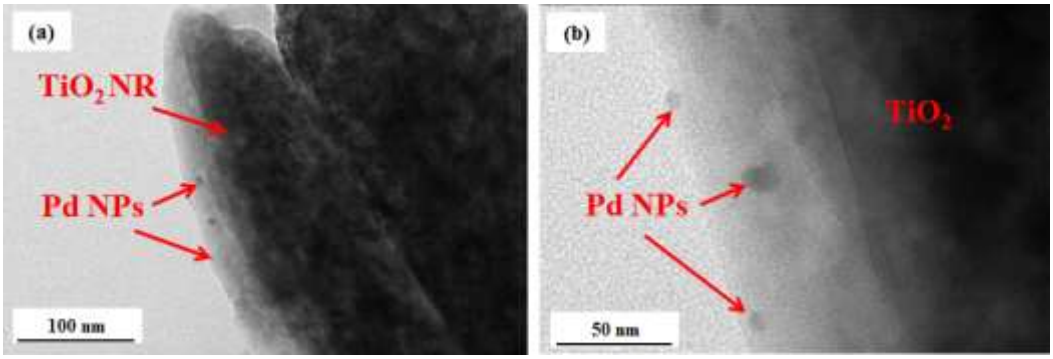

Figure 5.5 TEM micrographs of Pd nanoparticles photochemically deposited onto TiO_2 nanorods hydrothermally grown on FTO coated glass substrate

The phase composition of the TiO_2 and Pd/TiO_2 samples was analysed using XRD. Figure 5.6 shows the XRD patterns of TiO_2 and Pd/ TiO_2, whereby again the Pd was not detected among the peaks for rutile and the substrate. This is due to the fact that the amount of Pd incorporated was below the detection threshold of XRD.

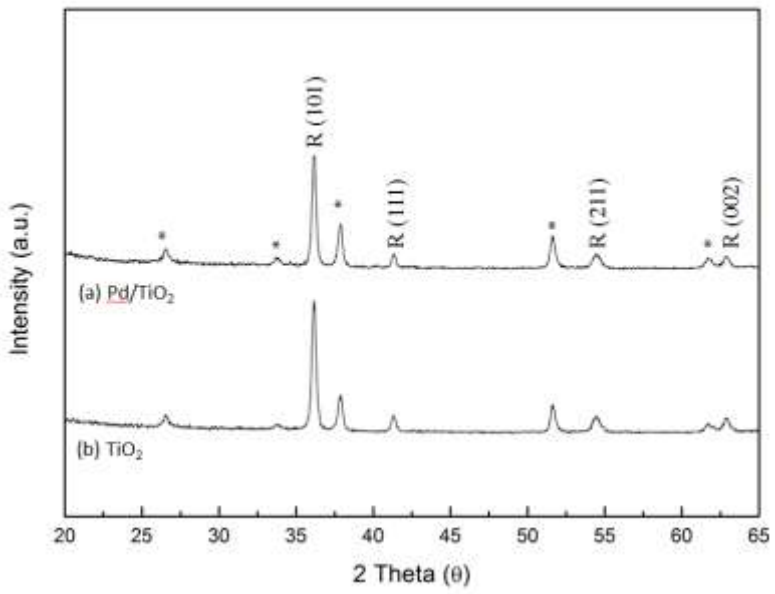

Figure 5.6 XRD pattern of TiO_2 and Pd/ TiO_2 on FTO coated glass. There was no observable change and Pd peak was not observed. R: Rutile, *: SnO_2

XPS was performed to confirm the existence and valence state of Pd deposited onto the TiO_2 nanorods. High resolution XPS spectra in Figure 5.7 for Pd shows the two characteristic peaks at $3d_{3/2}$=340.20eV and $3d_{5/2}$=335.08eV. The spin orbit splitting

of Pd's 3d is 5.12eV. These characteristic peak values confirmed that the Pd deposited onto TiO_2 nanorods is in the metallic Pd^0 form. The oxidation of Pd did not occur during deposition under irradiation.

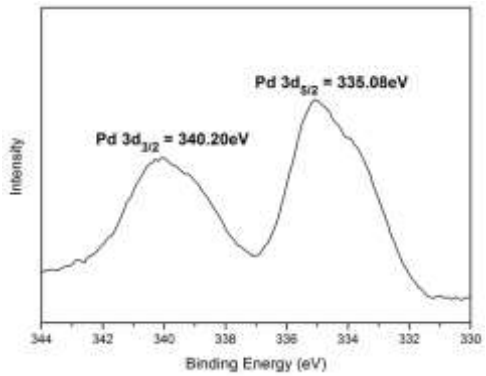

Figure 5.7 High resolution XPS spectrum of Pd 3d: The existence of metallic form of Pd^0 was confirmed by the characteristic binding energies

Figure 5.8 shows the normalised absorbance curves for TiO_2 and Pd/TiO_2 structures grown on FTO coated glass substrates determined by UV-Vis spectroscopy. It can be clearly seen that the optical response of TiO_2, which is limited to UV light, has been shifted and widened to within the visible light range. This is due to the plasmonic interaction of the Pd nanoparticles with visible light.

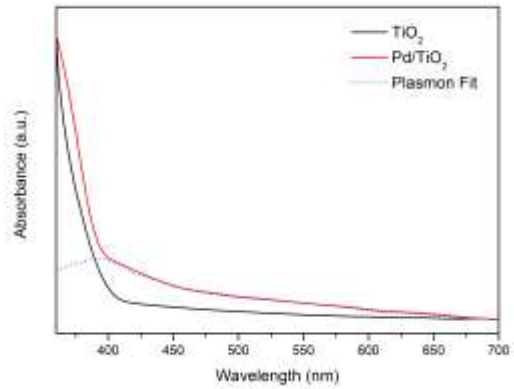

Figure 5.8 UV-Vis spectroscopy for absorbance curves of as-grown TiO_2 and Pd /TiO_2

5.3. Photoelectrochemical Measurements

5.3.1. Mott-Schottky Plots

Figure 5.9 displays the Mott-Schottky plot for TiO_2 nanorods hydrothermally grown on FTO coated glass. As expected, n-type behaviour was exhibited by TiO_2 and confirmed by the positive slope of the curves. The flat band potential of TiO_2 was estimated to be -065V vs Ag/AgCl (-0.45V vs NHE). This value is more negative than the hydrogen reduction level.

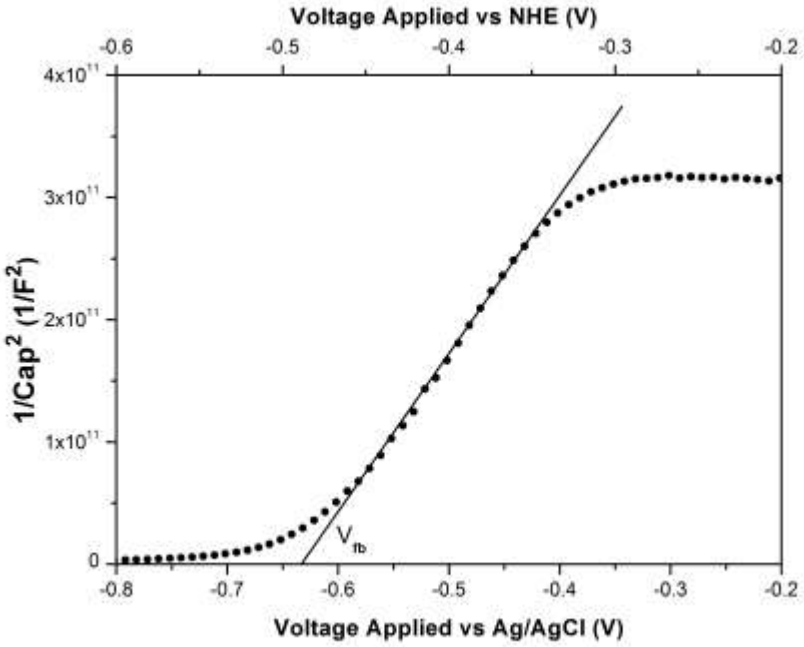

Figure 5.9 Mott-Schottky plots for TiO_2 nanorods hydrothermally grown on FTO coated substrate. The measurement was taken in the dark in an electrolyte solution of 0.01M Na_2SO_4

Figure 5.10 shows the Mott-Schottky plot for TiO_2 obtained at different frequencies. The frequency mentioned here is the frequency of the AC potential applied to the electrochemical cell when measuring the capacitance of the space charge layer. All curves extrapolate to the same flat band potential value.

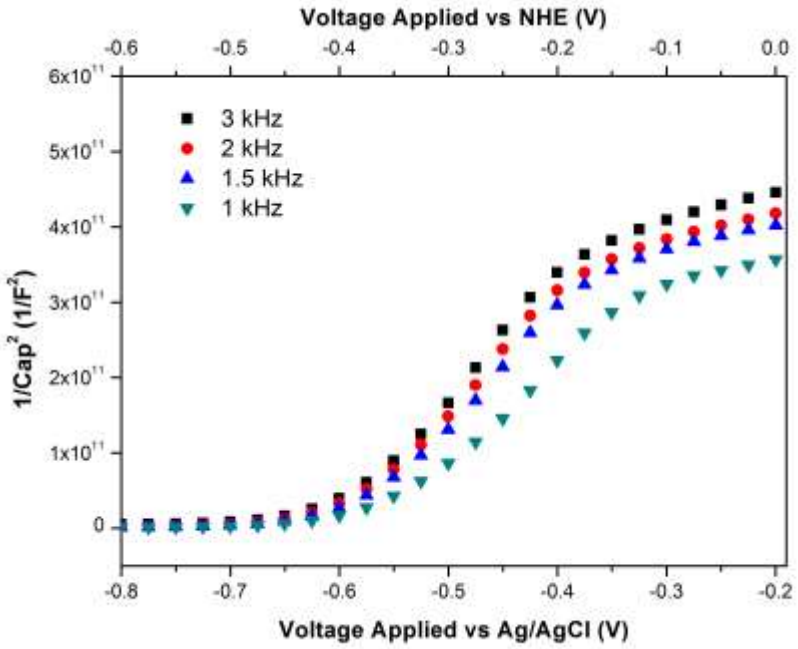

Figure 5.10 Mott-Schottky plots for TiO_2 nanorods hydrothermally grown on FTO coated substrate. The measurements were taken in the dark at different frequencies in an electrolyte solution of 0.01M Na_2SO_4

The theory of Mott Schottky suggests that the flat band potential should be independent of this frequency according to the Equation 5.2:

$$\frac{1}{C_{SC}^2} = \left(\frac{2}{\varepsilon\varepsilon_0 e N_D}\right)\left(V_B - V_{fb}\right) \qquad \text{Eqn (5.2)}$$

where V_B is the applied potential and V_{fb} is the flat band potential. ε is the relative permittivity of the semiconductor, ε_0 is the vacuum permittivity, e is the electron charge and N_D is the donor density.

Figure 5.11 displays the Mott-Schottky plots for TiO_2 and Pd/TiO_2 nanorods hydrothermally grown on FTO. There was a slight positive shift for the E_{fb} value after Pd nanoparticle deposition. This is related to Schottky junction formed at the Pd/TiO_2 interface as the Fermi level of Pd (+0.4V vs NHE, pH=0) is below the conduction band of TiO_2 (-0.1V vs NHE, pH=0) which causes a decrease in the band bending leading to a positive shift in the Fermi level.

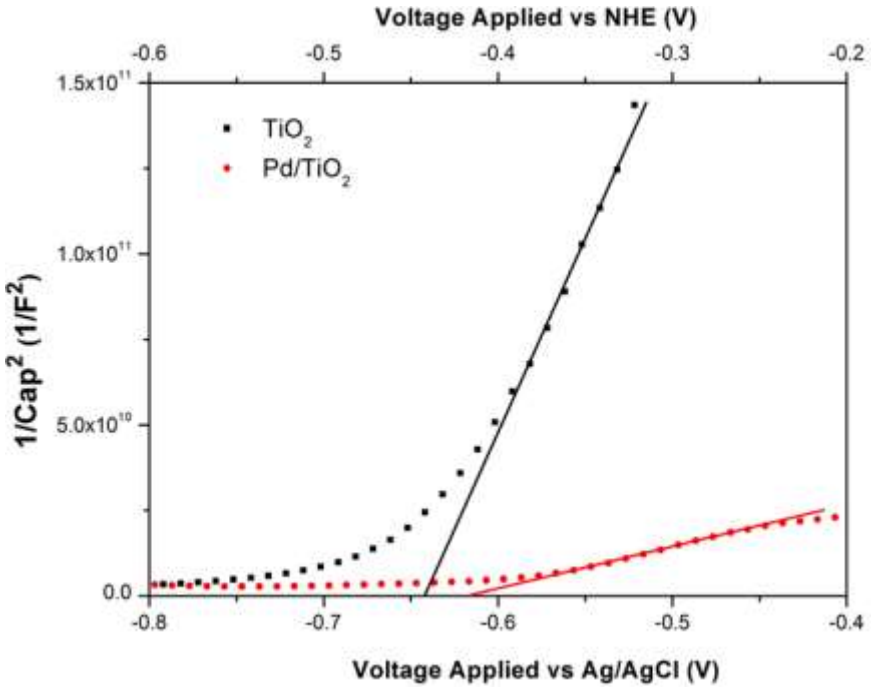

Figure 5.11 Mott-Schottky plots for TiO_2 nanorods hydrothermally grown on FTO coated substrate. The measurement was taken in the dark at different frequencies in an electrolyte solution of 0.01M Na_2SO_4

The decrease in band bending by the addition of Pd is illustrated in Figure 5.12. Figure 5.12a shows TiO_2 band levels before and after contact with the electrolyte. Due to the n-type conductivity of TiO_2, the conduction and valence band are bent upward until the redox potentials of the semiconductor and the electrolyte are aligned. The addition of Pd to the system, which has its own Fermi level, alters the redox potential alignment. $E_{F,Pd}$ has lower energy than that of the E_F of TiO_2 leading to a reduction in the degree of band bending (Figure 5.12b).

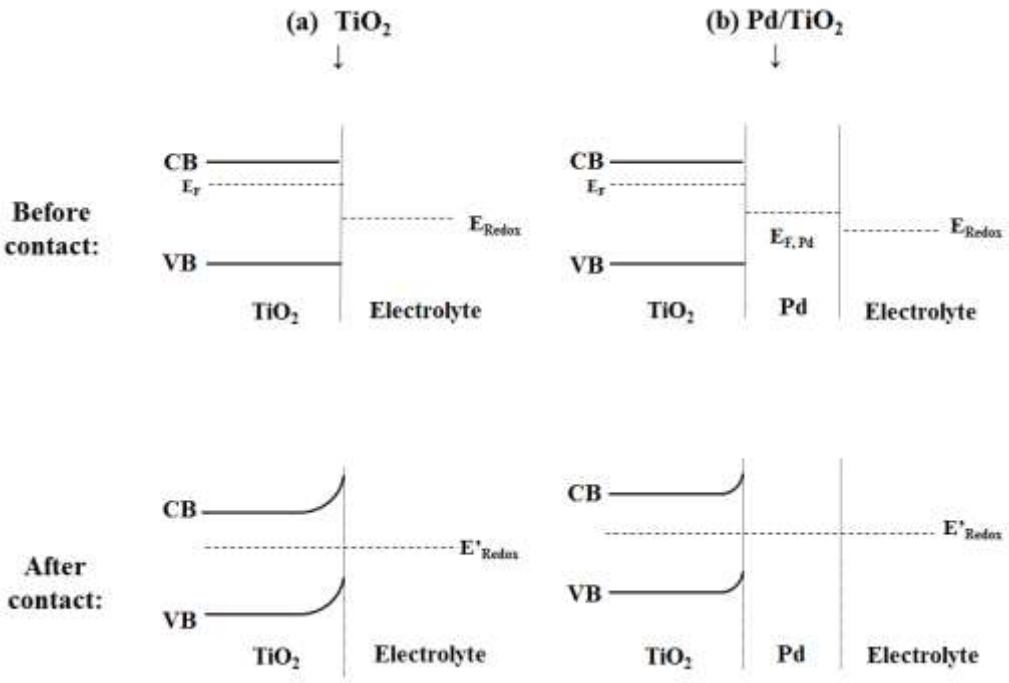

Figure 5.12 Schematic representation of energy band levels of (a) TiO_2 and (b) Pd/TiO_2 with the electrolyte before and after contact in the dark

Smaller band bending indicates a rapid charge transfer which results in an increase in charge carrier density.[164] The significant decrease in the slope of the Mott-Schottky curve of Pd/TiO_2 compared to bare TiO_2 already shows this increase in charge carrier density.[165]

The carrier density (N_D) of the samples can be further calculated using the following Equation 5.3:

$$N_D = \frac{2}{e\,\varepsilon_0\varepsilon}\left(\frac{dE}{d\left(\frac{1}{C^2}\right)}\right) \qquad \text{Eqn (5.3)}$$

where e = 1.6 x 10^{-19}C, ε_0 is the permittivity of vacuum (=8.86x10^{-12} F/m), ε is the relative permittivity of the semiconductor (=86 for rutile TiO_2).[166] $dE/d(1/C^2)$ values were determined from the Mott-Schottky plots.

Table 5.1 shows the calculated N_D values of TiO_2 and Pd/TiO_2. The carrier density of Pd/TiO_2 is one order magnitude bigger than TiO_2.

Table 5.1 Calculated carrier density of TiO_2 and Pd/TiO_2 under dark

Sample	Carrier Density (cm^{-3})
TiO_2	$0.15x10^{19}$
Pd/TiO_2	$1.36x10^{19}$

5.3.2. Electrochemical Impedance Spectroscopy (EIS)

Electrochemical impedance spectroscopy (EIS) measurements were performed in order to understand the charge transfer kinetics occurring at the interface. The rapid charge transfer at Pd/TiO_2 sample was confirmed by the higher N_D values calculated from the Mott-Schottky plots. EIS measurements further investigate the resistance against the interfacial charge transfer between the electrolyte and the semiconductor. Impedance data for TiO_2 and Pd/TiO_2 was represented by a Nyquist plot that shows the resistance over a frequency range. Figure 5.13 shows the Nyquist plots for TiO_2 and Pd/TiO_2 samples under dark and light conditions with a frequency range from 1MHz to 1Hz. The arc size of the Pd/TiO_2 sample is smaller compared to bare TiO_2. A smaller arc size in Nyquist plots indicates a lower resistance against the charge transfer at the interface.[167] The decreased resistance by Pd/TiO_2 sample is due to facilitated charge transfer at the interface by the smaller band bending and the electron trapping role of Pd nanoparticles.[168]

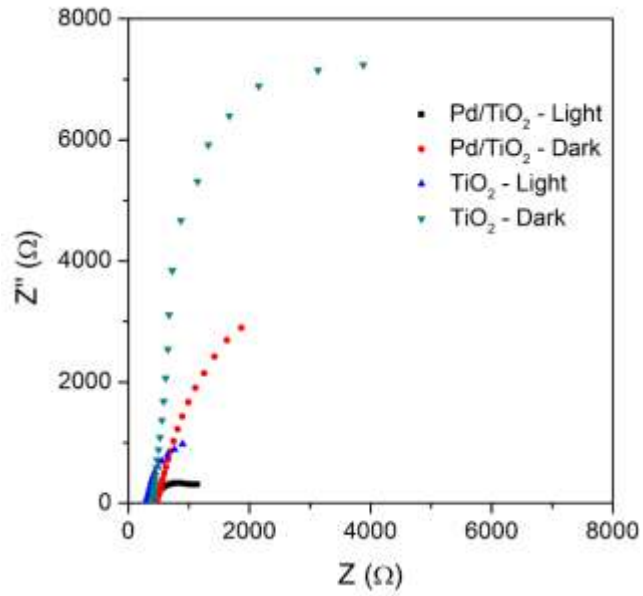

Figure 5.13 EIS analysis: Nyquist plots of TiO_2 andPd/TiO_2 for under dark and light conditions

The Nyquist plots were represented in the equivalent circuit where R_s is resistance of the solution, C_d is the capacitance and R_c is the resistance at the double layer formed at the interface (Figure 5.14):

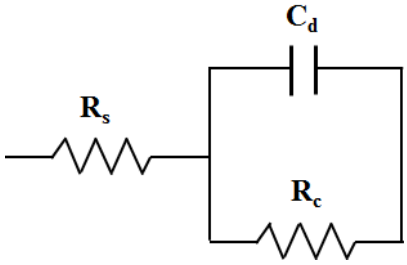

Figure 5.14 Equivalent circuit fitting for EIS data

Corresponding resistance and capacitance values were calculated by the software Z View. The values for TiO_2 and Pd/TiO_2 under illumination are summarised in Table 5.2 where the decrease in the resistance and capacitance in the hybrid Pd/TiO_2 catalyst system can be seen.

Table 5.2 Calculated Rs, C_d, and R_c values for TiO_2 and Pd/TiO_2 under illumination

	Rs (Ω)	C_d (μF)	Rc (Ω)
TiO_2	210	80	1303
Pd/TiO_2	403	32	628

5.3.3 j-V curves

The effect of annealing on the photocurrent has been investigated. PEC responses of as-grown and annealed TiO_2 nanorods on FTO are shown in Figure 5.15, whereby it can be seen that the photocurrent was immensely improved by annealing. This improvement in photocurrent can be seen more clearly from the j-v curves when the illumination was interrupted by a mechanic light chopper (Figure 5.16). Heat treatment enhances the crystallinity of the sample, which was confirmed by the intense crystalline peaks observed via the XRD pattern of annealed TiO_2 as in Figure 5.4. Annealing improves the anisotropy of the material, which facilitates charge transport across the nanorods to the FTO substrates. The crystal defects in as-grown TiO_2 nanorods, which can act as recombination centres for electron and holes, are reduced by annealing. These delays in recombination leads to an increased availability of photoexcited charge carriers, hence, an increase in photocurrent.

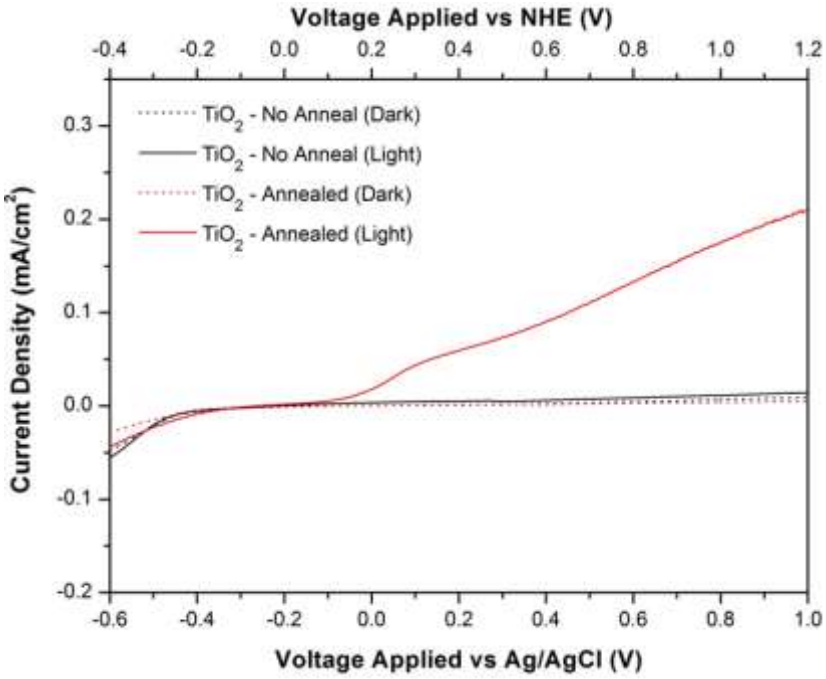

Figure 5.15 j-v curves for as-grown and annealed TiO_2 nanorods hydrothermally grown on FTO coated substrates under dark and light with a scan rate of 10mV/s in 0.01M Na_2SO_4 solution

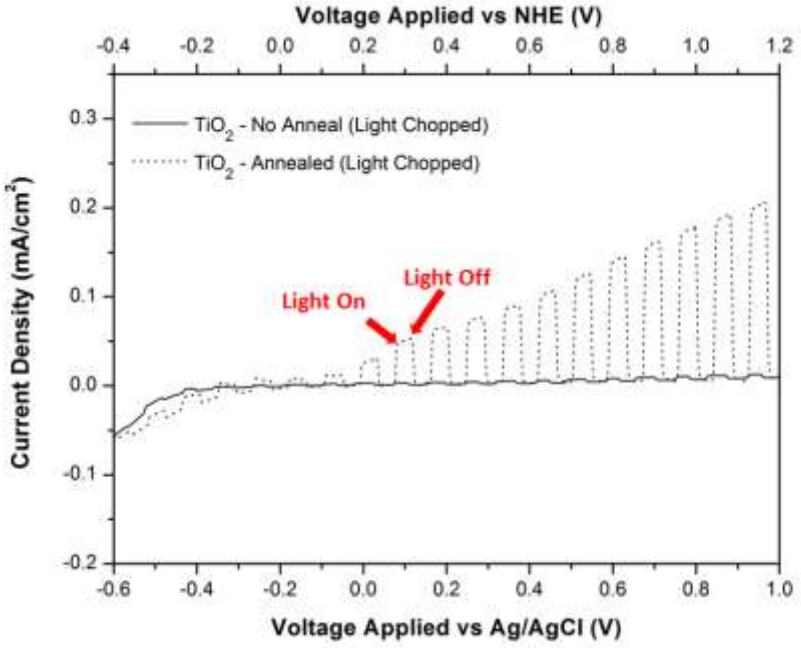

Figure 5.16 j-v curves for as-grown and annealed TiO_2 nanorods hydrothermally grown on FTO coated substrates under interrupted illumination with a mechanical light chopper. Scan rate was 10mV/s and an electrolyte of 0.01M Na_2SO_4 solution was used

The increase in crystallinity of TiO_2 nanorods grown on FTO coated glass was more significant compared to the TiO_2 nanorods synthesised on glass fibres substrates after the heat treatment. This difference is ascribed to the crystallinity of the substrates. The degree of crystallisation during the heat treatment is affected by the crystal structure of the substrates. The lattice match between the substrate and the nanorods is important. Glass fibres have an amorphous structure whereas FTO (SnO_2) is semicrystalline. The diffusion of atoms and hence the crystallisation take longer with amorphous substrates due to different surface energies between the substrate and nanorods. Therefore, heat treatment improves the crystallinity of TiO_2 grown on the FTO susbtrate considerably in contrast to TiO_2 on glass fibre substrates.

After confirming this significant influence of annealing, following PEC studies, including photoelectrocatalytic dye degradation and water splitting, were done with annealed TiO_2 samples only.

The effect of Pd nanoparticles on TiO_2's photoelectrochemical performance has been studied. PEC responses for TiO_2 and Pd/TiO_2 are shown in Figure 5.17. The dark currents of both samples were insignificant. All films showed photoanodic performance giving current at positive voltages under illumination. Pd/TiO_2 samples yield a higher photocurrent after 0V vs Ag/AgCl. The onset potential shifted toward more negative voltages at Pd/TiO_2 resulting in enhanced anodic photocurrents. The negative shift in onset potential of Pd/TiO_2 also indicates reduced overpotential losses. This can be ascribed to decreased band bending induced by Pd as discussed with the Mott-Schottky plots and EIS measurements. Figure 5.18 shows the J-V curves of the films where the illumination was interrupted by a mechanical light chopper. The photoresponse of all samples starts at negative voltages (-0.7V vs Ag/AgCl) which match with the flat band potential values.

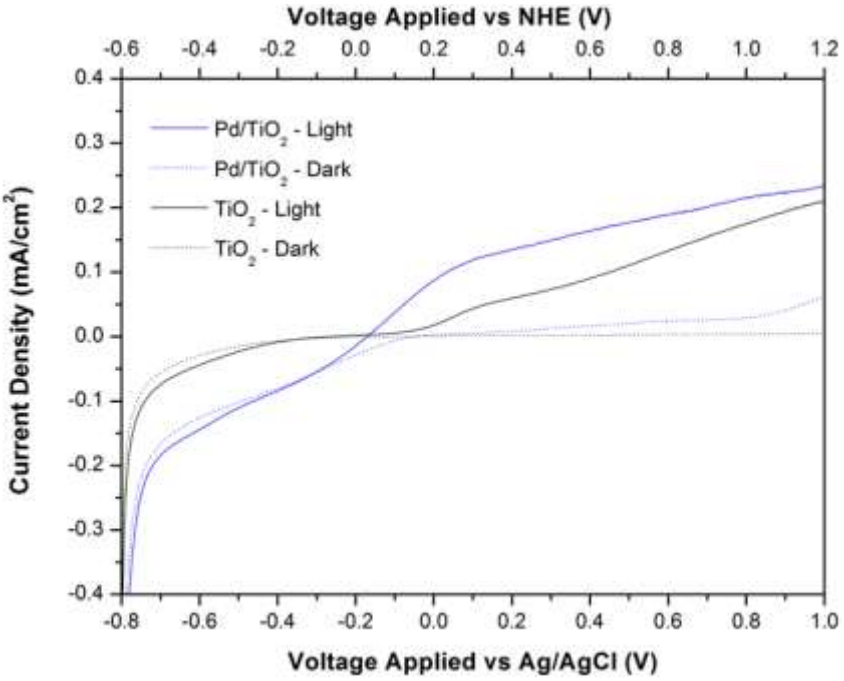

Figure 5.17 j-v curves for TiO_2 and Pd/TiO_2 hydrothermally grown on FTO coated substrates under dark and light with a scan rate of 10mV/s in 0.01M Na_2SO_4 solution

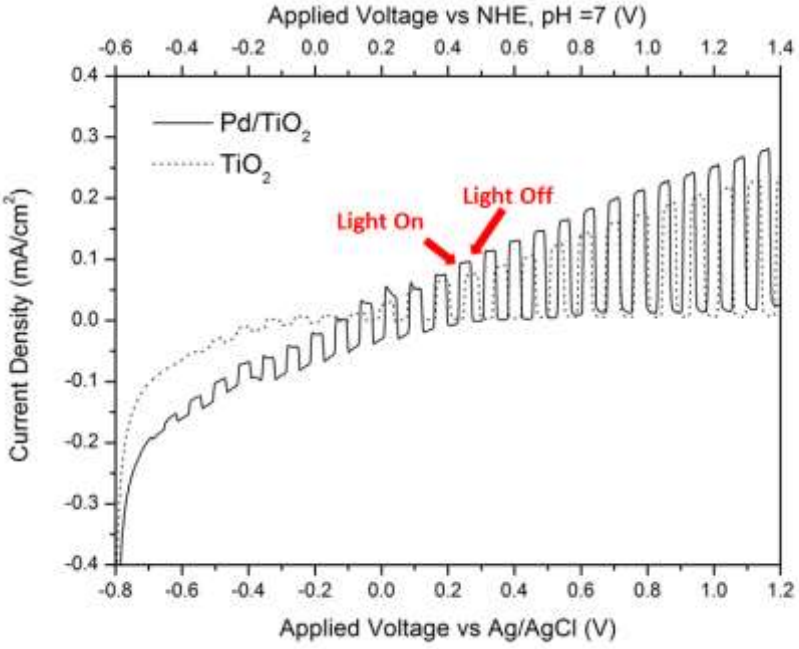

Figure 5.18 j-v curves for of TiO_2 and Pd/TiO_2 under interrupted illumination with a mechanical light chopper

Figure 5.19 shows the j-v curves of Pd/TiO_2 sample measured with different optical filters under interrupted illumination to show the PEC response in UV and visible light range. It can be observed that a photoresponse is obtained in both the UV and visible ranges of solar spectrum.

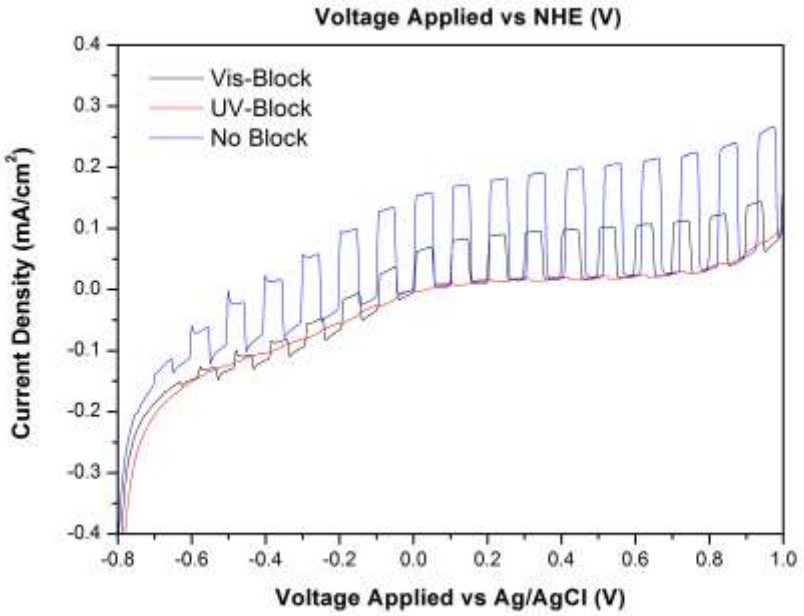

Figure 5.19 j-v curves for of Pd/TiO_2 with optical filtres under interrupted illumination. $\lambda_{UV\ block}$ > 400nm; $\lambda_{Vis\ Block}$ <400nm.

Since the optical response of TiO_2 is limited to UV range, the photocurrent obtained by the sample in the visible light range can be attributed to the plasmonic interaction of Pd nanoparticles with visible light. The free electrons of Pd are oscillated by the visible light are transferred to the conduction band of TiO_2 and then to the counter electrode through the outer circuit.

However, a significant amount of the photocurrent is formed by the electrons that are generated by UV light. This shows that TiO_2 is the dominant part of the hybrid photocatalyst Pd/TiO_2 in charge carrier generation. Considering the low amount of

Pd nanoparticles loaded onto TiO_2 nanorods, which is only 0.01M and, this dominance was anticipated.

5.4. Photoelectrocatalysis of Rhodamine B

The photoelectrocatalytic performance of the bare TiO_2 and hybrid Pd/TiO_2 catalyst systems was firstly studied through the photodecolourisation of RhB. The photocatalysts were fixed in a PEC cell with 2 ml of aqueous RhB dye solution (10ppm). The illumination area was 0.125 cm^2. The system was kept under dark for 30 minutes to provide the adsorption equilibrium before illumination under solar simulator. Voltages applied were 0V, 0.5V and 1V versus the reference electrode of Ag/AgCl. Only one dye solution sample per experiment was analysed by UV-Vis Spectroscopy as the solution volume is small (2ml). Therefore, the degree of degradation was reported as a percentage instead of displaying a full decolourisation profile as a function of time. The results of RhB degradation by TiO_2 and Pd/TiO_2 samples in different solutions at different applied voltages are summarised in Table 5.3.

Table 5.3 The percentage of RhB (10ppm) decolourisation by photoelectrocatalysis with TiO_2 and Pd/TiO_2 at different voltages

Voltage Applied vs Ag/AgCl	Time	Decolourisation TiO_2	Decolourisation Pd/TiO_2
1V	2h	22.5%	32%
0.5V	2h	17.1%	24.2%
0V	2h	13.6%	14.1%

The low degree of decolourisation in all samples is due to the small value of area of illumination (only 0.125 cm^2) in 2 ml of dye solution. The photoelectrocatalytic activities of all samples increased with increasing voltage. This enhancement is ascribed to the increased availability of charge carriers as recombination is surpassed by the external electric field. The hybrid catalyst Pd/TiO_2 showed a higher photoelectrocatalytic activity in aqueous RhB solution compared to bare TiO_2 at all voltages. The i-t curves during decolourisation confirmed that a higher photocurrent resulted in higher degree of photodecolourisation (Figure 5.20).

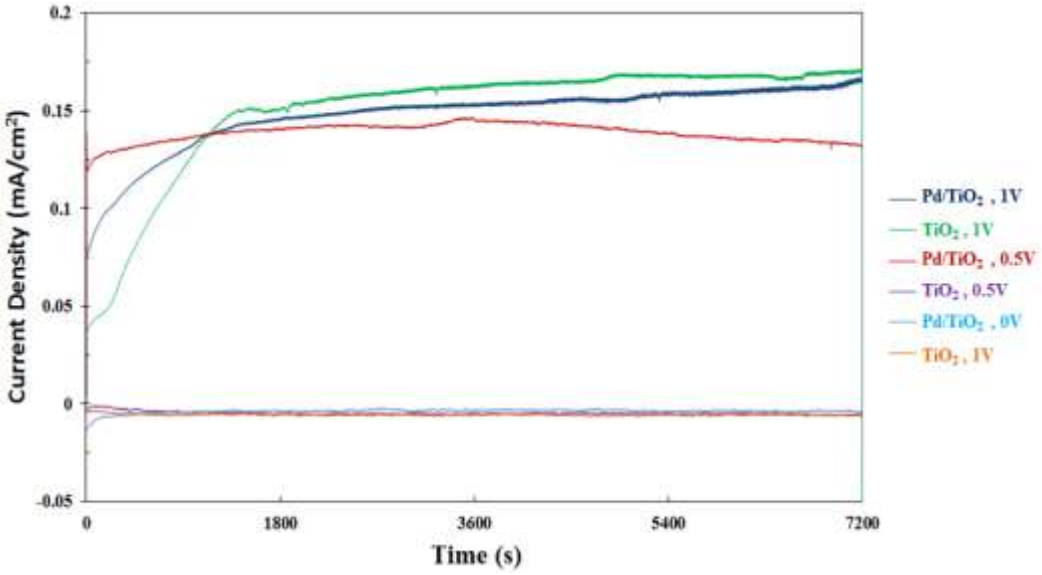

Figure 5.20 i-t curves during photoelectrocatalysis of RhB with TiO_2 and Pd/TiO2 under a variety of applied voltages vs Ag/AgCl

The redox reactions that occur in photoelectrocatalytic degradation of RhB can be summarised as below in Equation 5.4-5.8 and the proposed mechanism for the photoelectrochemistry is shown in Figure 5.21. The separated electrons and holes drive the redox reactions with the aqueous solution whereby holes oxidise water and hydroxyl ions to form hydroxyl radicals ($OH^{\cdot}$); and electrons reduce the oxygen to form superoxide radical anions ($O_2^{\cdot-}$). The degradation of the dye molecules occurs

due to the attack by these radical ions. The hybrid catalyst system Pd/TiO_2 showed superior performance compared to bare TiO_2 at all voltages. Therefore it can be suggested that the electrons scavenged by Pd nanoparticles contributes to the dye degradation by reducing the aqueous solution to form superradical ions ($O_2^{\cdot-}$) that subsequently degrade the dye molecules (Eqn 5.7).

$$h^+ (TiO_2) + H_2O \rightarrow OH^{\cdot} \tag{5.4}$$

$$2e^-(TiO_2) + O_2 \rightarrow O_2^{\cdot-} \tag{5.5}$$

$$2e^-(Pt\ counter\ electrode) + O_2 \rightarrow O_2^{\cdot-} \tag{5.6}$$

$$2e^-(Pd) + O_2 \rightarrow O_2^{\cdot-} \tag{5.7}$$

$$O_2^{\cdot-} + OH^{\cdot} + RhB\ Dye \rightarrow Degrdation\ products \tag{5.8}$$

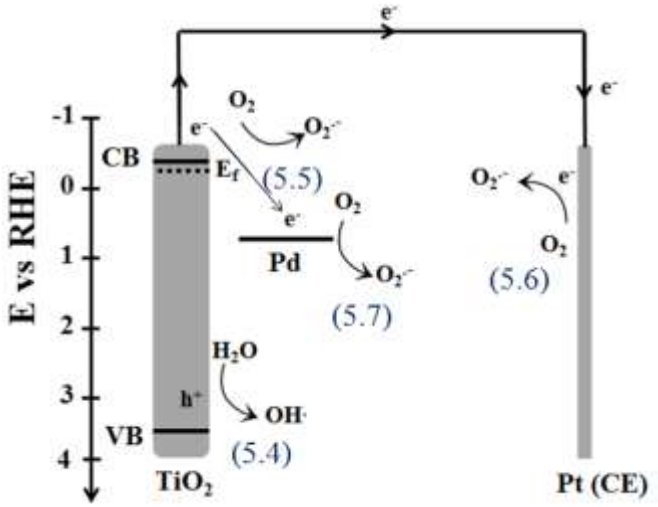

Figure 5.21 Proposed charge transfer mechanism for the photoelectrocatalysis of Rhodamine B with Pd/TiO_2 sample

5.5. Solar Hydrogen Production

The prepared bare TiO_2 and hybrid Pd/TiO_2 catalyst systems were then tested for their ability to produce hydrogen using solar simulator. The experiments were conducted in three different solutions; namely, 0.01M Na_2SO_4 aqueous solution, pure deionised water and methanol solution (methanol:deionised water with 1:4 ratio). The photogenerated hydrogen evolution profiles as a function of time was obtained at the different voltages applied versus NHE: 0V, 0.7V and 1.2V. The solar hydrogen production processes with pure deionised water were conducted in a one chamber photoelectrochemical cell (Series 948307) where both the catalyst and counter electrode were placed in the same single chamber due to the low ionic conductivity of the deionised water. The experiments with 0.01M Na_2SO_4 and methanol solution were conducted in a two chamber photoelectrochemical cell (Series 946621) where the catalyst and the counter electrode were placed in two separate chambers. Solar hydrogen production was measured from both of the chambers. The hydrogen profiles were given as the sum of the hydrogen produced in each chamber. Gas samples were taken manually with a syringe every 15 minutes for the first hour of the experiment. They were then taken at in 1 hour intervals for the GC analysis.

Figure 5.22 shows the hydrogen evolution profiles for the system with 0.01M Na_2SO_4 solution used as sacrificial agent. Hydrogen was not produced unless an external bias was applied to the system. For the systems under external bias of 0.7V and 1.2V vs NHE, the catalyst conditioning prolonged 30 minutes and the evolution of photogenerated hydrogen started after 30 minutes showing in a linear increase in the total amount of hydrogen produced. Highest amount of hydrogen was obtained with the TiO_2 sample reaching to a total 612µmol of H_2 in 5 hours (122.5µmol/h) (η_F = 44.7%) at an external bias of 1.2V vs NHE. This value was 197µmol for Pd/TiO_2

(39.4 µmol/h) (η_F = 42.2.0%) under the same conditions. An example of the i-t curve during hydrogen production is shown in Figure 5.23. These i-t curves belong to TiO_2 and Pd/TiO_2 in 0.01M Na_2SO_4 at an applied voltage of 1.2V and shows that the photocurrent of TiO_2 is higher than that of Pd/TiO_2.

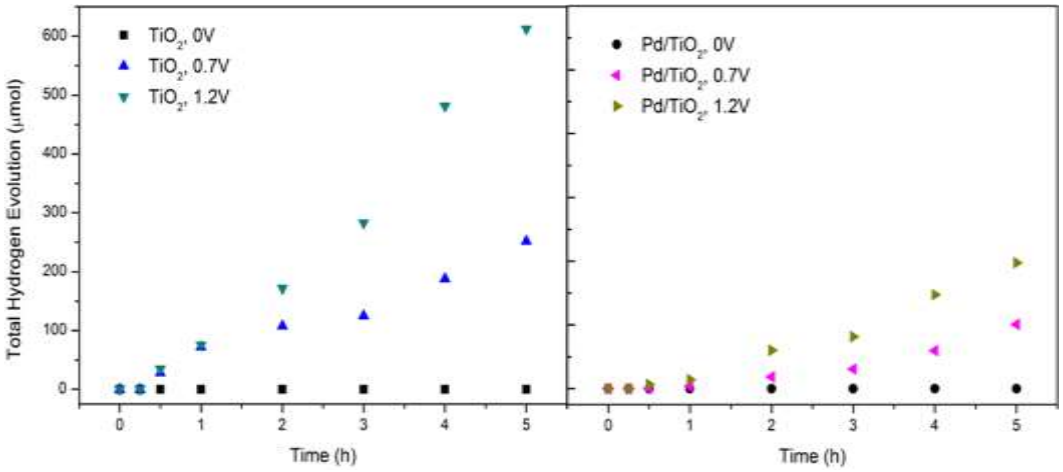

Figure 5.22 Hydrogen evolution profiles of TiO_2 and Pd/TiO_2 as a function of time at different voltages time in 0.01M Na_2SO_4

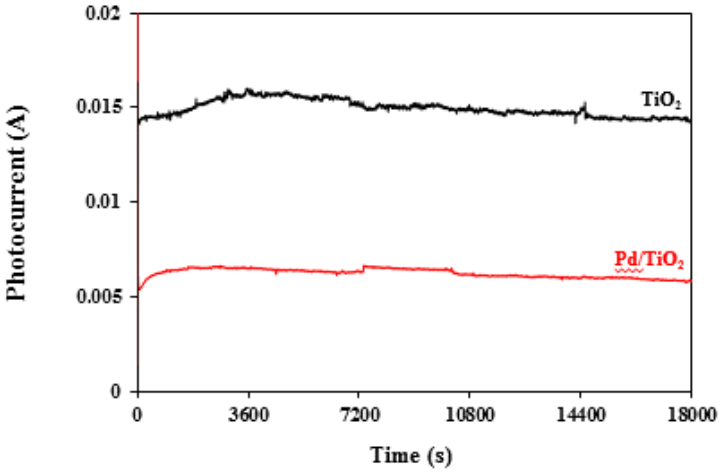

Figure 5.23 i-t curves during solar hydrogen production in 0.01M Na_2SO_4 at V_{app} = 1.2V with TiO_2 and Pd/TiO_2

Figure 5.24 shows the hydrogen evolution profiles of bare TiO_2 and Pd/TiO_2 when the experiment was conducted with deionised water. Hydrogen was again produced

only under an applied voltage. Here, the catalyst conditioning took longer; the experiments thereby were carried out for longer times. The amount of photogenerated hydrogen was again higher for the TiO_2 samples (16.7µmol) (η_F = 11.1%) compared to Pd/TiO_2 (12.4µmol) (η_F = 16.6%) in 8 hours at an applied voltage of 1.2V vs NHE (pH = 7) in deionised water. The i-t curve during water splitting in deionized water at V_{app} = 0.7V shows that TiO_2 has a higher photocurrent that Pd/TiO_2 (Figure 5.25). The amount of hydrogen produced by TiO_2 at 0.7V and 1.2V were very close which could be ascribed to the saturated photocurrent of TiO_2 after a certain value of applied voltage. Hydrogen production by Pd/TiO_2 however increased with the increasing potential which in turn promoted the efficient separation of electrons and holes, hence, a higher photocurrent.

-

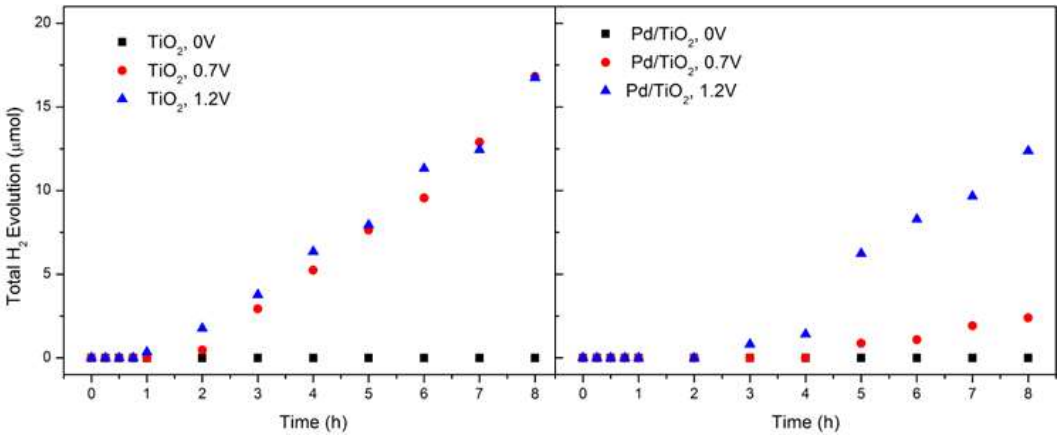

Figure 5.24 Hydrogen evolution profiles of TiO_2 and Pd/TiO_2 as a function of time at different voltages time in deionized water

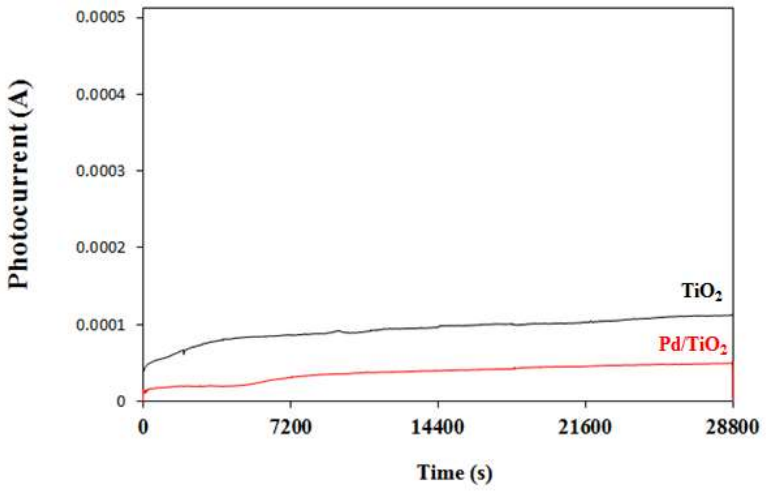

Figure 5.25 i-t curves during solar hydrogen production in deionized water at V_{app} = 0.7V with TiO_2 and Pd/TiO_2

Figure 5.26 shows the solar hydrogen production as a function of time from methanol solution (1:4, methanol:deionised water) with bare TiO_2 and Pd/TiO_2 at different voltages. The catalyst conditioning took more than 4 hours for TiO_2 whereas it was only 2 hours for Pd/TiO_2. In contrast to previous systems, it was the hybrid catalyst Pd/TiO_2 system that have the superior photoelectrocatalytic activity in methanol solution i-t curve during methanol reforming in methanol solution at V_{app} = 1.2V again confirmed that higher photocurrent resulted in higher hydrogen production (Figure 5.27). The amount of photogenerated hydrogen with Pd/TiO_2 was 25.7µmol (η_F = 34.4%) at an applied voltage of 1.2V vs NHE (pH = 7) compared to TiO_2 which was only 3.2µmol in 8 hours (η_F = 5.4%) under same conditions.

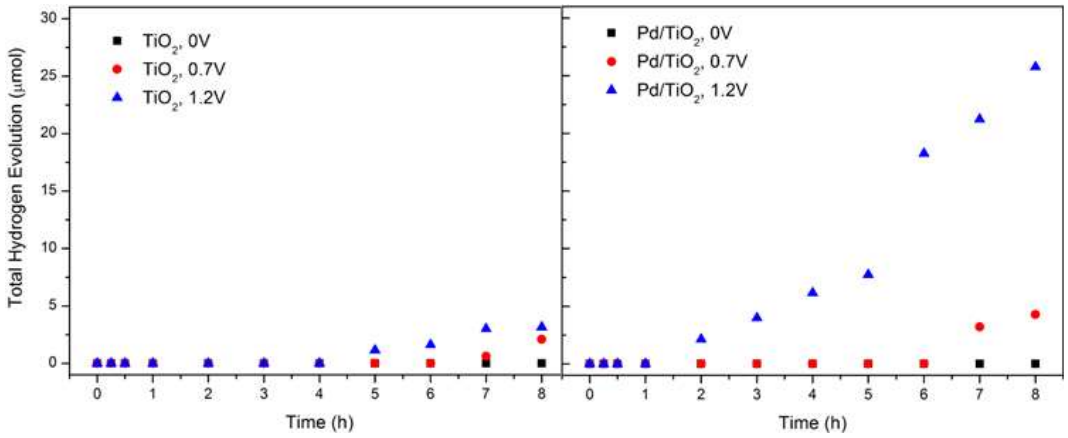

Figure 5.26 Hydrogen evolution profiles of TiO_2 and Pd/TiO_2 as a function of time at different voltages time in 1:4 methanol:deionized water

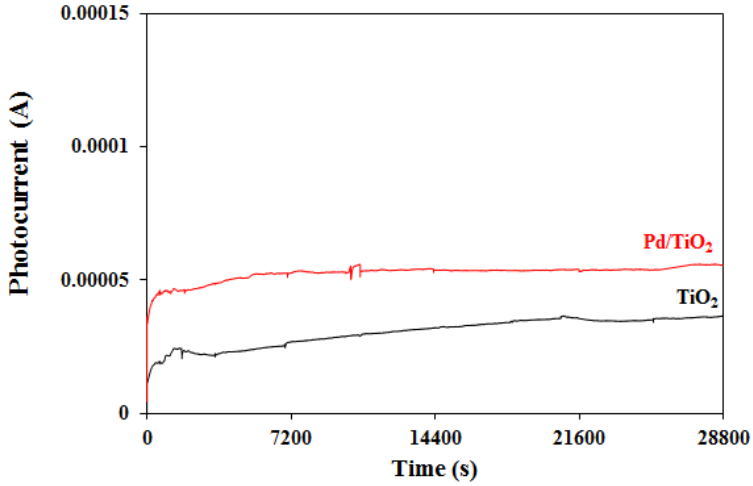

Figure 5.27 i-t curves during methanol reforming in 1:4 methanol deionized water at V_{app} = 1.2V with TiO_2 and Pd/TiO_2

Two prominent observations can be made from these results. Firstly, hydrogen evolution is significantly higher when the system is in Na_2SO_4 solution. This is related to the higher ionic conductivity of the solution compared to methanol and deionised water solution which enables a more efficient transfer of ions between the electrodes. Secondly, TiO_2 showed a better photoreactivity in 0.01M Na_2SO_4 electrolyte solution and deionised water whereas Pd/TiO_2 produced more hydrogen in methanol solutions. The mechanism of photoelectrochemistry, which can be

summarised as a combination of the transfer of photogenerated charges and the redox reactions occurring at the surfaces, should be investigated to understand the results.

When photons are absorbed by TiO_2 and the electrons are excited to the conduction band of TiO_2 holes are left in the valence band. A certain amount of these photogenerated electrons are transferred to Pd nanoparticles which inhibits electrons to move to FTO substrate and then to Pt counter electrode. This implies an efficient charge separation; however, it also represents a decrease in the photocurrent detected by the potentiostat in photoelectrochemical measurements. The localised plasmon resonance effect by Pd nanoparticles should also be discussed in this respect. It is expected that excessive oscillations of the electrons of Pd by the surrounding electric field will create an enhancement in charge generation. If the photoexcited electrons have energy higher than that of the conduction band of TiO_2, they are then directly transferred to the conduction band and then to the counter electrode, which represent an increase the photocurrent and solar hydrogen production at the counter electrode. However, the contribution of plasmonic interaction is not significant as discussed with the j-V curves under UV block in Figure 5.19.

With increasing voltage resulting from the increased electric field between the electrodes, more electrons are transferred to the counter electrode. The availability of photogenerated holes that remain in the working electrode is therefore also enhanced. This explains the enhanced photoelectrocatalytic performance in both dye degradation and solar hydrogen production at higher voltages.

The key point in understanding the difference between photoelectrocatalytic performance of TiO_2 and Pd/TiO_2 lies in the fate of photoelectrons trapped by the Pd nanoparticles. The height of the Schottky barrier that is formed between the

semiconductor and metal, which is dependent on the work function of the metal, inclines whether the metal acts as an efficient electron scavenger. A higher work function indicates a higher Schottky barrier which implies more energy is required for electron transfer and also a higher probability for hole transfer to the metal. The work function of Pd (-5.2eV) lies in-between Ag (-4.7eV) and Pt (-6.3eV). Whether the trapped electrons by Pd undergo reduction chemistry with the solution on the surface prior to recombination with the holes determines the performance of the Pd/TiO_2 catalyst system. The redox reactions in solar hydrogen production by the catalyst system in 0.01M Na_2SO_4 solution and deionised water are as follows in Equation 5.9-5.12. The proposed mechanism for the charge transfer is shown in Figure 5.28.

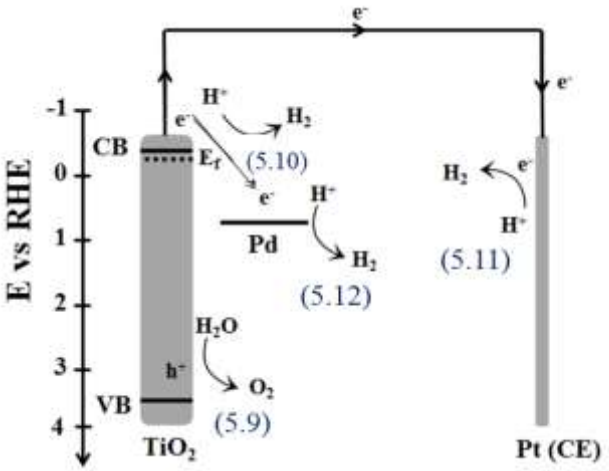

Figure 5.28 Proposed charge transfer mechanism with Pd/TiO_2 sample in 0.01M Na_2SO_4 and in deionised water for solar hydrogen production

$$H_2O + 2h^+ \rightarrow \frac{1}{2}O_2 + 2H^+ \quad (5.9)$$

$$2e^-(TiO_2) + 2H^+ \rightarrow H_2 \quad (5.10)$$

$$2e^{-}(Pt\ counter\ electrode) + 2H^{+} \rightarrow H_2 \quad (5.11)$$

$$2e^{-}(Pd) + 2H^{+} \rightarrow H_2 \quad (5.12)$$

The electrons that reach the counter electrode successfully reduce the hydrogen ions to hydrogen gas. Hydrogen ions are also reduced by the electrons that are in the conduction band of TiO_2 as hydrogen evolution was also detected in the PEC cell chamber where the TiO_2 sample was kept. However, it should be noted that the amount of H_2 produced was higher at the chamber of the counter electrode (Figure 5.29).

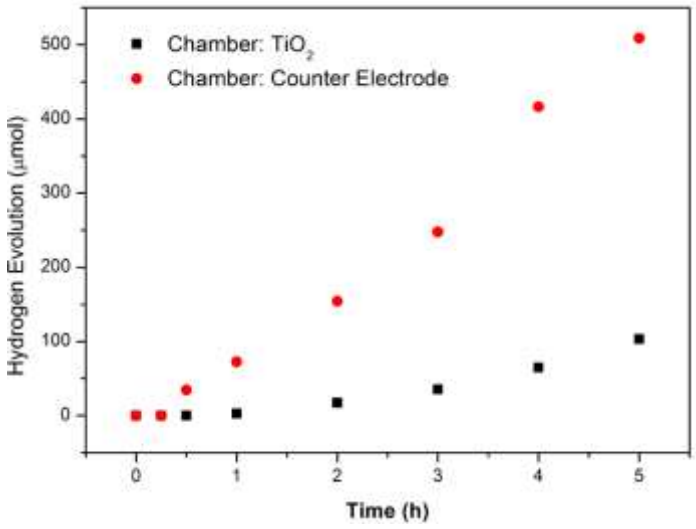

Figure 5.29 Solar hydrogen production by TiO_2 in two different chambers during solar hydrogen production in 0.01M Na_2SO_4 at V_{app} = 1.2v vs NHE

In the process of solar hydrogen production, the hybrid Pd/TiO_2 catalyst system failed to produce the amount of hydrogen that bare TiO_2 produced in deionised water and 0.01M Na_2SO_4. The electrons trapped by the Pd nanoparticles recombine with

the holes before they can reduce the hydrogen ions and contribute to total solar hydrogen production.

Hydrogen production in methanol reforming involves a different mechanism of photoelectrochemistry. The redox reactions that occur in solar hydrogen production from methanol solution are stated below in Equations 5.12-5.16. The proposed mechanism for the charge transfer is shown in Figure 5.30. The methanol solution is oxidised by holes to form CO_2 and H^+ whereby H^+ ions are reduced to evaluate hydrogen gas. The intermediate reactions involve the formation of CO and formaldehyde. O_2 production does not occur; therefore, this process is termed as methanol reforming instead of water splitting. The Pd/TiO_2 catalyst system produced more hydrogen compared to bare TiO_2 in methanol solution. This could be attributed to the excellent catalytic properties of metal co-catalysts when it comes to methanol reforming.[169,170] Methanol is an efficient hole scavenger compared to pure deionised water and Na_2SO_4 which reduces the possibility of photoelectrons trapped by the Pd nanoparticles to recombine with the holes.

$$CH_3OH + H_2O + 6h^+ \rightarrow CO_2 + 6H^+ \quad (5.13)$$

$$2e^-(TiO_2) + 2H^+ \rightarrow H_2 \quad (5.14)$$

$$e^-(Pt\ counter\ electrode) + H^+ \rightarrow H_2 \quad (5.15)$$

$$e^-(Pd) + H^+ \rightarrow H_2 \quad (5.16)$$

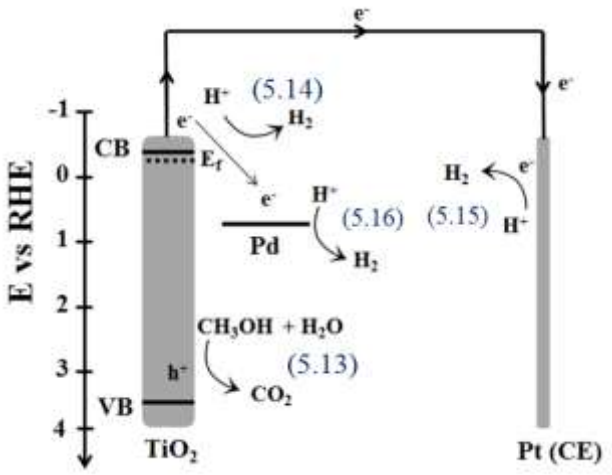

Figure 5.30 Proposed charge transfer mechanism with Pd/TiO_2 sample for solar hydrogen production with methanol reforming

5.6. Summary

A hybrid Pd/TiO_2 photocatalyst system was developed by depositing metallic Pd nanoparticles onto TiO_2 nanorods hydrothermally grown on FTO substrate. The existence of Pd was confirmed by characterisation methods such as TEM and XPS. The samples were photoelectrochemically characterised by electrochemical impedance spectroscopy and subsequently derived Mott-Schottky plots. There was a positive shift in flat band potential due to the relative position of Pd's to the Fermi level of TiO_2 which induced a reduction in overpotentials in Pd/TiO_2 samples. The facilitated electron transfer between Pd and TiO_2 was also confirmed by EIS data. The photoelectrochemical performance of the bare TiO_2 and hybrid Pd/TiO_2 samples were compared depending on their photoactivities on the decolourisation of a standard commercial textile dye Rhodamine B (RhB) and solar hydrogen production in different electrolyte solutions at various applied voltage values. Hybrid photocatalyst Pd/TiO_2 showed enhanced photoelectrocatalytic activity in decolourisation RhB in aqueous solution. A higher amount of hydrogen was

photogenerated in methanol solution by Pd/TiO_2. However, bare TiO_2 samples produced a higher amount of hydrogen in 0.01M Na_2SO_4 and pure deionised water under the same conditions. The hole scavenging role of methanol is crucial here as electrons successfully trapped by the Pd nanoparticles can contribute to hydrogen reduction before recombination. The results were explained by possible mechanisms of photoelectrochemistry proposed for both dye degradation and solar hydrogen production.

CHAPTER 6: Ag MODIFICATION OF BiFeO3 THIN FILMS FOR THE ENHANCEMENT OF PHOTOCATHODE PERFORMANCE UNDER VISIBLE LIGHT

IOP Publishing Nanotechnology
Nanotechnology 27 (2016) 345402 (8pp) doi:10.1088/0957-4484/27/34/345402

Perovskite $BiFeO_3$ thin film photocathode performance with visible light activity

P Yilmaz[1], D Yeo[2], H Chang[2], L Loh[2] and S Dunn[1]

[1] School of Engineering and Materials Science, Queen Mary University of London, Mile End Road, London E1 4NS, UK
[2] School of Engineering, Nanyang Polytechnic, Singapore 569830, Singapore

E-mail: s.e.dunn@qmul.ac.uk

Received 4 April 2016, revised 24 May 2016
Accepted for publication 22 June 2016
Published 15 July 2016

Abstract

Perovskite materials are now an important class of materials in the application areas of photovoltaics and photocatalysis. Inorganic perovskites such as $BiFeO_3$ (BFO) are promising photocatalyst materials with visible light activity and inherent stability. Here we report the large area sol-gel synthesis of BFO films for solar stimulated water photo oxidation. By modifying the sol-gel synthesis process we have produced a perovskite material that has p-type behaviour and a flat band potential of ~1.15 V (versus NHE). The photocathode produces a density of $-0.004\,mA\,cm^{-2}$ at 0 V versus NHE under AM1.5G illumination. We further show that 0.6 $\mu mol\,h^{-1}$ of O_2 was produced at an external bias of −0.5 V versus Ag/AgCl. The addition of a non-percolating conducting network of Ag increases the photocurrent to $-0.07\,mA\,cm^{-2}$ at 0 V versus NHE (at 2% Ag loading) with an increase to 2.7 $\mu mol\,h^{-1}$ for O_2 production. We attribute the enhancement in photoelectrochemical performance to increased light absorption due light scattering by the incorporated Ag particles, improved charge transfer kinetics at the Ag/BFO interface and reduced over potential losses. We support these claims by an observed shift in flat band and onset potentials after Ag modification through UV–vis spectroscopy, Mott–Schottky plots and j–v curve analysis.

S Online supplementary data available from stacks.iop.org/NANO/27/345402/mmedia

Keywords: solar energy conversion, photocathode, photoelectrochemistry, perovskite thin film, photooxidation

(Some figures may appear in colour only in the online journal)

Introduction

The use of perovskite materials in photoactive devices and systems is increasingly well studied with concerns over the stability and process ability of systems such as MAPI ($CH_3NH_3PbI_3$) being of key interest [1]. Additionally, studies in the mid 2010s are indicating that some of the organo-halide perovskite systems may have a ferroelectric contribution due to the rotation of dipoles in the backbone of the system [2, 3]. There has been a historical interest in the photophysics and photochemistry of inorganic ferroelectric materials, many of which share the perovskite crystal structure. Such interest in ferroelectric materials as a photocatalysts stem from the inherent materials properties associated with carrier separation and chemical stability under illumination in aqueous environments [4, 5]. The charge separation is a result of the electric field formed by the internal spontaneous polarisation within ferroelectric domains. The spontaneous polarisation drives electrons and holes accumulate at opposite surfaces where band bending occurs [6]. Efficient charge separation is induced by this inherent band bending and accumulated charges can react with adsorbed molecules at the surfaces [7]. Photocatalytic treatment of waste water and textile dyes has been reported with such material systems [8, 9].

Among inorganic perovskite materials, $BiFeO_3$ (BFO) is drawing attention due to its narrow optical band gap (E_g ~2.0–2.2 eV) [10] and corresponding optical response to

 © 2016 IOP Publishing Ltd Printed in the UK

6.1. Introduction

There is growing interest in ferroelectric materials for photocatalytic and photovoltaic applications due to their material properties associated with carrier separation and chemical stability under illumination in aqueous environments.[16,80] Among ferroelectric photocatalysts such as $BaTiO_3$ and $LiNbO_3$, $BiFeO_3$ (BFO) has received great attention as it harvest visible light due to its narrow band gap (2.0-2.2eV).[171] $BiFeO_3$ is an intriguing and complex material which has been extensively investigated for its structural, optical and electrical properties whereby a range of contradictory information has been reported in literature.[18] Its complexity comes from its varying band positions, indirect/direct band gap characteristics and type of n or p conductivity which immensely influence the resulting photoelectrochemical behaviour.[66,67,172,69]

This chapter focuses on the production of $BiFeO_3$ thin films on large area FTO coated glass by a simple sol-gel method for photo-oxidation of water. The $BiFeO_3$ thin films showed photocathode performance with p-type behaviour. This is in contrast to previous water splitting studies in literature, which have reported $BiFeO_3$ electrodes mostly as photoanodes.[173,174,175] The flat band potential was estimated to be 0.95V vs Ag/AgCl (1.15 vs NHE, pH = 7). A photocurrent density of -0.004mA/cm^2 was achieved by pure $BiFeO_3$ at 0V vs NHE under AM1.5 G illumination. This value is an order of two magnitudes smaller compared to native conventional semiconductors. To improve photocatalytic performance, pure $BiFeO_3$ samples were modified by incorporating Ag into the $BiFeO_3$ matrix. Ag was added in the form of metallic Ag particles and Ag NWs during the sol-gel preparation. SEM,

TEM, XPS and UV-Vis spectroscopy were used for the characterisation of the samples.

It was shown that at different concentrations of Ag there are clear trends to the photocurrent and corresponding amount of photogenerated O_2. The highest photocurrent was achieved using $BiFeO_3$ with 2molar% Ag particles and $BiFeO_3$ with 0.1vol% Ag NWs with photocurrents of -0.07mA/cm^2 and -0.05mA/cm^2, respectively. The significant increase in photoelectrochemical performance was attributed to reduced overpotential losses and efficient charge separation by Ag particles which act as an electron sink and surpass their recombination with holes. These explanations are supported by detailed mesurements of Mott-Schottky plots and j-v curves with shifts in the flat band and onset potentials after Ag modification. The photoelectrochemical improvements were achieved without any significant change on the morphological structure and p-type behaviour of the pure $BiFeO_3$ samples.

6.2 Materials Characterisation

The morphology of the $BiFeO_3$ thin films on FTO coated glass produced by sol-gel process were analysed using SEM imaging. SEM micrographs of the pure $BiFeO_3$ thin film, which is formed with of 1, 2 and 3 layers, are shown in Figure 6.1. The SEM micrographs show uniform thin films that consist of small particulates of $BiFeO_3$. The deposition is not densely packed as there are voids in between the particulates for all the samples. In particular, 1-layer $BiFeO_3$ does not cover the whole FTO substrate and particles of FTO can be clearly seen. In comparison, thin films of 2-layer $BiFeO_3$ and 3-layer $BiFeO_3$ are more densely packed.

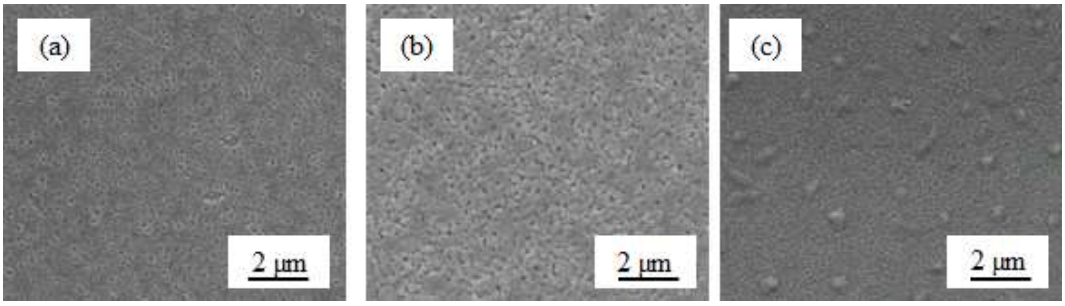

Figure 6.1 SEM micrographs of pure $BiFeO_3$ thin films deposited on FTO substrates as (a) 1-layer, (b) 2-layer and (c) 3-layer. The FTO substrate can be seen clearly in 1-layer thin film whereas 2 and 3 layer thin films were denser

The SEM micrographs for the cross-sections of the samples are shown in Figure 6.2. The film thickness was measured to be 390nm, 410nm, and 440nm for 1-layer $BiFeO_3$, 2-layer $BiFeO_3$ and 3-layer $BiFeO_3$ thin films, respectively. The deposition of subsequent layers did not double or triple the thickness of the films. The TEM micrograph of 2-layer $BiFeO_3$ can confirm this as the deposited subsequent layer is thinner than the adjacent layer (Figure 6.2d).

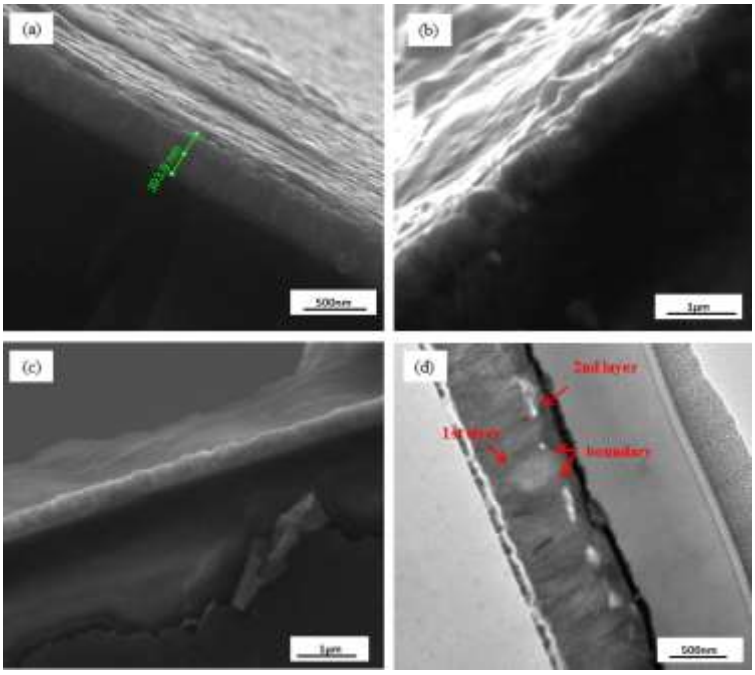

Figure 6.2 SEM micrographs for the cross-section of pure $BiFeO_3$ thin as (a) 1-layer, (b) 2-layer and (c) 3-layer. The film thickness was measured to be 380nm, 410nm, and 440nm for a, b and c. (d) TEM micrograph of 2-layer $BiFeO_3$ which clearly the shows the thickness of the 2nd layer deposited is smaller compared to the thickness of the 1st layer deposited on FTO substrate

This could be related to the wettability of $BiFeO_3$ sol dripped on the sample before spin coating. It was observed that the $BiFeO_3$ sol completely wets the FTO substrate compared to the surface of 1-Layer $BiFeO_3$ thin film (Figure 6.3). The contact angle measurements could not be done as the angles were too small to detect. The inferior wettability could lead to production of a thinner subsequent layer in 2-layer $BiFeO_3$ and 3-layer $BiFeO_3$ thin films compared to 1-layer $BiFeO_3$.

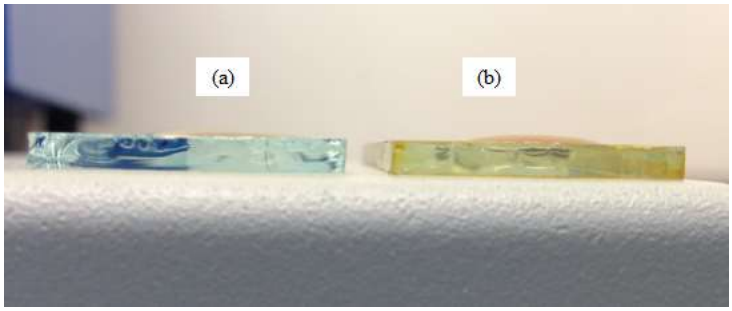

Figure 6.3 Images of $BiFeO_3$ sol dipped on the (a) FTO coated glass and (b) 1-layer BiFeO3 thin film deposited on FTO coated glass

The photocurrents of $BiFeO_3$ thin films with different layers under dark and light have been investigated. The results will be discussed in details in the next section. Highest photocurrent was observed for the 2-layer $BiFeO_3$ thin film deposited on FTO coated glass. Therefore, further studies using Ag modification and subsequent characterisation along with experiments for photo-oxidation of water have been done using 2-layer $BiFeO_3$ thin films. The term "pure $BiFeO_3$" will now be used in the following discussions to refer to 2-layer $BiFeO_3$ thin films.

Figure 6.4 shows the SEM micrographs of $BiFeO_3$ thin films incorporated with Ag at different concentrations. Ag modification did not have any significant effect on the morphological structure. In fact, metallic Ag particles and Ag nanowires were not observed under SEM imaging and EDX during SEM analysis. This is because the the amount of Ag incorporated was below the detection threshold of EDX.

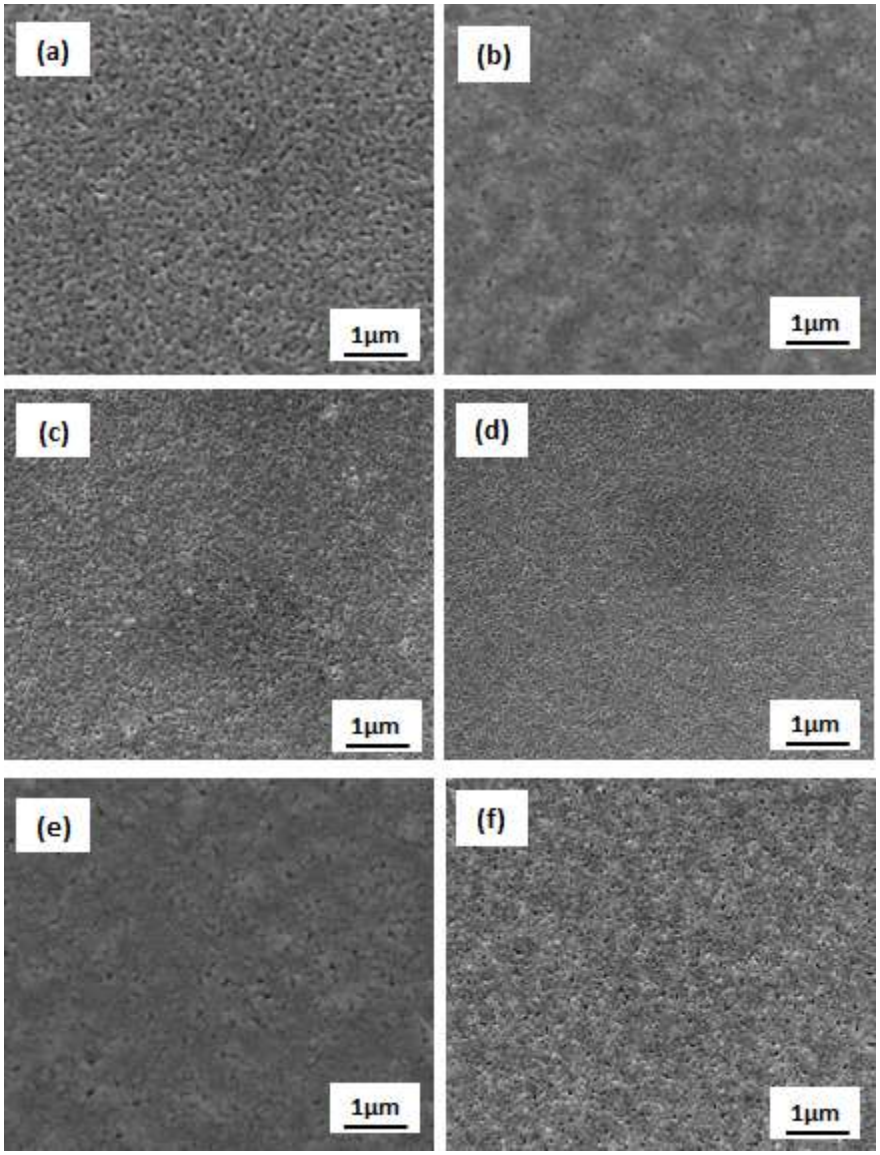

Figure 6.4 SEM micrographs for $BiFeO_3$ thin films with (a) 0.5molar% Ag particles, (b) 2molar% Ag particles, (c) 0.01vol%Ag NWs, (d) 0.06vol%Ag NWs, (e) 0.1vol% Ag NWs and (f) 0.2vol%Ag NWs. Ag modification did not have any significant effect on the morphological structure

The phase compositions of the samples were analysed using XRD. Figure 6.5 shows the XRD patterns of pure $BiFeO_3$ and Ag modified $BiFeO_3$ at different Ag concentrations. All crystalline peaks were indexed to perovskite $BiFeO_3$ except for an impurity peak for Bi_2O_3 which was observed at $2\theta = 54.7$. The other peaks can be ascribed to the FTO substrate. Ag was not detected under XRD analysis as its amount was below the detection threshold of XRD.

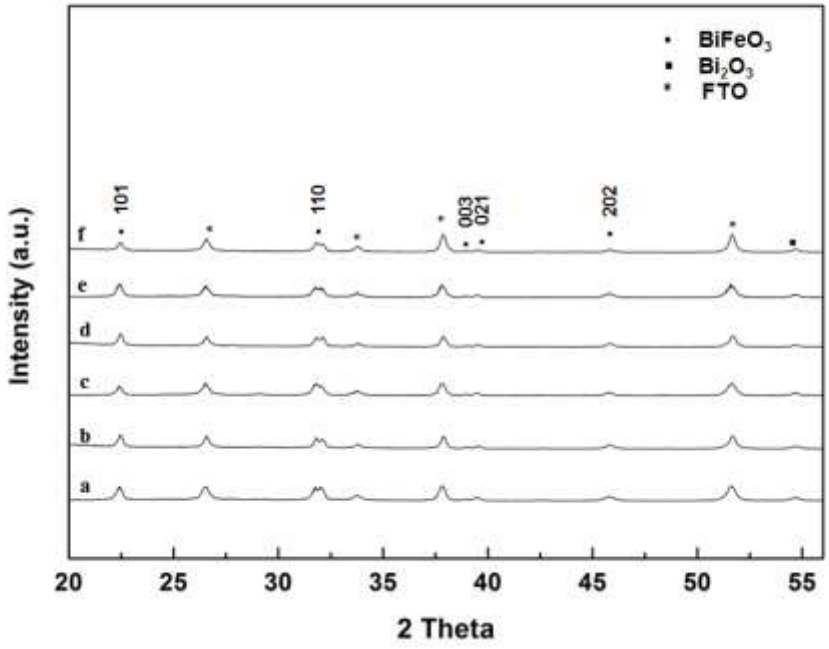

Figure 6.5 XRD pattern of (a) pure $BiFeO_3$ (b) $BiFeO_3$ with 0.5molar% Ag particles, (c) $BiFeO_3$ with 2molar% Ag particles, (d) $BiFeO_3$ with 0.01vol%Ag NWs, (e) $BiFeO_3$ with 0.1vol% Ag NWs and (f) $BiFeO_3$ with 0.2vol%Ag NWs. There was no observable change and no Ag peak was observed in XRD patterns of Ag modified $BiFeO_3$ thin films

There was no significant change observed in the XRD patterns after the incorporation of Ag. Minor differences were observed especially in the intensity of the (110) peak. These minor differences can be attributed to altered nucleation mechanisms in the thin film production during Ag modification.[176] However, there was no major shift in the doublet peak at (110) which denotes that Ag was not incorporated into the $BiFeO_3$ lattice but was instead present on the surface or grain boundaries (Figure 6.6).[92]

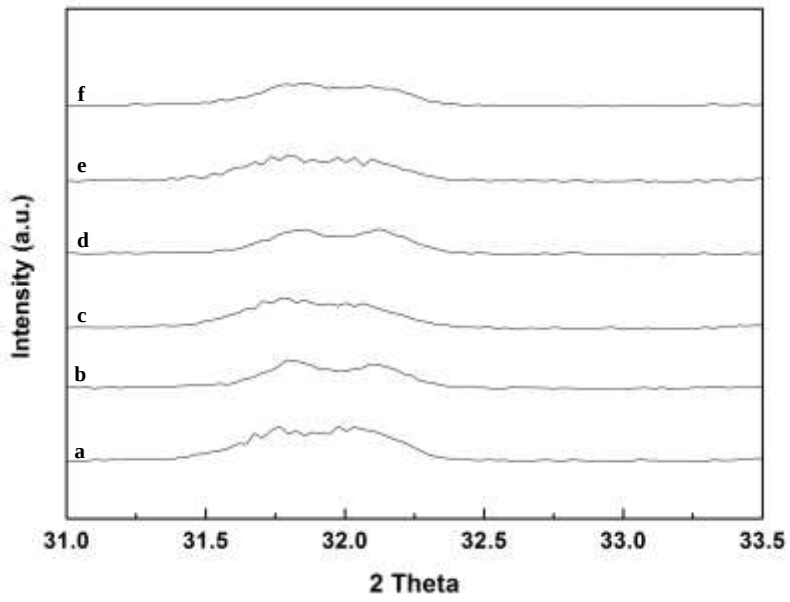

Figure 6.6 High resolution XRD scans of (110) plane of of (a) pure $BiFeO_3$ (b) $BiFeO_3$ with 0.5molar% Ag particles, (c) $BiFeO_3$ with 2molar % Ag particles, (d) $BiFeO_3$ with 0.01vol%Ag NWs, (e) $BiFeO_3$ with 0.1vol% Ag NWs and (f)) $BiFeO_3$ with 0.2vol% Ag NWs

The nucleation mechanisms for $BiFeO_3$ with metallic Ag particles and $BiFeO_3$ with Ag nanowires are different. For $BiFeO_3$ with metallic Ag particles, Ag ions from the $AgNO_3$ precursor are reduced to metallic Ag and nucleate as metallic Ag instead of replacing Bi or Fe ions within the lattice. XPS confirmed the existence of metallic Ag in $BiFeO_3$ thin films. Two characteristic peaks of Ag 3d can be seen at $3d_{3/2}$=374.68eV and $3d_{5/2}$=368.5eV (Figure 6.7). The energy of 6.1eV between the split of two peaks confirms that Ag incorporated into $BiFeO_3$ is in metallic Ag^0 form.[177] Ag was not oxidised to AgO or Ag_2O_3 during annealing. The incorporation of Ag nanowires occurred by the mechanical addition of already nucleated Ag into the $BiFeO_3$ sol. Chemical reactions were not involved. It is believed that Ag nanowires were dispersed next to the $BiFeO_3$ lattice, thereby forming a network for charge transport to occur. XPS failed to detect Ag NWs because the amount of Ag NWs at the surface of the film is below the detection threshold of XPS. However, it

is not expected that Ag nanowires were oxidised as the samples were exposed to the same heat treatment to the $BiFeO_3$ thin films incorporated with Ag by using $AgNO_3$.

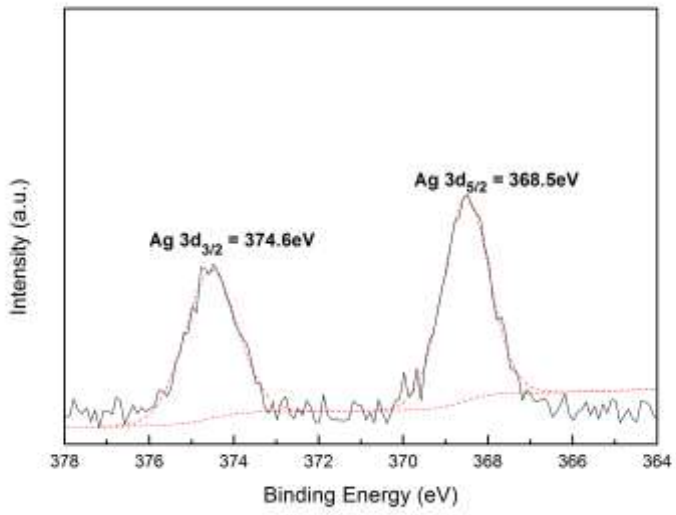

Figure 6.7 XPS spectrum of Ag 3d for $BiFeO_3$ with 2molar% Ag particles. Binding energies confirm the existence of metallic Ag ^{0}

The optical properties of the samples were investigated using UV-Vis Spectroscopy. Figure 6.8 and 6.9 show the absorption curves of pure $BiFeO_3$ and Ag modified $BiFeO_3$ thin films at different Ag concentrations. Significant absorption in the visible light range can be seen due to the narrow band gap of $BiFeO_3$. Additionally, there is an increase in light absorption for Ag modified samples. This is due to the light scattering effect between the Ag particles and Ag nanowires that are dispersed next to $BiFeO_3$ particulates. Scattered photons get trapped within the thickness of the film leading to an enhanced absorption due to longer time of light diffusion.[178]

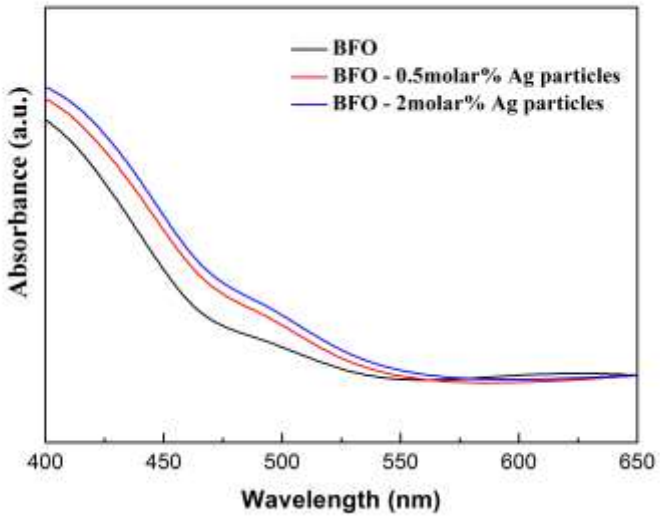

Figure 6.8 Absorbance spectra of pure $BiFeO_3$ and $BiFeO_3$ thin films with metallic Ag particles at different concentrations. Light absorption is enhanced by Ag modificiation

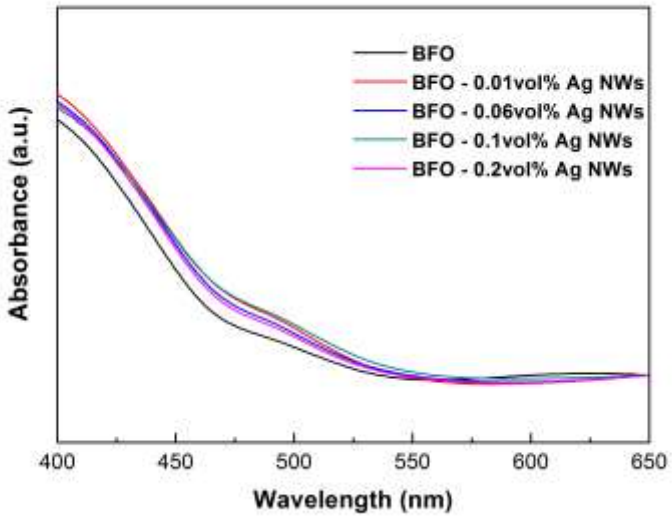

Figure 6.9 Absorbance spectra of pure $BiFeO_3$ and $BiFeO_3$ thin films with Ag NWs at different concentrations. Light absorption is enhanced by Ag modificiation

$BiFeO_3$ has been reported to have both a direct and indirect band gap. Tauc plots were used to estimate the optical band gap using the following equation:

$$\alpha h\nu = A\ (h\nu - E_g)^n \qquad \text{(Eqn 6.1)}$$

where α is the absorbance value, A is a constant, $h\nu$ is the incident photon energy, E_g is band the band gap and n was taken as 1/2 for indirect and 2 for direct band gap calculation. Both fittings clearly show a characteristic slope used to determine the band gap value. Linear extrapolation of $(\alpha h\nu)^n$ to zero indicates an indirect band gap of 2.1eV and a direct band gap of 2.65eV for pure $BiFeO_3$ thin films. There were small variations in band-gap values after Ag modification (Figure 6.10-6.13). This is related to the altered absorption mode because of the light scattering between the Ag and $BiFeO_3$ matrix.

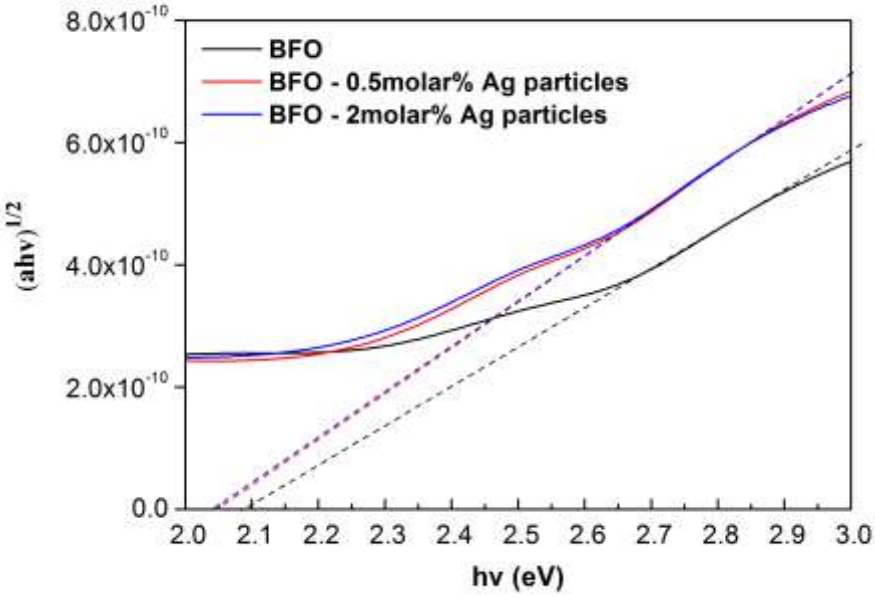

Figure 6.10 Tauc plots of pure $BiFeO_3$ and $BiFeO_3$ thin films with metallic Ag particles at different concentrations for indirect band gap demonstration

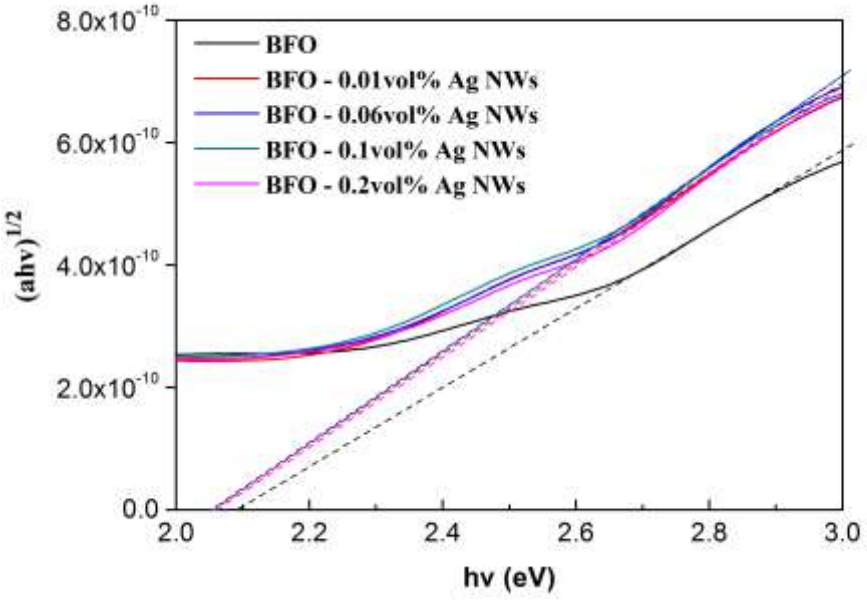

Figure 6.11 Tauc plots of pure $BiFeO_3$ and $BiFeO_3$ thin films with Ag NWs at different concentrations for indirect band gap demonstration

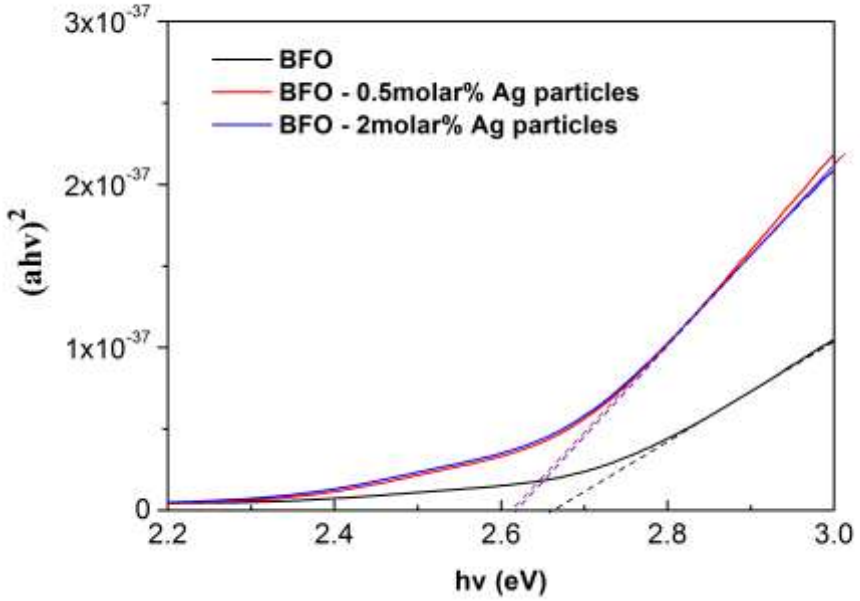

Figure 6.12 Tauc plots of pure $BiFeO_3$ and $BiFeO_3$ thin films with metallic Ag particles at different concentrations for direct band gap demonstration

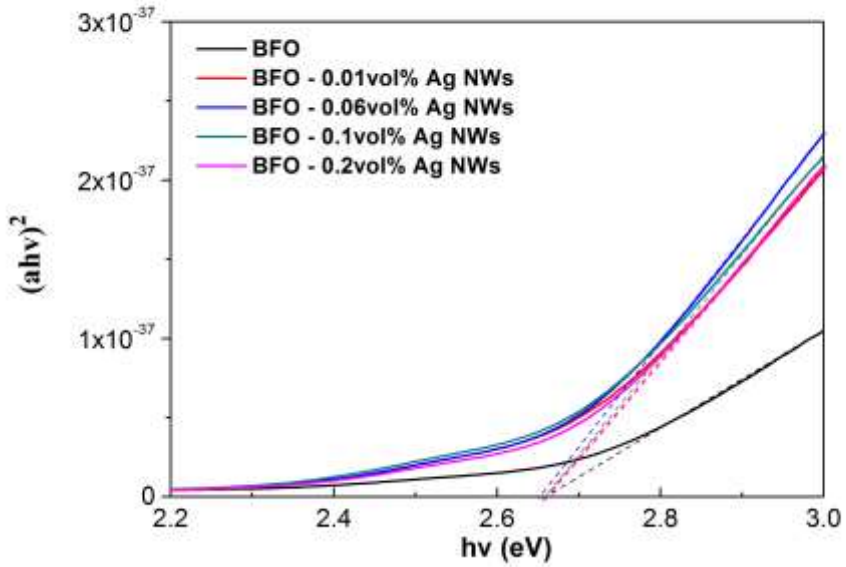

Figure 6.13 Tauc plots of pure $BiFeO_3$ and $BiFeO_3$ thin films with Ag NWs at different concentrations for direct band gap demonstration

6.3. Photoelectrochemical Measurements

6.3.1. Mott-Schottky Plots

Figure 6.14 displays the Mott-Schottky plot for pure $BiFeO_3$ thin film produced on FTO coated glass. P-type behaviour was exhibited by the films and is confirmed by the negative slope of the curves. Both p and n type conductivity have been reported for $BiFeO_3$ depending on its element deficiencies. It was shown that $BiFeO_3$ grown in reducing conditions with oxygen vacancies has n-type conductivity whereas Bi and Fe vacancies formed in oxidising condition result in p-type conductivity. The p-type conductivity in films produced in this project is due to the oxidising conditions used during pre-annealing and annealing.

The flat band potential of pure $BiFeO_3$ was estimated to be 1.15V (vs NHE, pH = 7). This value is close to valence band of the $BiFeO_3$ but below the water oxidation level.

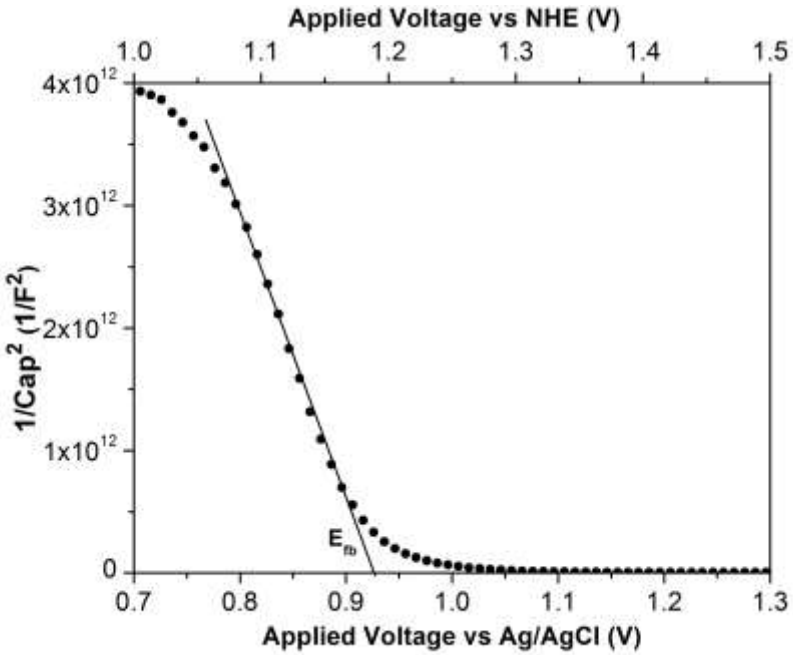

Figure 6.14 Mott Schottky plot for pure $BiFeO_3$ in dark in 0.01M Na_2SO_4

Figure 6.15 and 6.16 displays the Mott-Schottky plots for $BiFeO_3$ incorporated with Ag at different concentrations. There was a slight negative shift for E_{fb} values after Ag modification. E_{fb} becomes 1.1V (vs RHE, pH =7) for all Ag modified samples except for $BiFeO_3$ with 0.06vol% and 0.2vol% Ag NWs where a shift was not observed.

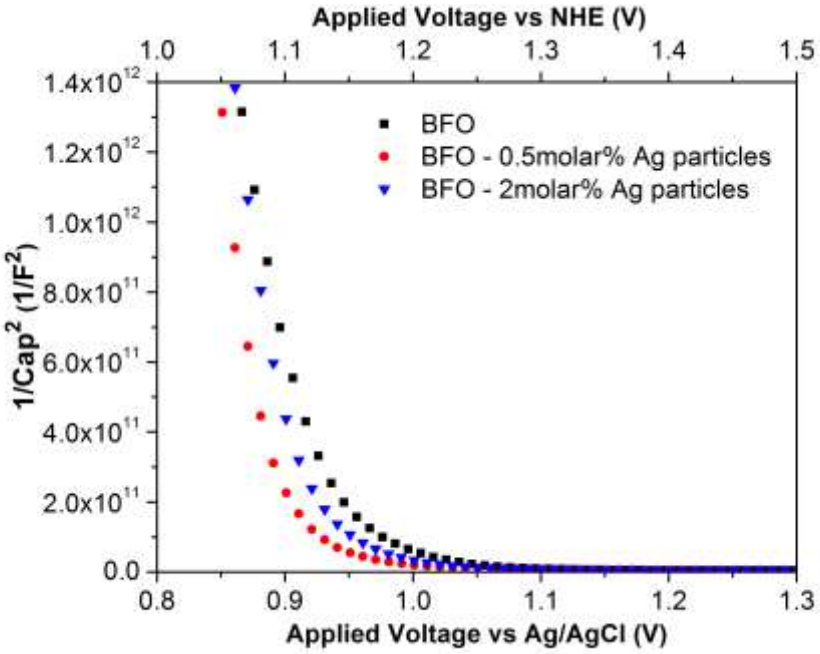

Figure 6.15 Mott Schottky plots for $BiFeO_3$ and $BiFeO_3$ thin films with metallic Ag particles at different concentrations measured in dark in 0.01M Na_2SO_4

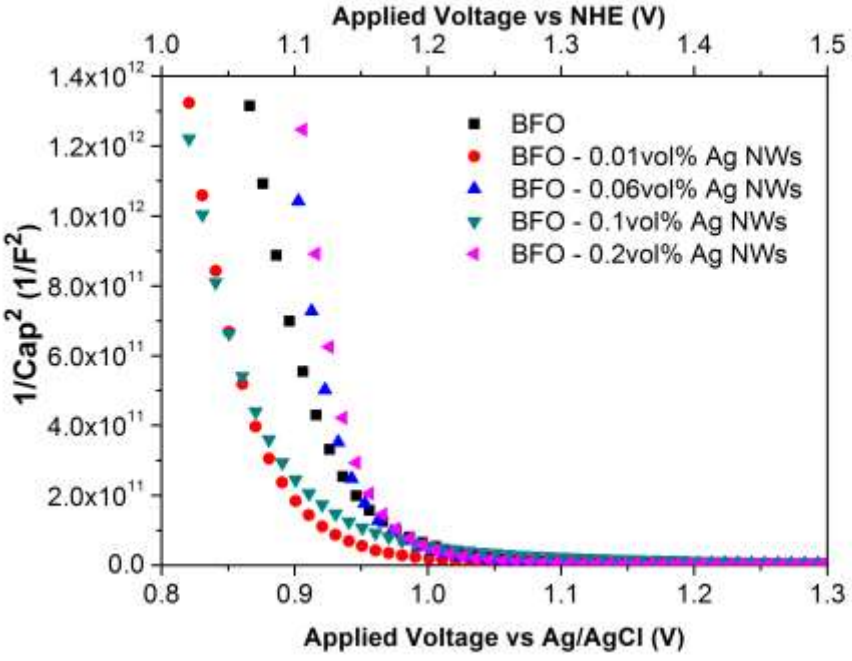

Figure 6.16 Mott Schottky plots for $BiFeO_3$ and $BiFeO_3$ thin films with Ag NWs at different concentrations measured in dark in 0.01M Na_2SO_4

The shift in E_{fb} is related to the Schottky junction formed at the Ag/$BiFeO_3$ interface. The Fermi level of Ag (+0.4V vs RHE) is below the conduction band of $BiFeO_3$ (+0.1V vs RHE) (Figure 6.17). Similar to Pd deposition onto TiO_2, the presence of Ag decreases the degree of band bending and shifts the Fermi level by 0.05V to a more negative level.

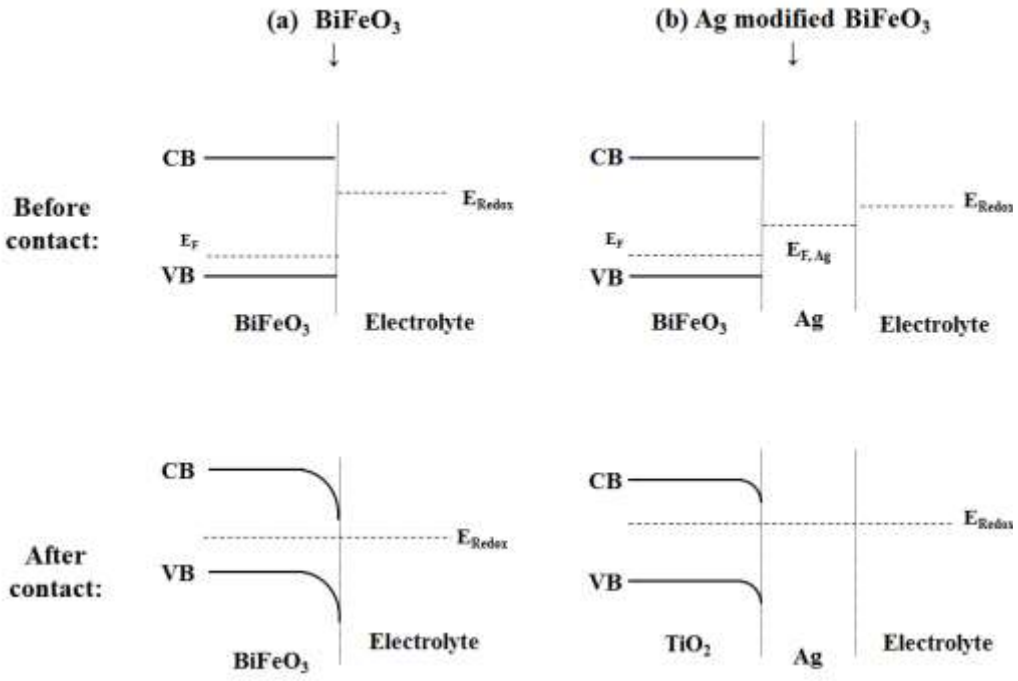

Figure 6.17 Schematic representations of energy band levels of (a) pure $BiFeO_3$ and (b) Ag incorporated $BiFeO_3$ with the electrolyte before and after contact in the dark. The band bending is reduced by Ag incorporation due to the Fermi level of Ag

The carrier density (N_D) of the samples can be calculated using the following Equation 6.1:

$$N_D = \frac{2}{e\,\varepsilon_0\varepsilon}\left(\frac{dE}{d\left(\frac{1}{C^2}\right)}\right) \qquad \text{Eqn (6.2)}$$

where e = 1.6 x 10^{-19}C, ε_0 is the permittivity of vacuum (=8.86x10^{-12} F/m), ε is the relative permittivity of the semiconductor (=53 for rutile $BiFeO_3$)[179]. dE/d(1/C^2) values were determined the slope of the curves in Mott-Schottky plots. The slopes of the Mott-Schottky curves are similar; therefore, calculated charge carrier densities values of each sample are close to each other and were calculated to be $N_D \sim 2x10^{15}$ cm^{-3}.

6.3.2. J-V Curves

The photocurrents of $BiFeO_3$ thin films with different layers under dark and light have been investigated. A photodiode j-v curve could not be obtained for the 1-Layer $BiFeO_3$ thin film. This is because there was not full coverage of thin film on the substrate and FTO was also exposed to the electrolyte which dominated the photoresponse.

Figure 6.18 shows the photocurrent measurements of 2-layer $BiFeO_3$ and 3-layer $BiFeO_3$ thin film under dark and light. A higher photocurrent has been observed for the 2-layer $BiFeO_3$ thin film deposited on FTO coated glass. The inferior photoelectrochemical performance of the 3-layer $BiFeO_3$ thin film is due to the increased grain boundaries present between the layers which can act as recombination centres.

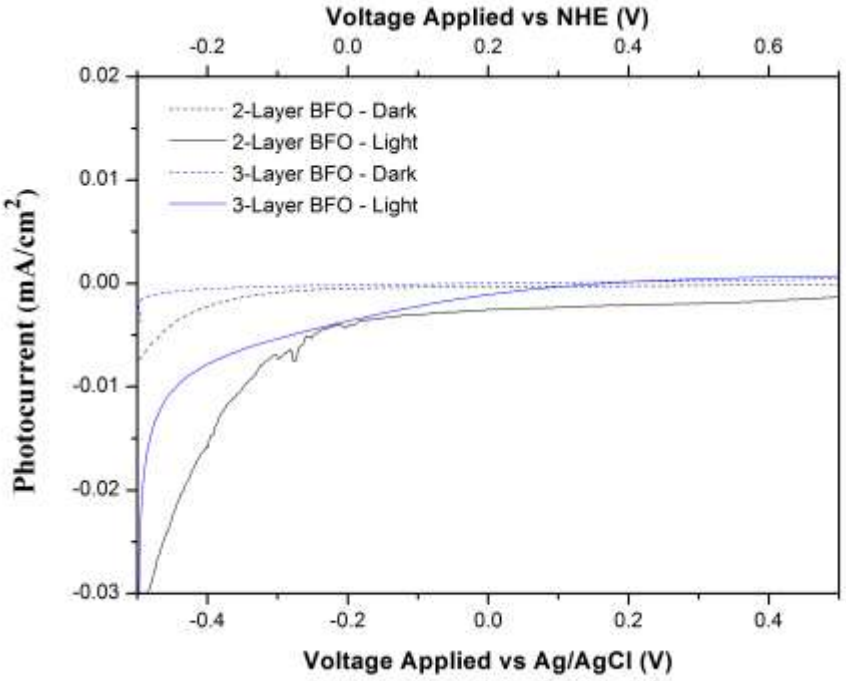

Figure 6.18 Photocurrent densities of 2-layer $BiFeO_3$ and 3-layer $BiFeO_3$ thin films with a scan rate of 10mV/s in 0.01M Na_2SO_4 solution

The photoelectrochemical performances of 2-layer BiFeO3 thin films with different Ag concentrations were investigated. The dark currents of all samples were insignificant. All films showed photocathodic performance giving current at negative voltages under illumination. A photocurrent density of -0.004mA/cm^2 was achieved by pure $BiFeO_3$ thin films (Reminder: 2-layer $BiFeO_3$) at 0V vs NHE under AM1.5 G illumination.

PEC responses for $BiFeO_3$with metallic Ag structures are shown in Figure 6.19. There is a correlation with photocurrent and Ag concentration whereby photocurrent increased with increasing Ag concentration. The onset potential shifted towards more positive voltages at Ag modified samples resulting in enhanced cathodic photocurrents. The positive shift in onset potential indicates reduced overpotential losses and can be ascribed to improved charge trapping and decreased band bending induced by the presence of Ag.[179,180,181] The decrease in band bending facilitates the

electron transfer at the interface of $Ag/BiFeO_3$.[102] Ag acts as an electron sink and scavenges electrons from the conduction band of $BiFeO_3$. This prohibits their recombination with holes at lower energy states, thereby leading to efficient charge separation and, hence a higher photocurrent. The highest photocurrent was obtained from $BiFeO_3$ with 2 molar% Ag particles -0.07mA/cm^2 at 0V vs NHE which shows a 17-fold increase in photocurrent compared to pure $BiFeO_3$.

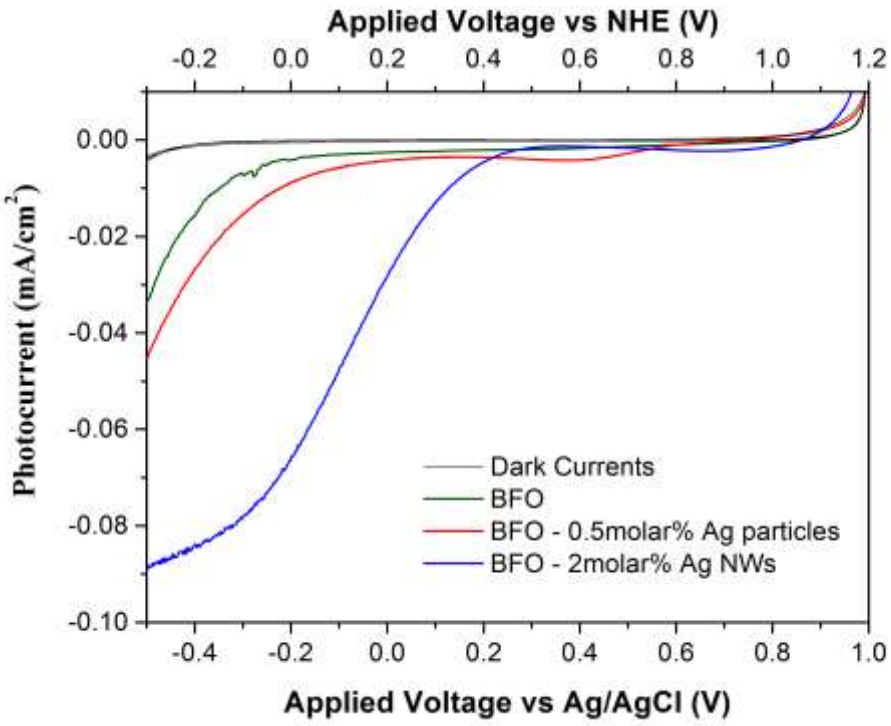

Figure 6.19 Photocurrent density of $BiFeO_3$ and $BiFeO_3$ thin films with metallic Ag particles at different concentrations. The scan rate was 10mV/s in 0.01M Na_2SO_4 solution

For the samples modified with the incorporation of Ag nanowires, there was also a clear trend between photocurrent and nanowire concentration (Figure 6.20). The highest photocurrent was achieved using $BiFeO_3$ incorporated with 0.1vol% Ag NWs which is -0.05mA/cm^2 at 0V vs NHE. The onset potential of this sample is also shifted to more positive voltages suggesting lower overpotentials compared to pure $BiFeO_3$ and other Ag NWs loaded $BiFeO_3$ thin films. This improved photocurrent

can be attributed to the enhanced charge generation due to the light scattering effect and enhanced charge separation, as with the case of metallic Ag particles.

In addition to trapping electrons from $BiFeO_3$'s conduction band, the Ag nanowires create a pathway for electrons to transfer easily to the surface to interact with the electrolyte therefore increasing the carrier mobility and the resulting photocurrent of the films. The shape of the j-v curve 三 for $BiFeO_3$ with 0.1vol% Ag NWs and $BiFeO_3$ with 2molar% Ag particles is also different compared to others. The slope of the curves is steeper with a sharp increase in the photocurrent at more negative voltages suggesting higher charge carrier mobility.[182,183]

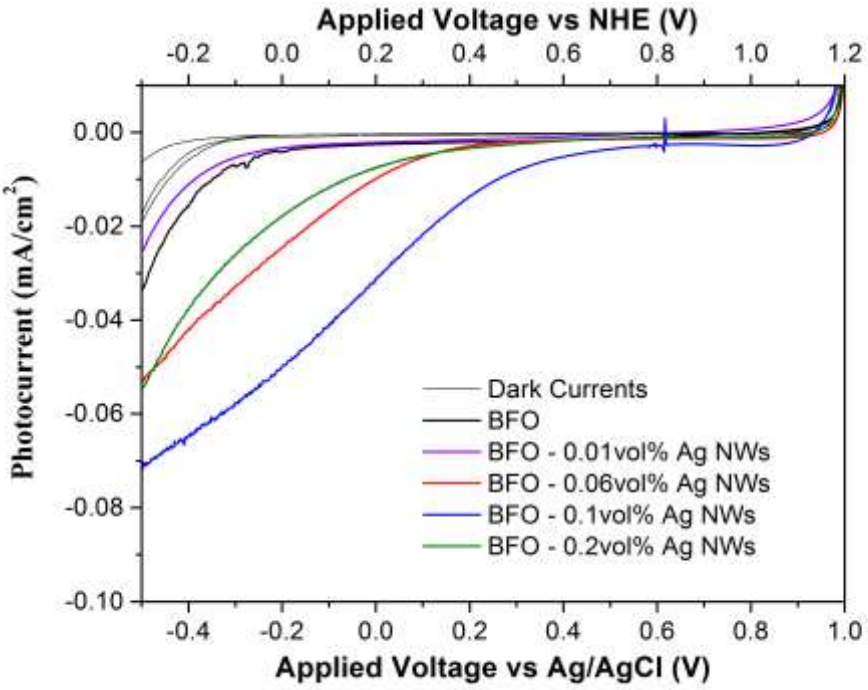

Figure 6.20 Photocurrent densities of $BiFeO_3$ and $BiFeO_3$ thin films with Ag NWs at different concentrations. The scan rate was 10mV/s in 0.01M Na_2SO_4 solution

6.4. Photo-oxidation of Water

Water splitting was conducted with three different samples; pure $BiFeO_3$ thin film, $BiFeO_3$ with 2molar% Ag and $BiFeO_3$ with 0.1vol% Ag NWs. These Ag concentrations were chosen as they gave the highest photocurrent among the Ag modified samples. Figure 6.21 shows the j-V curves of the films when the illumination was interrupted by a mechanical light chopper. The photoresponse of all samples starts at high positive voltages (1.0V vs Ag/AgCl) which match with the E_{fb} values.

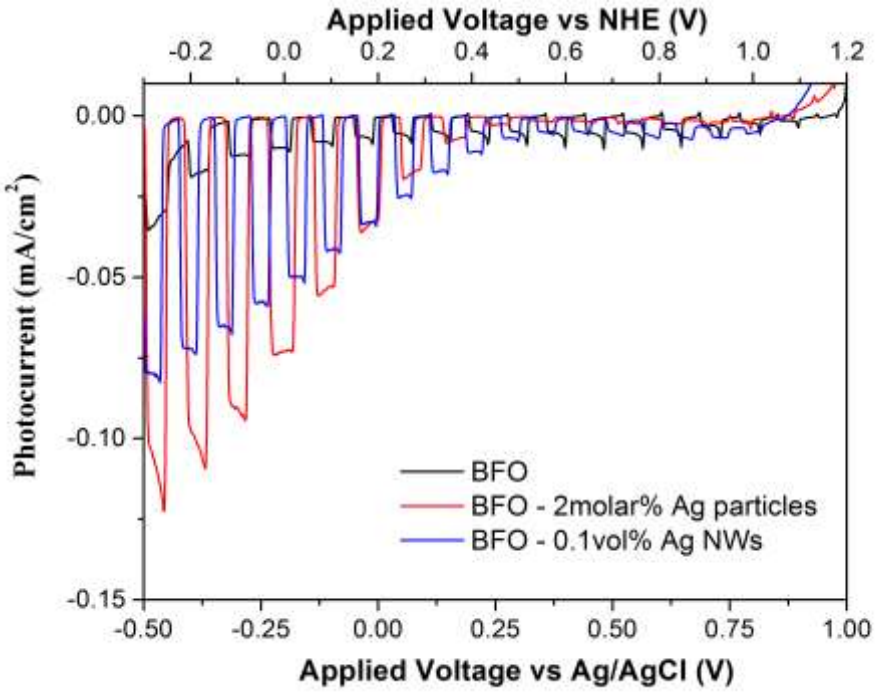

Figure 6.21 Photocurrent density of $BiFeO_3$, $BiFeO_3$ with 0.1vol% Ag NWs and $BiFeO_3$ with 2molar% Ag particles under interrupted illumination. The scan rate was 10mV/s in 0.01M Na_2SO_4 solution

Only half cell reaction of the water splitting was successful. Oxygen was successfully obtained by photo-oxidation of water; however, hydrogen was not produced. This is mostly the case in photoelectrocatalysis reports for $BiFeO_3$ thin films or particles. The studies include the photo-oxidation of water to evaluate oxygen gas whereas the studies for H_2 evolution by BFO are limited. It was Ji et al.'s

BFO thin film sputtered on SRO buffered STO substrates that managed to evaluate both H_2 and O_2 without external bias as it was shown by UPS that the band edges straddled the water redox levels.[184] Deng et al. coated Ti foil by BFO particles and achieved both H_2 and O_2 formation with photoelectrochemical and photocatalytic tests.[185] Luo et al. coated BFO nanoparticles with crystalline $SrTiO_3$ to successfully produce H_2 in presence of CH_3OH_3 under no external bias as pure BFO failed to reduce protons to evaluate hydrogen gas.[125]

The limitation for hydrogen production by BFO is attributed to the positions of the band levels relative to water reduction and oxidation potentials. The estimated band levels of $BiFeO_3$ are presented in Figure 6.22. The conduction band of $BiFeO_3$ is below hydrogen reduction level resulting in a significant potential barrier. Applied external bias of -0.5V vs Ag/AgCl was not sufficient for the photoelectrons do not to overcome the potentials and reduce the hydrogen protons. H^+ ions stay in the solution as proton and H_3O^+; however, the difference in pH wasn't detected by our pH meter due to its small production. Since there was no electron acceptor in the solution, we believe photogenerated electrons can do reduction chemistry with the $BiFeO_3$ itself. The valence state of Fe varies in $BiFeO_3$and reduction of Fe (Fe^{3+} to Fe^{2+}) by electrons is plausible forming structures of $Bi_xFe_{2-x}O_{y-1}$.

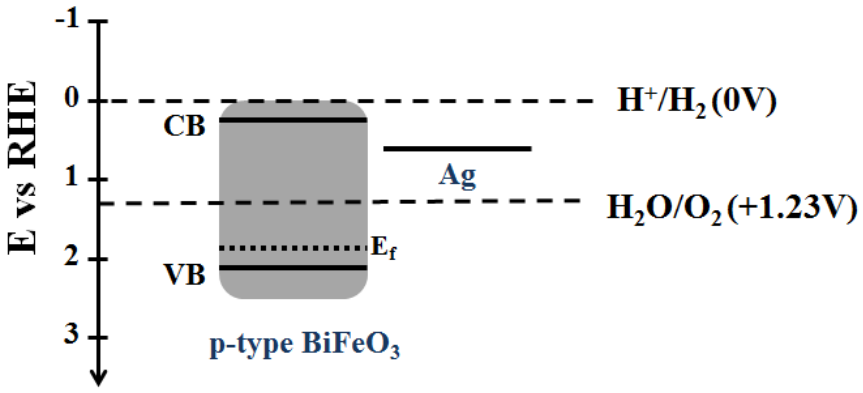

Figure 6.22 Estimated location of band levels and Fermi level of p-type $BiFeO_3$ and Ag

The influence of Ag modification on water oxidation was investigated. The total amounts of photogenerated oxygen for pure $BiFeO_3$ thin film, $BiFeO_3$ with 2molar% Ag particles and $BiFeO_3$ with 0.1vol% Ag NWs are summarised in Table 6.1. The small production of O_2 is a result of limited ion transfer due to lack of ionic solution as the water splitting process was carried out with pure deionized water. Oxygen evolution reached saturation and stopped with pure $BiFeO_3$ thin film in the first 0.5h giving only 1.2μmol of O_2. Ag modified samples produced a higher amount of oxygen compared to pure $BiFeO_3$ under the same conditions. Total O_2 produced was 9.6μmol and 25.4μmol by the end of 20h for $BiFeO_3$ with 0.1vol% Ag NWs and $BiFeO_3$ with 2molar% Ag particles.

The enhanced performance can be attributed to the increased availability of photoactive holes. The recombination rate is reduced due to the electron trapping role of Ag as previously discussed. The electrons are scavenged by Ag from the conduction band of $BiFeO_3$ which leaves photoactive holes for oxidation of water.

Table 6.1 Amount of photogenerated oxygen evolution for pure $BiFeO_3$, $BiFeO_3$ with 0.1% Ag NWs and $BiFeO_3$ with 2% Ag NWs at -0.5V vs Ag/AgCl

O_2 Evolution (µmol/cm^2)			
	1h	***2h***	***20h***
$BiFeO_3$	1.2	1.2	1.2
$BiFeO_3$ - 0.1vol% Ag NWs	2.7	5.4	9.6
$BiFeO_3$ – 2molar% Ag particles	1.2	6.6	25.2

6.5. Summary

This chapter has outlined the development of photoelectrodes based on $BiFeO_3$ thin films – one of the most popular ferroelectric photocatalysts. The photocatalytic activity of samples was studied by photo-oxidation of water. $BiFeO_3$ thin films was deposited on FTO coated glass by a simple sol-gel method to produce photoelectrodes for water splitting. The films showed p-type behaviour with a flat band potential of 1.15V (vs RHE, pH=7). The p-type conductivity is a result of the oxidising conditions in sol-gel synthesis and annealing. Photocurrent density of -0.004mA/cm^2 was achieved by pure $BiFeO_3$ thin films at 0V vs NHE under AM1.5 G illumination. This value was further increased by Ag modification where Ag was incorporated into the $BiFeO_3$ matrix at different concentrations as metallic Ag structures and Ag NWs. The samples were analysed by characterisation methods such as SEM, XRD, TEM and XPS. Optical properties were investigated by UV-Vis spectroscopy. It was found that light absorption was enhanced by the addition of Ag which was credited to the light scattering effect between the Ag and $BiFeO_3$ matrix. Optical band gap values were calculated from absorbance curves. An indirect band gap of 2.1eV and direct band gap of 2.65eV were estimated for pure $BiFeO_3$ thin

films. There were small variations in band-gap values after Ag modification which was again related to light-scattering. Photocurrents of $BiFeO_3$ with different Ag concentration were studied. There are clear trends to the photocurrent and amount of photogenerated O_2 gas obtained at different concentrations of Ag. Highest photocurrent was achieved with $BiFeO_3$ with 2molar% Ag particles and $BiFeO_3$ with 0.1vol% Ag NWs with photocurrents of -0.07mA/cm^2 and -0.05mA/cm^2, respectively. These two samples along with pure $BiFeO_3$ thin film were then tested for photoelectrocatalytic water splitting of pure deionised water at an applied voltage of -0.5V (vs Ag/AgCl). Only half cell reaction was completed; no hydrogen evolution was detected. Oxygen evolution amount was significantly enhanced by Ag modified $BiFeO_3$ compared to pure $BiFeO_3$ thin films. The credit was given to reduced overpotential losses and efficient charge separation by Ag which acts as electron sinks and surpasses recombination with holes.

CHAPTER 7: CONCLUSIONS AND FUTURE WORK

7.1. Conclusions

The aim of this work was to investigate the photocatalytic performance of two different systems based on n-type TiO_2 nanorods and p-type $BiFeO_3$ thin films. The photoactivity of the systems were analysed through photodecolourisation of a common textile dye Rhodamine B and photogeneration of hydrogen and oxygen under solar simulator. The influence of metal loading on photoactivity, where Pd was deposited onto TiO_2 nanorods and Ag was incorporated into $BiFeO_3$ thin films, was investigated by a variety of photoelectrochemical tests.

The first stage was to develop a photocatalyst system with high surface area TiO_2 nanorods grown on glass fibre substrates and to investigate the effect of annealing and Pd nanoparticle loading on photoactivity. The aim was to produce a mechanically robust photocatalyst system as a photocatalytic filter alternative to powder photocatalyst systems used for waste water treatment. The first trial for the production of the catalyst was an aqueous method whereby ZnO nanorods previously grown on glass fibres were converted to TiO_2 nanorods. Although the full chemical conversion was successful, the photocatalyst failed to show a good photocatalytic activity for the photodecolourisation of Rhodamine B due to insufficient crystallinity and surface area. The production method was then changed to hydrothermal

synthesis where rutile TiO_2 nanorods were directly grown on glass fibre substrates. The nanorods formed were in rutile phase with high crystallinity.

The photoactivity of the catalyst system was studied through decolourisation of a common textile dye – Rhodamine B (RhB). Full photodecolourisation of RhB (10 ppm) was achieved within 180 minutes with as-grown TiO_2 nanorods. The annealing of the TiO_2 nanorods did not have any effect on photoactivity of the system as the crystallinity was not immensely improved by annealing. The influence of Pd metal loading on TiO_2's photoactivity was further investigated. Pd nanoparticles were deposited onto TiO_2 nanorods via photochemical method which was successfully confirmed by TEM and XPS. It was found that the hybrid Pd/TiO_2 catalyst system showed higher photoactivity where full decolourisation occurred in 90 minutes. The credit in enhancement of photoactivity by Pd loading was given to localised surface plasmon resonance (LSPR) effect due to interaction of Pd with visible light and the electron scavenging role of Pd for efficient charge separation to surpass recombination which was explained by the mechanism. The recyclability tests showed that the reused hybrid Pd/TiO_2 catalyst system had a good catalytic performance that is similar to the original samples.

The next stage was to replicate the same photocatalyst system on a conductive substrate so that photoelectrochemicals experiments could be carried out. In this respect, the Pd/TiO_2 photocatalyst system was produced on FTO coated glass substrate. The production method was the same with the photocatalyst system on the glass fibres substrates where metallic Pd nanoparticles were deposited by a photochemical method onto TiO_2 nanorods that were hydrothermally grown on the substrate. The samples were photoelectrochemically characterised by a potentiostat with tests for i-v and i-t measurements under dark and illumination, Mott-Schottky

curves for estimation of flat-band potential and electrochemical impedance spectroscopy (EIS) to understand the charge transfer kinetics at the Pd/TiO_2/electrolyte interface. The flat band potential of TiO_2 was estimated to be -0.45V (vs NHE, pH = 7) and there was a positive shift in flat band potential when Pd was loaded onto TiO_2 due to the relative position of Pd's Fermi level to the conduction band of TiO_2. Pd loading induced a decrease in band bending which implies a facilitated electron transfer between Pd and TiO_2. Nyquist plots from EIS data confirmed this by a smaller arc size measure for Pd/TiO_2 which indicates a lower resistance against as the charge transfer.

The photoelectrochemical performance of the bare TiO_2 and hybrid Pd/TiO_2 samples were then compared depending on their photoactivities on the decolourisation of a standard commercial textile dye Rhodamine B (RhB) and solar hydrogen production in different electrolyte solutions at various applied voltage values. Hybrid photocatalyst Pd/TiO_2 showed enhanced photoelectrocatalytic activity in decolourisation RhB in aqueous solution. A higher amount of hydrogen by Pd/TiO_2 was photogenerated in methanol solution. However, bare TiO_2 samples produced a higher amount of hydrogen in 0.01M Na_2SO_4 and pure deionised water under same conditions. The role of methanol as a hole scavenger helped the efficient charge separation so that the electrons trapped by Pd could contribute to the hydrogen reduction. The results were explained by possible mechanisms of photoelectrochemistry proposed for both dye degradation and solar hydrogen production.

Finally, the photoelectrochemical activity of a p-type photocatalyst based on $BiFeO_3$ was investigated. $BiFeO_3$ thin films were deposited on large scale FTO coated glass by a sol-gel method. The photoelectrochemical properties were further analysed after

Ag modification. Ag was incorporated into the $BiFeO_3$ matrix at different concentrations as metallic Ag structures and Ag nanowires. The light absorption was enhanced by the addition of Ag which was due to the light scattering between the Ag and $BiFeO_3$ matrix. An indirect band gap of 2.1eV and direct band gap of 2.65eV were estimated for pure $BiFeO_3$ thin films with small variations after Ag modification. All of the films showed p-type behaviour with a flat band potential of 1.15V (vs NHE, pH=7) for pure $BiFeO_3$. Ag modification induced a small negative shift in flat band potential due to the reduced band bending.

Photocurrents of $BiFeO_3$ with different Ag concentration were investigated. Photocurrent density of -0.004mA/cm^2 was achieved by pure $BiFeO_3$ thin films at 0V vs NHE under AM1.5 G illumination. For the Ag modified $BiFeO_3$ samples, the highest photocurrent was achieved for $BiFeO_3$ with 2molar% metallic Ag structures and $BiFeO_3$ with 0.1vol% Ag nanowires with photocurrents of -0.07mA/cm^2 and -0.05mA/cm^2, respectively. Photoelectrocatalytic water splitting of pure deionised water with these three samples was carried out at an applied voltage of -0.5V (vs Ag/AgCl). Only half cell reaction was successful and only oxygen evolution occurred whereas hydrogen evolution was not detected. The oxygen evolution amount was immensely enhanced by Ag modified $BiFeO_3$ compared to the pure $BiFeO_3$ thin films. The significant increase in photocurrent and corresponding amount of photogenerated O_2 gas were attributed to reduced overpotential losses and efficient charge separation by the Ag particles.

7.2. Future Work

A range of ideas that could be further carried out for this project are suggested in this section. The recommendations for future work include:

- Loading of different precious metals onto TiO_2 nanorods: A comparison study on photoelectrochemical activity of TiO_2 nanorods with different metals (other than Pd) can be investigated. The potential metals for such study could be Ag, Au, Pt and Ru. The difference in work function values of each metal will result in different degrees of band bending and subsequent Schottky barrier heights. This will massively influence the charge separation efficiency and the electron and hole trapping ability which in return will have a significant effect on the photoelectrochemical performance of each system.
- Developing a hydrid photocatalyst system with n-type TiO_2 and p-type $BiFeO_3$: This could be achieved in two ways. Firstly, instead of using a counter electrode to act like a cathode or anode depending on the conductivity type of the working electrode, the system could be combination of photoelectrodes where TiO_2 as a photoanode and $BiFeO_3$ as a photocathode can be used and can be both illuminated. Secondly, semiconductor coupling could be performed where a p-type $BiFeO_3$ thin film is deposited on n-type TiO_2 nanorods to obtain a pn junction. This system would improve the charge separation and subsequent photoelectrocatalytic performance.
- Processing of $BiFeO_3$ thin films: As discussed previously, atmospheric conditions during the synthesis of $BiFeO_3$ have a significant influence on the type of $BiFeO_3$ conductivity. It was shown that $BiFeO_3$ synthesised in reducing conditions have oxygen vacancies which results in n-type conductivity, whereas Bi and Fe vacancies formed in oxidising conditions result in p-type $BiFeO_3$. The BiFeO3 thin films in this project have p-type conductivity due to the oxidising conditions used during pre-annealing and annealing. Reducing conditions, such as annealing

in N_2 gas, could be attempted in order to produce n-type $BiFeO_3$ thin films. A coupling system with n and p type $BiFeO_3$ could also be formed.

REFERENCES

1. Muhd Julkapli, N., Bagheri, S. & Bee Abd Hamid, S. Recent Advances in Heterogeneous Photocatalytic Decolorization of Synthetic Dyes. *Sci. World J.* **2014,** 1–25 (2014).
2. Honda, K. and Fujishima, A. Electrochemical Photolysis of Water at a Semiconductor Electrode. *Nature* **238,** 37–38 (1972).
3. Liao, C.-H., Huang, C.-W. & Wu, J. C. S. Hydrogen Production from Semiconductor-based Photocatalysis via Water Splitting. *Catalysts* **2,** 490–516 (2012).
4. Walter, M. G. *et al.* Solar water splitting cells. *Chem. Rev.* **110,** 6446–6473 (2010).
5. Ibhadon, A. O. & Fitzpatrick, P. Heterogeneous Photocatalysis: Recent Advances and Applications. *Catalysts* **3,** 189–218 (2013).
6. Lam, S.-M., Sin, J.-C., Abdullah, A. Z. & Mohamed, A. R. Degradation of wastewaters containing organic dyes photocatalysed by zinc oxide: a review. *Desalin. Water Treat.* **41,** 131–169 (2012).
7. Vayssieres, L. *On Solar Hydrogen & Nanotechnology*. (2009).
8. Graetzel, M. Photoelectrochemical cells. *Nat. Mater.* **414,** (2001).
9. Ola, O. & Maroto-Valer, M. M. Review of material design and reactor engineering on TiO2 photocatalysis for CO2 reduction. *J. Photochem. Photobiol. C Photochem. Rev.* **24,** 16–42 (2015).
10. Nozik, A. J. Photoelectrochemistr Y : Conversion. *Ann. Rev. Phys. Chem* **29,** 189–222 (1978).
11. Ni, M., Leung, M. K. H., Leung, D. Y. C. & Sumathy, K. A review and recent developments in photocatalytic water-splitting using TiO2 for hydrogen production. *Renew. Sustain. Energy Rev.* **11,** 401–425 (2007).
12. Pillai, S., Pelaez, M. & Kontosd, A. G. A Review on the Visible Light Active Titanium Dioxide Photocatalysts for Environmental Applications. **125,** 331–349 (2012).
13. Huang, W., Wang, X., Xue, Y., Yang, Y. & Ao, X. Hybrid nanostructures of mixed-phase TiO_2 for enhanced photoelectrochemical water splitting. *RSC Adv.* **5,** 56098–56102 (2015).
14. Daghrir, R., Drogui, P. & Robert, D. Modified TiO2 for environmental photocatalytic applications: A review. *Ind. Eng. Chem. Res.* **52,** 3581–3599 (2013).

15. Cui, Y., Briscoe, J. & Dunn, S. Effect of Ferroelectricity on Solar-Light-Driven Photocatalytic Activity of BaTiO 3 □Influence on the Carrier Separation and Stern Layer Formation. (2013).

16. Stock, M. & Dunn, S. Influence of the Ferroelectric Nature of Lithium Niobate to Drive Photocatalytic Dye Decolorization under Artificial Solar Light. (2012).

17. Zhang, X. *et al.* Preparation of M@BiFeO $_3$ Nanocomposites (M = Ag, Au) Bowl Arrays with Enhanced Visible Light Photocatalytic Activity. *J. Am. Ceram. Soc.* **98,** 2255–2263 (2015).

18. Arnold, D. C. Composition-Driven Structural Phase Transitions in Rare-Earth-Doped BiFeO 3 Ceramics : A Review. *Ieee Trans. Ultrason. Ferroelectr. Freq. Control* **62,** 62–82 (2015).

19. Edmund, B. Memoire sur les effets électriques produits sous li'influence des rayons solaires. *C. R. Acad. Sci* **9,** 561–567 (1839).

20. Brattain, W.H. and Garrett, C. G. B. Experiments on the interface between germanium and an electrolyte. *Bell Sys. Tech. J.* **34,** 95 (1955).

21. Patterson, J. and Bailey, B. *Solid-State Physics: Introduction to the Theory*. (Springer, 2010).

22. Wert, C. A. and Thomson, R. M. *Physics of Solids*. (McGraw-Hill, 1970).

23. Meyers, H. P. *Introductory Solid State Physics*. **2,** (CRC Press, 1997).

24. Callister, W. & Rethwisch, D. *Materials science and engineering: an introduction*. *Materials Science and Engineering* **94,** (2007).

25. Colinge, J. P. *Physics of Semiconductor Devices*. (Springer, 2002).

26. Roy, N. B. *Fundamentals of Classical and Statistical Thermodynamics*. (Wiley, 2002).

27. Brennan, K. F. *The Physics of Semiconductors: With Applications to Optoelectronic Devices*. (Cambridge University Press, 1999).

28. Gerischer, H. Electron-transfer kinetics of redox reactions at the semiconductor/electrolyte contact. A new approach. *J. Phys. Chem.* **95,** 1356–1359 (1991).

29. Nozik, a. J. & Memming, R. Physical Chemistry of Semiconductor - Liquid Interfaces. *J. Phys. Chem.* **100,** 13061–13078 (1996).

30. Rajeshwar, K. Fundamentals of Semiconductors Electrochemistry and Photoelectrochemistry. (2001).

31. Radecka, M., Rekas, M., Trenczek-Zajac, a. & Zakrzewska, K. Importance of the band gap energy and flat band potential for application of modified TiO2 photoanodes in water photolysis. *J. Power Sources* **181,** 46–55 (2008).

32. Bott, A. W. & Ph, D. Electrochemistry of Semiconductors. *Sol. Energy* **8,** 136 (1964).

33. Dung, D., Ramsden, J. & Graetzel, M. Dynamics of interfacial electron-transfer processes in colloidal semiconductor systems: Journal of the American Chemical Society. *J. Am. Chem. Soc.* **104,** 2977–2985 (1982).

34. Beranek, R. (Photo)electrochemical Methods for the Determination of the Band Edge Positions of TiO2-Based Nanomaterials. *Adv. Phys. Chem.* **2011,** 1–20 (2011).

35. Chen, Z., Huyen, D., Miller, E. *Photoelectrochemical Water Splitting: Standards, Experimental Methods, and Protocols*. (Springer, 2013).

36. Lvovich, V. F. *Impedance Spectroscopy: Applications to Electrochemical and Dielectric Phenomena*. (John Wiley and Sons, 2012).

37. Campanella, H. *Acoustic Wave and Electromechanical Resonators: Concept to Key Applications*. (Artech House, 2010).

38. Guermazi, M., Tröltzsch, U., Kanoun, O. & Derbel, N. Assessment of beef meat aging using impedance spectroscopy. *Int. Multi-Conference Syst. Signals Devices, SSD'11 - Summ. Proc.* (2011). doi:10.1109/SSD.2011.5767450

39. Barsoukov, E. & Macdonald, J. R. *Impedance Spectroscopy*. *Impedance Spectroscopy: Theory, Experiment, and Applications* (2005). doi:10.1002/0471716243

40. Bak, T., Nowotny, J., Rekas, M. & Sorrell, C. . Photo-electrochemical hydrogen generation from water using solar energy. Materials-related aspects. *Int. J. Hydrogen Energy* **27,** 991–1022 (2002).

41. Yong, X. & Schoonen, M. a a. The absolute energy positions of conduction and valence bands of selected semiconducting minerals. *Am. Mineral.* **85,** 543–556 (2000).

42. Hashimoto, K., Irie, H. & Fujishima, A. Photocatalysis: A Historical Overview and Future Prospects. *Jpn. J. Appl. Phys.* **44,** 8269–8285 (2005).

43. Hashimoto, K., Irie, H. & Fujishima, A. TiO 2 Photocatalysis: A Historical Overview and Future Prospects. *Jpn. J. Appl. Phys.* **44,** 8269–8285 (2005).

44. Vaidya & A. A., Datye, K. V. Environmental pollution during chemical processing of synthetic fibers. *Colourage* 29 (1982).

45. Khataee, A. R., Zarei, M. & Moradkhannejhad, L. Application of response surface methodology for optimization of azo dye removal by oxalate catalyzed photoelectro-Fenton process using carbon nanotube-PTFE cathode. *Desalination* **258,** 112–119 (2010).

46. Chang, S. M., Lo, P. H. & Chang, C. T. Photocatalytic behavior of TOPO-capped TiO2 nanocrystals for degradation of endocrine disrupting chemicals. *Appl. Catal. B Environ.* **91,** 619–627 (2009).

47. Fu, H., Zhang, L., Zhang, S. & Zhu, Y. Electron Spin Resonance Spin-Trapping Detection of Radical Intermediates in N-Doped TiO 2 -Assisted Photodegradation of 4-Chlorophenol. *Society* 3061–3065 (2006).

48. Cui, Y., Goldup, S. M. & Dunn, S. Photodegradation of Rhodamine B over Ag modified ferroelectric $BaTiO_3$ under simulated solar light: pathways and mechanism. *RSC Adv.* **5,** 30372–30379 (2015).

49. Chen, Z. *et al.* Accelerating materials development for photoelectrochemical hydrogen production: Standards for methods, definitions, and reporting protocols. *J. Mater. Res.* **25,** 3–16 (2010).

50. Hisatomi, T., Kubota, J. & Domen, K. Recent advances in semiconductors for photocatalytic and photoelectrochemical water splitting. *Chem. Soc. Rev.* **43,** DOI: 10.1039/C3CS60378D (2014).

51. Juan Carlos Colmenares, Y.-J. X. *Heterogeneous Photocatalysis: From Fundamentals to Green Applications*. (Springer, 2015).

52. Fujishima, A., Rao, T. N. & Tryk, D. a. Titanium dioxide photocatalysis. *J. Photochem. Photobiol. C Photochem. Rev.* **1,** 1–21 (2000).

53. Banerjee, A. N. The design, fabrication, and photocatalytic utility of nanostructured semiconductors: focus on TiO2-based nanostructures. *Nanotechnol. Sci. Appl.* **4,** 35–65 (2011).

54. Lee, J.-H., Leu, I.-C., Hsu, M.-C., Chung, Y.-W. & Hon, M.-H. Fabrication of aligned TiO2 one-dimensional nanostructured arrays using a one-step templating solution approach. *J. Phys. Chem. B* **109,** 13056–9 (2005).

55. Bang, J. H. & Kamat, P. V. Solar Cells by Design: Photoelectrochemistry of TiO2 Nanorod Arrays Decorated with CdSe. *Adv. Funct. Mater.* **20,** 1970–1976 (2010).

56. Liu, Z. *et al.* Highly Ordered TiO 2 Nanotube Arrays with Controllable Length for Photoelectrocatalytic Degradation of Phenol. 253–259 (2008).

57. Diebold, U. The Surface Science of Titanium Dioxide. *Appl. Surf. Sci.* **48,** 53–229 (2003).

58. Samsonov, G. V. *The oxide handbook*. (Plenum Press, 1982).

59. Karthick, S. N., Hemalatha, K. V, Raj, C. J., Kim, H. & Yi, M. Processing Research Titanium dioxide paste preparation for dye sensitized solar cell using hydrother- mal technique. **13,** 136–139 (2012).

60. Gupta, S. M. & Tripathi, M. A review of TiO2 nanoparticles. *Chinese Sci. Bull.* **56,** 1639–1657 (2011).

61. Luttrell, T. *et al.* Why is anatase a better photocatalyst than rutile?--Model studies on epitaxial TiO2 films. *Sci. Rep.* **4,** 4043 (2014).

62. Zhang, J., Zhou, P., Liu, J. & Yu, J. New understanding of the difference of photocatalytic activity among anatase, rutile and brookite TiO $_2$. *Phys. Chem. Chem. Phys.* **16,** 20382–20386 (2014).

63. Soundarrajan, P., Sankarasubramanian, K., Raman, S. & K, P. R. Controlled (110) and (101) crystallographic plane growth of single crystalline rutile TiO2 nanorods by facile low cost chemical methods. *CrystEngComm* 8756–8768 (2014). doi:10.1039/C4CE00820K

64. Sajan, C. P., Wageh, S., Al-ghamdi, A. a & Yu, J. TiO 2 nanosheets with exposed { 001 } facets for photocatalytic application. (2015). doi:10.1007/s12274-015-0919-3

65. Dozzi, M. V. & Selli, E. Specific Facets-Dominated Anatase TiO 2 : Fluorine-Mediated Synthesis and Photoactivity. *Catalysts* **3,** 455–485 (2013).

66. Železný, V., Chvostová, D., Pajasová, L., Vrejoiu, I. & Alexe, M. Optical properties of epitaxial BiFeO3 thin films. *Appl. Phys. A* **100,** 1217–1220 (2010).

67. Ihlefeld, J. F. *et al.* Optical band gap of BiFeO[sub 3] grown by molecular-beam epitaxy. *Appl. Phys. Lett.* **92,** 142908 (2008).

68. Kumar, A. *et al.* Linear and nonlinear optical properties of BiFeO[sub 3]. *Appl. Phys. Lett.* **92,** 121915 (2008).

69. Ju, S., Cai, T.-Y. & Guo, G.-Y. Electronic structure, linear, and nonlinear optical responses in magnetoelectric multiferroic material BiFeO(3). *J. Chem. Phys.* **130,** 214708 (2009).

70. Zhao, T. *et al.* Electrical control of antiferromagnetic domains in multiferroic BiFeO3 films at room temperature. *Nat. Mater.* **5,** 823–829 (2006).

71. Wang, H., Zheng, Y., Cai, M., Huang, H. & Chan, H. L. W. First-principles study on the electronic and optical properties of BiFeO 3. *Solid State Commun.* **149,** 641–644 (2009).

72. Higuchi, T., Liu, Y., Yao, P., Glans, P. & Guo, J. Electronic structure of multiferroic BiFeO 3 by resonant soft-X-ray emission spectroscopy. 1–18

73. Neaton, J. B., Ederer, C., Waghmare, U. V., Spaldin, N. a. & Rabe, K. M. First-principles study of spontaneous polarization in multiferroic <math display='inline'> <mrow> <mi mathvariant='normal'>Bi</mi> <mi mathvariant='normal'>Fe</mi> <msub> <mi mathvariant='normal'>O</mi> <mn>3</mn> </msub> </mrow> </math>. *Phys. Rev. B* **71,** 014113 (2005).

74. Clark, S. J. & Robertson, J. Energy levels of oxygen vacancies in BiFeO[sub 3] by

screened exchange. *Appl. Phys. Lett.* **94,** 022902 (2009).

75. Yang, C.-H. *et al.* Electric modulation of conduction in multiferroic Ca-doped BiFeO3 films. *Nat. Mater.* **8,** 485–93 (2009).

76. Paudel, T. R., Jaswal, S. S. & Tsymbal, E. Y. Intrinsic defects in multiferroic BiFeO_{3} and their effect on magnetism. *Phys. Rev. B* **85,** 104409 (2012).

77. Masó, N. & West, A. R. Electrical Properties of Ca-Doped BiFeO 3 Ceramics: From p -Type Semiconduction to Oxide-Ion Conduction. *Chem. Mater.* **24,** 2127–2132 (2012).

78. Mohanty, S. & Choudhary, R. N. P. Dielectric and Electrical Properties of BiFeO3–LiTaO3 Systems. *J. Electron. Mater.* **44,** 2359–2368 (2015).

79. Chen, X. Y. *et al.* Application of weak ferromagnetic BiFeO[sub 3] films as the photoelectrode material under visible-light irradiation. *Appl. Phys. Lett.* **91,** 022114 (2007).

80. Li, S. *et al.* Remarkably enhanced photocatalytic activity of laser ablated Au nanoparticle decorated BiFeO3 nanowires under visible-light. *Chem. Commun.* **49,** 5856 (2013).

81. Zhu, A., Zhao, Q., Li, X. & Shi, Y. BiFeO 3 /TiO 2 Nanotube Arrays Composite Electrode: Construction, Characterization, and Enhanced Photoelectrochemical Properties. (2014).

82. Yang, Y. C. *et al.* Electrospun nanofibers of p-type BiFeO 3 /n-type TiO 2 hetero-junctions with enhanced visible-light photocatalytic activity. *RSC Adv.* **4,** 31941 (2014).

83. Haider, Z. & Kang, Y. S. Facile preparation of hierarchical TiO2 nano structures: Growth mechanism and enhanced photocatalytic H2 production from water splitting using methanol as a sacrificial reagent. *ACS Appl. Mater. Interfaces* **6,** 10342–10352 (2014).

84. Huang, C.-W., Liao, C.-H. & Wu, J. C. S. Photocatalytic Separate Evolution of Hydrogen and Oxygen over Highly Ordered Nanorods and Bulk TiO2Thin Films. *J. Clean Energy Technol.* **1,** 1–5 (2013).

85. Galin, A. & Walendziewski, J. Photocatalytic Water Splitting over Pt-TiO2 in the Presence of Sacrificial Reagents. *Am. Chem. Soc.* **19,** 1143–1147 (2005).

86. Zhang, X., Chen, Y. L., Liu, R.-S. & Tsai, D. P. Plasmonic photocatalysis. *Rep. Prog. Phys.* **76,** 046401 (2013).

87. Hirakawa, T., Kamat, P. V, Uni, V. & Dame, N. Charge Separation and Catalytic Activity of Ag @ TiO 2 Core - Shell Composite Clusters under UV - Irradiation. 3928–3934 (2005).

88. Chandrasekharan, N. & Kamat, P. Improving the Photoelectrochemical Performance of Nanostructured TiO 2 Films by Adsorption of Gold Nanoparticles. *J. Phys. Chem. B* **104,** 10851–10857 (2000).

89. White, C. T. & Mintmire, J. W. Feature article. 7729–7744 (2004). doi:10.1080/14427591.2008.9686601

90. Awazu, K. *et al.* A plasmonic photocatalyst consisting of sliver nanoparticles embedded in titanium dioxide. *J. Am. Chem. Soc.* **130,** 1676–1680 (2008).

91. Di, L. J. *et al.* Enhanced photocatalytic activity of BiFeO3 particles by surface decoration with Ag nanoparticles. *J. Mater. Sci. Mater. Electron.* 2463–2469 (2014). doi:10.1007/s10854-014-1896-0

92. Mohan, S., Subramanian, B. & Sarveswaran, G. A prototypical development of plasmonic multiferroic bismuth ferrite particulate and fiber nanostructures and their

remarkable photocatalytic activity under sunlight. *J. Mater. Chem. C* **2,** 6835 (2014).

93. Papadas, I., Christodoulides, J. a., Kioseoglou, G. & Armatas, G. S. A high surface area ordered mesoporous BiFeO 3 semiconductor with efficient water oxidation activity. *J. Mater. Chem. A* **3,** 1587–1593 (2015).

94. Primo, A., Corma, A. & García, H. Titania supported gold nanoparticles as photocatalyst. *Phys. Chem. Chem. Phys.* **13,** 886–910 (2011).

95. Silva, C. G., Juárez, R., Marino, T., Molinari, R. & García, H. Influence of excitation wavelength (UV or visible light) on the photocatalytic activity of titania containing gold nanoparticles for the generation of hydrogen or oxygen from water. *J. Am. Chem. Soc.* **133,** 595–602 (2011).

96. Kowalska, E., Mahaney, O. O. P., Abe, R. & Ohtani, B. Visible-light-induced photocatalysis through surface plasmon excitation of gold on titania surfaces. *Phys. Chem. Chem. Phys.* **12,** 2344–2355 (2010).

97. Yu, J., Dai, G. & Huang, B. Fabrication and Characterization of Visible-Light-Driven Plasmonic Photocatalyst Ag / AgCl / TiO 2 Nanotube Arrays. *J. Phys. Chem. C* **113,** 16394–16401 (2009).

98. Yu, J., Xiong, J., Cheng, B. & Liu, S. Fabrication and characterization of Ag-TiO2 multiphase nanocomposite thin films with enhanced photocatalytic activity. *Appl. Catal. B Environ.* **60,** 211–221 (2005).

99. Cozzoli, P. D. *et al.* Photocatalytic Synthesis of Silver Nanoparticles Stabilized by TiO 2 Nanorods: A Semiconductor/Metal Nanocomposite in Homogeneous Nonpolar Solution. *J. Am. Chem. Soc.* **126,** 3868–3879 (2004).

100. Anpo, M. The design and development of highly reactive titanium oxide photocatalysts operating under visible light irradiation. *J. Catal.* **216,** 505–516 (2003).

101. Zhai, W., Xue, S., Zhu, A., Luo, Y. & Tian, Y. Plasmon-Driven Selective Oxidation of Aromatic Alcohols to Aldehydes in Water with Recyclable Pt/TiO2 Nanocomposites. *ChemCatChem* **3,** 127–130 (2011).

102. Cheng, X., Liu, H., Chen, Q., Li, J. & Wang, P. Preparation and characterization of palladium nano-crystallite decorated TiO2 nano-tubes photoelectrode and its enhanced photocatalytic efficiency for degradation of diclofenac. *J. Hazard. Mater.* **254-255,** 141–148 (2013).

103. Zhang, Z., Yu, Y. & Wang, P. Hierarchical top-porous/bottom-tubular TiO 2 nanostructures decorated with Pd nanoparticles for efficient photoelectrocatalytic decomposition of synergistic pollutants. *ACS Appl. Mater. Interfaces* **4,** 990–996 (2012).

104. Ye, M., Gong, J., Lai, Y., Lin, C. & Lin, Z. High-efficiency photoelectrocatalytic hydrogen generation enabled by palladium quantum dots-sensitized TiO 2 nanotube arrays. *J. Am. Chem. Soc.* **134,** 15720–15723 (2012).

105. Kowalska, E. *et al.* Hybrid photocatalysts composed of titania modified with plasmonic nanoparticles and ruthenium complexes for decomposition of organic compounds. *Appl. Catal. B Environ.* **178,** 133–143 (2014).

106. Sakthivel, S. *et al.* Enhancement of photocatalytic activity by metal deposition: Characterisation and photonic efficiency of Pt, Au and Pd deposited on TiO 2 catalyst. *Water Res.* **38,** 3001–3008 (2004).

107. Bamwenda, G. R., Tsubota, S., Nakamura, T. & Haruta, M. Photoassisted hydrogen production from a water-ethanol solution: a comparison of activities of Au□TiO2 and Pt□TiO2. *J. Photochem. Photobiol. A Chem.* **89,** 177–189 (1995).

108. Subramanian, V., Wolf, E. & Kamat, P. V. Semiconductor - Metal Composite Nanostructures . To What Extent Do Metal Nanoparticles Improve the Photocatalytic

Activity of TiO 2 Films ? *J. Phys. Chem. B* **105,** 11439–11446 (2001).

109. Kumar, S. G. & Devi, L. G. Review on modified TiO2 photocatalysis under UV/visible light: Selected results and related mechanisms on interfacial charge carrier transfer dynamics. *J. Phys. Chem. A* **115,** 13211–13241 (2011).

110. Bloh, J. Z., Dillert, R. & Bahnemann, D. W. Designing Optimal Metal-Doped Photocatalysts: Correlation between Photocatalytic Activity, Doping Ratio, and Particle Size. *J. Phys. Chem. C* **116,** 25558–25562 (2012).

111. Choi, W., Termin, A. & Hoffmann, M. R. The role of metal ion dopants in quantum-sized TiO\n 2: Correlation between photoreactivity and charge carrier recombination dynamics. *J. Phys. Chem.* **98,** 13669–13679 (1994).

112. Dholam, R., Patel, N., Adami, M. & Miotello, a. Hydrogen production by photocatalytic water-splitting using Cr- or Fe-doped TiO2 composite thin films photocatalyst. *Int. J. Hydrogen Energy* **34,** 5337–5346 (2009).

113. Huang, D. G., Liao, S. J., Liu, J. M., Dang, Z. & Petrik, L. Preparation of visible-light responsive N-F-codoped TiO2 photocatalyst by a sol-gel-solvothermal method. *J. Photochem. Photobiol. A Chem.* **184,** 282–288 (2006).

114. Morikawa, T., Ohwaki, T., Aoki, K., Taga, Y. & Series, N. All use subject to JSTOR Terms and Conditions Visible-Light Photocatalysis Titanium Nitrogen-Doped Oxides. **293,** 269–271 (2013).

115. Umebayashi, T., Yamaki, T., Itoh, H. & Asai, K. Band gap narrowing of titanium dioxide by sulfur doping. *Appl. Phys. Lett.* **81,** 454–456 (2002).

116. Xu, J., Ao, Y., Fu, D. & Yuan, C. Low-temperature preparation of F-doped TiO2 film and its photocatalytic activity under solar light. *Appl. Surf. Sci.* **254,** 3033–3038 (2008).

117. Madhu, C., Bellakki, M. B. & Manivannan, V. Synthesis and characterization of cation-doped BiFeO3 materials for photocatalytic applications. *Indian J. Eng. Mater. Sci.* **17,** 131–139 (2010).

118. Feng, Y. N., Wang, H. C., Shen, Y., Lin, Y. H. & Nan, C. W. Magnetic and photocatalytic behaviors of Ba-doped BiFeO3 nanofibers. *Int. J. Appl. Ceram. Technol.* **11,** 676–680 (2014).

119. Guo, R., Fang, L., Dong, W., Zheng, F. & Shen, M. Enhanced Photocatalytic Activity and Ferromagnetism in Gd Doped BiFeO3 Nanoparticles. *J. Phys. Chem. C* **114,** 21390–21396 (2010).

120. Vinodgopal, K. Enhanced Rates of Photocatalytic Degradation of an Azo Dye Using SnOfiiO2 Coupled Semiconductor Thin Films. **29,** 841–845 (1995).

121. Serpone, N., Maruthamuthu, P., Pichat, P., Pelizzetti, E. & Hidaka, H. Exploiting the interparticle electron transfer process in the photocatalysed oxidation of phenol, 2-chlorophenol and pentachlorophenol: chemical evidence for electron and hole transfer between coupled semiconductors. *J. Photochem. Photobiol. A Chem.* **85,** 247–255 (1995).

122. So, W. W., Kim, K. J. & Moon, S. J. Photo-production of hydrogen over the CdS-TiO2 nano-composite particulate films treated with TiCl4. *Int. J. Hydrogen Energy* **29,** 229–234 (2004).

123. Lee, Y. L., Chi, C. F. & Liau, S. Y. CdS/CdSe Co-Sensitized TiO2 photoelectrode for efficient hydrogen generation in a photoelectrochemical cell. *Chem. Mater.* **22,** 922–927 (2010).

124. Niu, F. *et al.* Facile Synthesis of Highly Efficient *p* - *n* Heterojunction CuO/BiFeO $_3$ Composite Photocatalysts with Enhanced Visible-Light Photocatalytic Activity. *ChemCatChem* n/a–n/a (2015). doi:10.1002/cctc.201500634

125. Luo, J. & Maggard, P. a. Hydrothermal Synthesis and Photocatalytic Activities of SrTiO3-Coated Fe2O3 and BiFeO3. *Adv. Mater.* **18,** 514–517 (2006).

126. Park, H., Park, Y., Kim, W. & Choi, W. Surface modification of TiO2 photocatalyst for environmental applications. *J. Photochem. Photobiol. C Photochem. Rev.* **15,** 1–20 (2013).

127. Abe, R., Shinmei, K., Hara, K. & Ohtani, B. Robust dye-sensitized overall water splitting system with two-step photoexcitation of coumarin dyes and metal oxide semiconductors. *Chem. Commun. (Camb).* 3577–3579 (2009). doi:10.1039/b905935k

128. Kim, W., Tachikawa, T., Majima, T. & Choi, W. Photocatalysis of Dye-Sensitized TiO 2 Nanoparticles with Thin Overcoat of Al 2 O 3 : Enhanced Activity for H 2 Production and Dechlorination of CCl 4. 10603–10609 (2009). doi:10.1021/jp9008114

129. Liu, Y. *et al.* Growth of well-arrayed ZnO nanorods on thinned silica fiber and application for humidity sensing. **20,** 1364–1368 (2012).

130. Greene, L. E. *et al.* Low-Temperature Wafer-Scale Production of ZnO Nanowire Arrays**. 3031–3034 (2003). doi:10.1002/anie.200351461

131. Vayssieres, B. L. Growth of Arrayed Nanorods and Nanowires of ZnO from Aqueous Solutions **. 464–466 (2003).

132. Lee, J.-H., Leu, I.-C., Hsu, M.-C., Chung, Y.-W. & Hon, M.-H. Fabrication of Aligned TiO2 One-Dimensional Nanostructured Arrays Using a One-Step Templating Solution Approach. *J. Phys. Chem. B* **109,** 13057 (2005).

133. Kaya, M., Onganer, Y. & Tabak, A. Preparation and characterization of 'green' hybrid clay-dye nanopigments. *J. Phys. Chem. Solids* **78,** 95–100 (2014).

134. Robinson, J. W. *Atomic Spectroscopy*. (Mercel Dekker, 1996).

135. Kumar, K. V., Porkodi, K. & Selvaganapathi, A. Constrain in solving Langmuir e Hinshelwood kinetic expression for the photocatalytic degradation of Auramine O aqueous solutions by ZnO catalyst. **75,** 246–249 (2007).

136. McCullagh, C., Robertson, P. K. J., Adams, M., Pollard, P. M. & Mohammed, A. Development of a slurry continuous flow reactor for photocatalytic treatment of industrial waste water. *J. Photochem. Photobiol. A Chem.* **211,** 42–46 (2010).

137. Novallc, S. New Reactor Design for Photocatalytic Wastewater Treatment with Ti02 Immobilized on Fused-Silica Glass Fibers: Photomineralization of 4-Chlorophenol. **28,** 670–674 (1994).

138. Yu, H., Lee, S. C., Yu, J. & Ao, C. H. Photocatalytic activity of dispersed TiO2 particles deposited on glass fibers. *J. Mol. Catal. A Chem.* **246,** 206–211 (2006).

139. Guo, W. *et al.* Rectangular bunched rutile TiO2 nanorod arrays grown on carbon fiber for dye-sensitized solar cells. *J. Am. Chem. Soc.* **134,** 4437–41 (2012).

140. Meng, X. *et al.* Growth of hierarchical TiO2 nanostructures on anatase nanofibers and their application in photocatalytic activity. *CrystEngComm* **13,** 3021 (2011).

141. Liu, W., Zhang, L., Cao, L.-X., Su, G. & Wang, Y.-G. Glass fibers templated preparation of TiO2 microtubes assembled from nano/micro hierarchical TiO2 crystals. *J. Alloys Compd.* **509,** 3419–3424 (2011).

142. Lee, J., Leu, I., Hsu, M., Chung, Y. & Hon, M. Fabrication of Aligned TiO 2 One-Dimensional Nanostructured Arrays Using a One-Step Templating Solution Approach. 13056–13059 (2005).

143. Ji, L.-W. *et al.* Effect of seed layer on the growth of well-aligned ZnO nanowires. *J. Phys. Chem. Solids* **70,** 1359–1362 (2009).

144. Wahab, R., Kim, Y.-S., Lee, K. & Shin, H.-S. Fabrication and growth mechanism of hexagonal zinc oxide nanorods via solution process. *J. Mater. Sci.* **45,** 2967–2973 (2010).

145. Polsongkram, D. *et al.* Effect of synthesis conditions on the growth of ZnO nanorods via hydrothermal method. *Phys. B Condens. Matter* **403,** 3713–3717 (2008).

146. Zheng, X. *et al.* Photoelectrocatalytic degradation of rhodamine B on TiO2 photonic crystals. *Phys. Chem. Chem. Phys.* **16,** 15299 (2014).

147. Ng, J., Wang, X. & Sun, D. D. One-pot hydrothermal synthesis of a hierarchical nanofungus-like anatase TiO2 thin film for photocatalytic oxidation of bisphenol A. *Appl. Catal. B Environ.* **110,** 260–272 (2011).

148. Ren, R. *et al.* Controllable Synthesis and Tunable Photocatalytic Properties of Ti3+-doped TiO2. *Sci. Rep.* **5,** 10714 (2015).

149. Mali, S. S. *et al.* Surfactant free most probable TiO2 nanostructures via hydrothermal and its dye sensitized solar cell properties. *Sci. Rep.* **3,** 1–8 (2013).

150. Buranawong, A., Witit-anun, N. & Chaiyakun, S. Total pressure and annealing temperature effects on structure and photo-induce hydrophilicity of reactive DC sputtered TiO \n 2 thin films. *Eng. J.* **16,** 79–89 (2012).

151. Leong, K. H., Chu, H. Y., Ibrahim, S. & Saravanan, P. Palladium nanoparticles anchored to anatase TiO $_2$ for enhanced surface plasmon resonance-stimulated, visible-light-driven photocatalytic activity. *Beilstein J. Nanotechnol.* **6,** 428–437 (2015).

152. Wang, D. *et al.* Enhanced oxygen reduction at Pd catalytic nanoparticles dispersed onto heteropolytungstate-assembled poly(diallyldimethylammonium)-functionalized carbon nanotubes. *Phys. Chem. Chem. Phys.* **13,** 4400–4410 (2011).

153. López-Vinasco, a M. *et al.* Unexpected bond activations promoted by palladium nanoparticles. *Dalton Trans.* **43,** 9038–44 (2014).

154. Wojcieszak, R., Ghazzal, M. N., Gaigneaux, E. M. & Ruiz, P. Low temperature oxidation of methanol to methyl formate over Pd nanoparticles supported on γ-Fe2O3. *Catal. Sci. Technol.* **4,** 738 (2014).

155. Lin, J., Liu, X., Zhu, S., Liu, Y. & Chen, X. Anatase TiO2 nanotube powder film with high crystallinity for enhanced photocatalytic performance. *Nanoscale Res. Lett.* **10,** 110 (2015).

156. Chang, S., Lo, P. & Chang, C. Photocatalytic behavior of TOPO-capped TiO2 nanocrystals for degradation of endocrine disrupting chemicals. *Appl. Catal. B Environ.* **91,** 619–627 (2009).

157. Fu, H., Zhang, L., Zhang, S., Zhu, Y. & Zhao, J. Electron spin resonance spin-trapping detection of radical intermediates in N-doped TiO2-assisted photodegradation of 4-chlorophenol. *J. Phys. Chem. B* **110,** 3061–5 (2006).

158. Lazar, M. a, Varghese, S. & Nair, S. S. Photocatalytic Water Treatment by Titanium Dioxide: Recent Updates. *Catalysts* **2,** 572–601 (2012).

159. Zhang, X., Chen, Y. L., Liu, R.-S. & Tsai, D. P. Plasmonic photocatalysis. *Reports Prog. Phys.* **76,** 046401 (2013).

160. Pelaez, M. & Nolan, N. A Review on the Visible Light Active Titanium Dioxide Photocatalysts for Environmental Applications. **125,** 331–349 (2012).

161. Hashimoto, K., Irie, H. & Fujishima, A. TiO $_2$ Photocatalysis: A Historical Overview and Future Prospects. *Jpn. J. Appl. Phys.* **44,** 8269–8285 (2005).

162. Xu, G. *et al.* Photoelectrochemical performances and potential applications of TiO 2 nanotube arrays modified with Ag and Pt nanoparticles. *Electrochim. Acta* **121,** 194–

202 (2014).

163. Gao, M., Peh, C. K. N., Pan, Y., Xu, Q.-H. & Ho, G. W. Fine structural tuning of whereabout and clustering of metal–metal oxide heterostructure for optimal photocatalytic enhancement and stability. *Nanoscale* **6,** 12655–12664 (2014).

164. Xu, Z. *et al.* Understanding the Enhancement Mechanisms of Surface Plasmon-Mediated Photoelectrochemical Electrodes : A Case Study on Au Nanoparticle Decorated TiO 2 Nanotubes. (2015). doi:10.1002/admi.201500169

165. Al, O. Enhanced photoelectrocatalytic performance of α -Fe 2 O 3 thin films by surface plasmon resonance of Au nanoparticles coupled with surface passivation by atom layer deposition of. *Nanoscale Res. Lett.* 4–11 (2015). doi:10.1186/s11671-015-1077-y

166. Parker, R. a. Static Dielectric Constant of Rutile (TiO$_2$), 1.6-1060$^\\circ$K. *Phys. Rev.* **53,** 1950–1953 (1961).

167. Feng, H. *et al.* A photoelectrochemical immunosensor for tris(2,3-dibromopropyl) isocyanurate detection with a multiple hybrid CdTe/Au-TiO2 nanotube arrays. *Analyst* 5726–5733 (2013). doi:10.1039/c3an00956d

168. Kim, K., Kim, M.-J., Kim, S.-I. & Jang, J.-H. Towards visible light hydrogen generation: quantum dot-sensitization via efficient light harvesting of hybrid-TiO2. *Sci. Rep.* **3,** 3330 (2013).

169. Chiarello, G. L., Aguirre, M. H. & Selli, E. Hydrogen production by photocatalytic steam reforming of methanol on noble metal-modified TiO2. *J. Catal.* **273,** 182–190 (2010).

170. Bahruji, H., Bowker, M., Davies, P. R., Kennedy, J. & Morgan, D. J. The importance of metal reducibility for the photoreforming of methanol on transition metal-TiO2photocatalysts and the use of non-precious metals. *Int. J. Hydrogen Energy* **40,** 1465–1471 (2015).

171. Guo, R., Fang, L., Dong, W., Zheng, F. & Shen, M. Magnetically separable BiFeO3 nanoparticles with a γ-Fe2O3 parasitic phase: controlled fabrication and enhanced visible-light photocatalytic activity. *J. Mater. Chem.* **21,** 18645 (2011).

172. Basu, S. R. *et al.* Photoconductivity in BiFeO3 thin films. *Appl. Phys. Lett.* **92,** 9–11 (2008).

173. Gao, F. *et al.* Preparation and photoabsorption characterization of BiFeO[sub 3] nanowires. *Appl. Phys. Lett.* **89,** 102506 (2006).

174. Joshi, U. a., Jang, J. S., Borse, P. H. & Lee, J. S. Microwave synthesis of single-crystalline perovskite BiFeO[sub 3] nanocubes for photoelectrode and photocatalytic applications. *Appl. Phys. Lett.* **92,** 242106 (2008).

175. Moniz, S. J. a. *et al.* A simple, low-cost CVD route to thin films of BiFeO3 for efficient water photo-oxidation. *J. Mater. Chem. A* **2,** 2922 (2014).

176. Zhang, H. *et al.* Incorporation of Ag nanowires in $CuWO_4$ for improved visible light-induced photoanode performance. *J. Mater. Chem. A* **3,** 9638–9644 (2015).

177. Sung-Suh, H. M., Choi, J. R., Hah, H. J., Koo, S. M. & Bae, Y. C. Comparison of Ag deposition effects on the photocatalytic activity of nanoparticulate TiO2 under visible and UV light irradiation. *J. Photochem. Photobiol. A Chem.* **163,** 37–44 (2004).

178. Edman Jonsson, G., Fredriksson, H., Sellappan, R. & Chakarov, D. Nanostructures for Enhanced Light Absorption in Solar Energy Devices. *Int. J. Photoenergy* **2011,** 1–11 (2011).

179. Lu, J. *et al.* On the room temperature multiferroic BiFeO 3: Magnetic, dielectric and thermal properties. *Eur. Phys. J. B* **75,** 451–460 (2010).

180. Wang, Z. *et al.* Visible-light photocatalytic, solar thermal and photoelectrochemical properties of aluminium-reduced black titania. *Energy Environ. Sci.* **6,** 3007 (2013).

181. Li, C., Hisatomi, T., Watanabe, O. & Nakabayashi, M. Environmental Science Positive onset potential and stability of Cu 2 O-based photocathodes in water splitting by atomic layer deposition of a Ga 2 O 3 buffer layer †. *Energy Environ. Sci.* **8,** 1493–1500 (2015).

182. Tress, W. *et al.* Imbalanced mobilities causing S-shaped IV curves in planar heterojunction organic solar cells. *Appl. Phys. Lett.* **98,** 2011–2013 (2011).

183. Würfel, U., Neher, D., Spies, A. & Albrecht, S. Impact of charge transport on current–voltage characteristics and power-conversion efficiency of organic solar cells. *Nat. Commun.* **6,** 6951 (2015).

184. Ji, W., Yao, K., Lim, Y.-F., Liang, Y. C. & Suwardi, A. Epitaxial ferroelectric BiFeO3 thin films for unassisted photocatalytic water splitting. *Appl. Phys. Lett.* **103,** 062901 (2013).

185. Deng, J., Banerjee, S., Mohapatra, S. K., Smith, Y. R. & Misra, M. Bismuth Iron Oxide Nanoparticles as Photocatalyst for Solar Hydrogen Generation from Water. *J. Fundam. Renew. Energy Appl.* **1,** 1–10 (2011).

186. Values, C. I. Basics of Electrochemical Impedance Spectroscopy Impedance Definition : Concept of Complex Impedance. 1–15 (2015).

187. Kaneko, M., Ueno, H. & Nemoto, J. Thin Film Photoanode in Contact With Redox Electrolyte Solutions. *Beilstein J. Nanotechnol.* **2,** 127–134 (2011).

188. Huang, Q., Kang, F., Liu, H., Li, Q. & Xiao, X. Highly aligned Cu2O/CuO/TiO2 core/shell nanowire arrays as photocathodes for water photoelectrolysis. *J. Mater. Chem. A* **1,** 2418 (2013).

189. Hammond, J. L., Bhalla, N., Rafiee, S. D. & Estrela, P. Localized surface plasmon resonance as a biosensing platform for developing countries. *Biosensors* **4,** 172–88 (2014).

Appendix A – Publications and Presentations

Publications

- **Yilmaz, P;** Lacerda, A. M.; Larrosa, I.; Dunn, S. Development of High Surface Area Titation on Glass Fibre Supports for Photocatalysis. ***Advances in Science and Technology, 2014, 93, 196-202*** **(Conference Proceeding).**

- Zhang, H.; **Yilmaz P.;** Ansari, J. O.; Khan, F. F.; Binions, R.; Krause, S.; Dunn, S. Incorporation of Ag Nanowires in CuWO4 for Improved Visibile Light-Induced Photoanode Performance. ***Journal of Materials Chemistry A, 2015, 3, 9638-9644.***

- **Yilmaz, P;** Yeo, D.; Chang, H.; Loh, L.; Dunn, S. Perovskite $BiFeO_3$ Thin Film Photocathode Performance with Visible Light Activity**,** ***Nanotechnology, 2016, 27, 34, 1-9.***

- **Yilmaz, P;** Lacerda, A. M.; Larrosa, I.; Dunn, S. Photoelectrocatalysis of Rhodamine B and Solar Hydrogen Production by TiO_2 and Pd/TiO_2 Catalyst Systems, ***Electrochimica Acta, Under Review.***

Presentations

- Development of High Surface Area Titation on Glass Fibre Supports for Photocatalysis. ***CIMTEC, 6th Forum on New Materials, June 15-19, 2014. Montecatini Terme, Italy.*** **(Oral Presentation)**

- Ag Modification of $BiFeO_3$ Thin Films Enhanced Photocathode Performance Under Visible Light. ***2015 E-MRS Spring Meeting, May 11-15, 2015. Lille, France.*** **(Poster Presentation)**

- Ag Modification of $BiFeO_3$ Thin Films Enhanced Photocathode Performance Under Visible Light. ***2015 Joint IEEE International Symposium on Applications of Ferroelectric (ISAF), International Symposium on Integrated Functionalities (ISIF), and Piezoresponse Force Microscopy Workshop (PFM) (ISAF-ISIF-PFM 2015), May 24-27, 2015. Singapore.*** **(Oral Presentation).**

- Ag Modification of $BiFeO_3$ Thin Films Enhanced Photocathode Performance Under Visible Light. ***2015 FEMS EUROMAT 2015. European Congress and Exhibition on Advanced Materials and Processes, September 20-24, 2015. Warsaw, Poland.*** **(Oral Presentation).**